

ABSTRACT

Title of dissertation: SPIN-ORBIT-COUPLED
QUANTUM GASES

Juraj Radić, Doctor of Philosophy, 2015

Dissertation directed by: Professor Victor Galitski
Department of Physics

The dissertation explores the effects of synthetic spin-orbit coupling on the behaviour of quantum gases in several different contexts.

We first study realistic methods to create vortices in spin-orbit-coupled (SOC) Bose-Einstein condensates (BEC). We propose two different methods to induce thermodynamically stable static vortex configurations: (1) to rotate both the Raman lasers and the anisotropic trap; and (2) to impose a synthetic Abelian field on top of synthetic spin-orbit interactions. We solve the Gross-Pitaevskii equation for several experimentally relevant regimes and find new interesting effects such as spatial separation of left- and right-moving spin-orbit-coupled condensates, and the appearance of unusual vortex arrangements.

Next we consider cold atoms in an optical lattice with synthetic SOC in the Mott-insulator regime. We calculate the parameters of the corresponding tight-binding model and derive the low-energy spin Hamiltonian which is a combination of Heisenberg model, quantum compass model and Dzyaloshinskii-Moriya interaction. We find that the Hamiltonian supports a rich classical phase diagram with collinear,

spiral and vortex phases.

Next we study the time evolution of the magnetization in a Rashba spin-orbit-coupled Fermi gas, starting from a fully-polarized initial state. We model the dynamics using a Boltzmann equation, which we solve in the Hartree-Fock approximation. The resulting non-linear system of equations gives rise to three distinct dynamical regimes controlled by the ratio of interaction and spin-orbit-coupling strength λ : for small λ , the magnetization decays to zero. For intermediate λ , it displays undamped oscillations about zero and for large λ , a partially magnetized state is dynamically stabilized.

Motivated by an interesting stripe phase which appears in BEC with SOC [Li *et al.*, Phys. Rev. Lett. **108**, 225301 (2011)], we study the finite-temperature phase diagram of a pseudospin-1/2 Bose gas with contact interactions. We show that strong inter-spin interactions can lead to the appearance of magnetically ordered phases at temperatures above the superfluid transition. For the case of inter-spin attraction, we also discuss the possibility of a *bosonic* analogue of the Cooper-paired phase, however this state is not energetically favourable. We extend our calculations to a spin-orbit-coupled Bose gas to investigate the possibility of stripe ordering in the normal phase. However, within our approximations, we do not find an instability towards stripe formation.

Finally, we consider a two-dimensional Bose gas at zero temperature with an underlying quartic single-particle dispersion in one spatial direction. This Hamiltonian can be realized using the NIST scheme of spin-orbit coupling [Y.-J. Lin, K. Jiménez-García, and I. B. Spielman, Nature **471**, 83 (2011)], or using the shaken

lattice scheme of Parker *et al.* [C. V. Parker, L.-C. Ha and C. Chin, Nature Physics **9**, 769 (2013)]. By numerically comparing energies of various trial wave-functions, we show that, at low densities, the ground state is strongly correlated, in contrast to a typical mean-field BEC. The trial wave-function with the lowest energy is of Jastrow-type and it describes a state with finite, but strongly reduced, condensate fraction.

SPIN-ORBIT-COUPLED
QUANTUM GASES

by

Juraj Radić

Dissertation submitted to the Faculty of the Graduate School of the
University of Maryland, College Park in partial fulfillment
of the requirements for the degree of
Doctor of Philosophy
2015

Advisory Committee:

Professor Victor Galitski, Chair/Advisor,

Professor Sankar Das Sarma,

Professor Ian Spielman,

Professor Jay Deep Sau,

Professor Dionisios Margetis (dean's representative)

© Copyright by
Juraj Radić
2015

Acknowledgments

This thesis would not have been possible without people who guided me through my research projects, and people who made my graduate school years enjoyable and worth remembering.

First and foremost, I want to thank my advisor Victor Galitski. He gave me a chance to join his group and to work on very interesting problems, carefully guided me through my research and helped me learn a lot about physics. He was always very understanding and supportive. I am very grateful for this and I will always remember it.

I would like to thank my collaborators, Ian Spielman, Stefan Natu, Andrea Di Ciolo, Tigran Sedrakyan and Kai Sun. Their ideas, guidance and support were essential for the research I am presenting in this thesis. I am also grateful to the Condensed Matter Theory Center, its director Sankar Das Sarma, and the Joint Quantum Institute for providing great environment for doing physics. The people who work here, and frequent seminars and talks were very inspiring and helpful.

I also want to mention my officemates (chronologically): Justin Wilson, Anirban Gangopadhyay, Joe Mitchell, Sergey Pershoguba, Qiuzi Li, Aydin Keser, and Hilary Hurst. I enjoyed our time together and all the conversations and discussions about physics or life in general. I am also grateful to all the other Galitski's group members with whom I spent my time at UMD.

I especially want to thank my roommates and friends from IHoP (the International House of Physicists) for all the years we spent together: Yigit Subasi,

Kanupriya Sinha, Ana Ješovnik, Marko Rajković, Dalia Ornelas, Francisco Salces, Zrinka Gregurić, Dinko Ferenček, Prateek Agrawal, Kevin Schoeffler, Jupiter Bagaipo, Dimitri Trypogeorgos, Wrick Sengupta and others. It was a pleasure living and sharing time with you. It is hard to imagine I could have ever found a better place to live.

Finally, I want to thank my family: my parents, siblings, grandparents, and all the aunts, uncles and cousins, who always supported me in my decisions and endeavors. They have always had a role of a foundation in my life and I could not be more grateful for that.

I would also like to thank the thesis defense committee members for their efforts to carefully read and comment on this thesis.

Table of Contents

List of Tables	vii
List of Figures	viii
List of Abbreviations	xiii
List of Publications	xiv
1 Introduction	1
1.1 Overview of dissertation	2
1.2 Origin of spin-orbit coupling	4
1.3 Synthetic spin-orbit coupling for cold gases	9
1.3.1 Tripod scheme	9
1.3.2 Raman coupling	12
1.3.3 Spin-orbit coupling with Raman lasers	15
1.3.4 Other proposals for creating synthetic SOC	19
2 Vortices in Spin-Orbit-Coupled Bose-Einstein Condensates	21
2.1 Introduction	21
2.2 Rotation in systems with engineered spin-orbit coupling	24
2.2.1 M-scheme	25
2.2.2 Tripod scheme	28
2.2.3 4-level scheme	31
2.3 Creating vortices by rotation	33
2.4 Creating vortices by spatially-dependent detuning	38
2.4.1 The model	38
2.4.2 Qualitative discussion	39
2.4.3 Results	41
2.4.4 Experimental signatures	48
2.5 Conclusion	49
2.6 Other works on vortices in spin-orbit-coupled BECs	50

3	Exotic Quantum Spin Models in Spin-Orbit-Coupled Mott Insulators	60
3.1	Introduction	60
3.2	The model	61
3.3	Low-energy Hamiltonian (spin model)	64
3.4	Classical phase diagram at zero temperature	66
3.5	Experimental realization	69
3.6	Conclusion	72
4	Interaction-Tuned Dynamical Transitions in a Rashba Spin-Orbit Coupled Fermi Gas	73
4.1	Introduction	73
4.2	The model	77
4.3	Results and discussion	79
4.4	Conclusion	85
5	Stoner Ferromagnetism in a Thermal Pseudospin-1/2 Bose Gas	86
5.1	Introduction	86
5.2	The model	89
5.3	Random phase approximation	89
5.4	Hartree-Fock theory	91
5.5	Pairing and collapse for attractive interactions	92
5.6	Magnetism and pairing in 2D	95
5.7	Experimental detection	97
5.8	Stripe order in the presence of SOC?	97
5.9	Conclusion	98
6	Strong Correlation Effects in a Two-Dimensional Bose Gas with Quartic Dispersion	100
6.1	Introduction	100
6.2	The model	102
6.3	Bogoliubov mean-field theory	105
6.4	Wigner crystal state	106
6.5	Strongly-correlated gas in the lower band	107
6.5.1	Non-interacting Fermi gas	107
6.5.2	Spinless system	109
6.5.2.1	“Fermionized” many-body states	109
6.5.2.2	Jastrow Ansatz for a strongly-correlated BEC – the winner	113
6.5.3	Spinful system	115
6.6	Discussion and experimental relevance	117
7	Conclusion	121

A	Rotation of a trap and/or spin-orbit lasers: derivations	124
A.1	M-scheme with rotating trap and spin-orbit lasers	124
A.2	M-scheme with rotating trap	126
A.3	Tripod scheme with rotating trap and spin-orbit lasers	127
B	Finding maximally localized Wannier states	129
C	Derivation of the collisionless Boltzmann equation	132
C.1	Non-interacting part	134
C.2	Interacting part	134
D	RPA susceptibility in the presence of spin-orbit coupling	136
D.1	Non-interacting susceptibility	136
D.2	Interaction susceptibility in RPA	139
E	Strongly correlated bosons with quartic dispersion: various calculations	141
E.1	Box-potential ground state in a system with quartic dispersion	141
E.2	Monte-Carlo calculations	142
E.3	Estimating the interaction energy of a spinless gas at small, but finite densities	144
E.4	Kinetic energy of a many-body wave-function	144
E.5	Estimating spinful state interaction energy	146
	Bibliography	151

List of Tables

6.1	Energy per particle (ϵ) of different states in the low-density limit (n and g are dimensionless density and interaction strength, respectively). Of all the wave-functions (w.f.) we consider, the Jastrow state has the lowest energy. Two wave-functions (absolute value of Fermi-sea w.f. and composite-fermion w.f.) have diverging expectation value of k_x^4 (see text for details).	118
-----	----------------------------------------------------------------------------------------------------------------------------------------------------------------------------------------------------------------------------------------------------------------------------------------------------------------------------------------------------------------------------------------------------------------------	-----

List of Figures

1.1	Physical origin of SOC: electron confined in x - y plane moving in a static electric field \mathbf{E} (a). In electron's frame of reference, Lorentz transformations generate magnetic field which depends linearly on velocity (b). See the text for details.	5
1.2	Tripod scheme: (a) three low-lying internal atomic states are (nearly) resonantly coupled to an excited state using lasers. The scheme produces an effective non-Abelian gauge field for slowly-moving atoms. (b) Laser arrangement for creating SOC.	11
1.3	Raman coupling: two lasers with similar frequencies ($\omega_1 - \omega_2 \approx \varepsilon_2 - \varepsilon_1 \ll \varepsilon_3$) couple low-energy states $ 1\rangle$ and $ 2\rangle$ to the high-energy state $ 3\rangle$. This effectively introduces coupling between $ 1\rangle$ and $ 2\rangle$ as a second-order process.	14
1.4	Generating SOC with Raman lasers: two Raman lasers create spatially varying coupling between $ 1\rangle$ and $ 0\rangle$, and between $ 0\rangle$ and $ -1\rangle$ states. For large quadratic Zeeman shift ($\hbar\omega_q$), state $ 1\rangle$ can be neglected and the remaining two-level system can be described in a pseudospin-1/2 notation.	16
1.5	The energy spectrum of Hamiltonian (1.25). In (a) spectra for different Ω (from $\Omega = 0$ to $\Omega = 6 E_L$) and $\delta = 0$ are shown (spectrum for $\Omega = 0$ is at the top while spectrum for $\Omega = 6 E_L$ is at the bottom). The effect of δ in small Ω regime is shown in (b) ($\Omega = 1 E_L$, $\delta = 0.5 E_L$ (solid blue line), $\delta = 1 E_L$ (dashed red line) and $\delta = 2 E_L$ (dotted black line)). The effect of δ in large Ω regime is shown in (c) ($\Omega = 16 E_L$, $\delta = 0 E_L$ (solid blue line), $\delta = 1 E_L$ (dashed red line) and $\delta = 2 E_L$ (dotted black line)). δ changes position and energy of the minimum.	18

2.1	The density profiles of the rotating spin-orbit-coupled BEC are shown. The first, second and third columns show density of $ \uparrow\rangle$ component ($ \psi_\uparrow ^2$), density of $ \downarrow\rangle$ component ($ \psi_\downarrow ^2$) and the total density ($\rho_T = \psi_\uparrow ^2 + \psi_\downarrow ^2$), respectively. Figure (a) shows results for $\Omega = 0$ which are characterized by density stripes and lines of vortices in both components. The results for $\Omega = 2 E_L$ (b) are qualitatively similar to the $\Omega = 0$ case. Figure (c) shows results for $\Omega = 10 E_L$; a vortex lattice is formed in both components and densities of the two components are almost identical.	37
2.2	The figure shows results for $\Omega = 0$, $\beta = 4 \hbar\omega/a_0$ and $\gamma = 1$. In (a) the total density is shown. The shape of the density is determined by spatially-dependent detuning, which shifts the densities of $ \uparrow\rangle$ and $ \downarrow\rangle$ particles (b). Momentum distribution of $ \uparrow\rangle$ and $ \downarrow\rangle$ components is shown in (c).	51
2.3	The figure shows results for $\Omega = 3 E_L$, $\beta = 8 \hbar\omega/a_0$ and $\gamma = 1$. In (a) the total density is shown. The series of minima at $y = 0$ comes from vortices in $ \uparrow\rangle$ and $ \downarrow\rangle$ wavefunctions (b). Momentum distribution of $ \uparrow\rangle$ and $ \downarrow\rangle$ components is shown in (c).	52
2.4	The figure (a) shows $ \psi_{\uparrow L} ^2$ and $ \psi_{\uparrow R} ^2$ the relative amplitude of which is given by $\int d^2r \psi_{\uparrow L} ^2 = 0.45$ and $\int d^2r \psi_{\uparrow R} ^2 = 0.05$ for the parameters $\Omega = 3 E_L$, $\beta = 8 \hbar\omega/a_0$ and $\gamma = 1$. The superposition of $\psi_{\uparrow L}$ and $\psi_{\uparrow R}$, $\psi_\uparrow = \psi_{\uparrow L} + \psi_{\uparrow R}$, produces vortices in ψ_\uparrow . The density of left- and right-moving particles ($\rho_L = \psi_{\uparrow L} ^2 + \psi_{\downarrow L} ^2$, $\rho_R = \psi_{\uparrow R} ^2 + \psi_{\downarrow R} ^2$) particles is shown in (b).	53
2.5	The figure shows the scalar potential $\Phi(y)$ (a), the effective trapping potential in \hat{y} direction $V_{\text{eff}}(y)$ (b), vector potential $A(y)$ (c) and inverse of the effective mass (d) for $\Omega = 3 E_L$, $\beta = 8 \hbar\omega/a_0$ and $\gamma = 1$. Values corresponding to the left minimum of the spectrum are represented by a solid red line while the values corresponding to the right minimum of the spectrum are represented by a dashed blue line (see the text for details).	54
2.6	The figure shows results for $\Omega = 5 E_L$, $\beta = 12 \hbar\omega/a_0$ and $\gamma = 1$. In (a) the total density is shown. The series of minima at $y = 0$ comes from vortices in $ \uparrow\rangle$ and $ \downarrow\rangle$ wavefunctions (b). Momentum distribution of $ \uparrow\rangle$ and $ \downarrow\rangle$ components is shown in (c).	55
2.7	The figure shows the scalar potential $\Phi(y)$ (a), the effective trapping potential in \hat{y} direction $V_{\text{eff}}(y)$ (b), vector potential $A(y)$ (c) and inverse of the effective mass (d) for $\Omega = 5 E_L$, $\beta = 12 \hbar\omega/a_0$ and $\gamma = 1$	56
2.8	The figure shows results for $\Omega = 10 E_L$, $\beta = 12 \hbar\omega/a_0$ and $\gamma = 1$. In (a) the total density is shown, while (b) and (c) show densities of $ \uparrow\rangle$ and $ \downarrow\rangle$ components. The vortex in the center appears for strong enough effective magnetic field.	57

2.9	The figure shows the effective trapping potential in \hat{y} direction $V_{\text{eff}}(y)$ (a), vector potential $A(y)$ (b), the effective magnetic field B_{eff} (c) and inverse of the effective mass (d) for $\Omega = 10 E_L$, $\beta = 12 \hbar\omega/a_0$ and $\gamma = 1$	58
2.10	The figure shows the total density for $\Omega = 10 E_L$, $\beta = 40 \hbar\omega/a_0$ and $\gamma = 1.85$	58
2.11	Figures show separated left and right phases with vortices in each phase. Trapping frequency is $\omega = 2\pi \times 10$ Hz. Figure (a) shows total density for $\Omega = 4 E_L$, $\beta = 20 \hbar\omega/a_0$ and $\gamma = 1.3$. Figure (b) shows total density for $\Omega = 10 E_L$, $\beta = 150 \hbar\omega/a_0$ and $\gamma = 2.75$	59
3.1	Tunneling amplitudes $T_y^{(1,1)}$ and $T_y^{(1,2)}$ obtained by Peierls substitution (full red and dash-dotted blue line) and localized Wannier states method (full dots and empty circles) for different strengths of Rashba SOC and $V_x = V_y = 10 E_R$	64
3.2	Spin textures: (a) ferromagnet ($\theta_x = \theta_y = 0$); (b) spiral wave ($\theta_x = 0.5$, $\theta_y = 0.2$); (c) vortex phase ($\theta_x = \theta_y = 1$); (d) antivortex phase ($\theta_x = \pi - 1$, $\theta_y = 1$); (e) stripes ($\theta_x = 1.6$, $\theta_y = 0.7$). Phases (a), (b) and (e) are coplanar and shown in a two-dimensional representation.	67
3.3	Classical phase diagram of the Hamiltonian H_B (see text for details): ferromagnet (black corner dots); spiral waves [dark orange (commensurate with four-sites periodicity), light orange (commensurate with three-sites periodicity), red (others)]; stripes (yellow); vortex phase (dark blue) and antivortex phase (light blue). Dashed lines denote the part of the stripe region with continuous ground-state degeneracy and also separate stripe phases of different orientation. Straight black lines separate phases of different orientation inside the spiral region.	70
4.1	Schematic plot showing non-equilibrium steady states of an initially spin-polarized Fermi gas in the presence of SOC. Here $\lambda = gn_0/\alpha p_{\text{th}}$, where gn_0 parametrizes the interactions (Eq. 4.2) and αp_{th} parametrizes the SOC (Eq. 4.3). Different types of steady states are separated by transition points λ_{c1} and λ_{c2} . For small interactions ($\lambda < \lambda_{c1}$), magnetization decays to zero. For $\lambda_{c1} < \lambda < \lambda_{c2}$ magnetization oscillates forever around zero, while for large interactions ($\lambda > \lambda_{c2}$) the system becomes partially polarized.	74

- 4.2 Top-Left: SOC and interactions can be viewed as magnetic fields in the longitudinal (red solid arrow) and transverse direction (blue solid arrow) respectively. The spin precesses around $\mathbf{B}_{\text{eff}} = \mathbf{B}_{\text{SOC}} + \mathbf{B}_{\text{MF}}$. Right Panels: Snapshots of the magnetization for various interaction strengths showing the three different final states: unpolarized, oscillating magnetization and partially polarized state. (Top) Solid red curve is the non-interacting result (see text for analytic formula), and the blue dashed-dotted blue curve has $\lambda = 1.5$. (Center) $\lambda = 2.3$ and the strongly anharmonic curve is $\lambda = 2.977$. (Bottom) $\lambda = 4$. Bottom-Left: The long time-averaged magnetization (dashed blue) and the amplitude of fluctuations about the average $\delta m_z = \sqrt{\langle (m_z - \langle m_z \rangle)^2 \rangle}$ (solid red), for different values of λ . At a first critical value, $\lambda_{c1} = 1.533(3)$, the magnetization develops undamped oscillations about zero, and at a second critical value $\lambda_{c2} = 2.9825(2)$, the net magnetization jumps to a non-zero at long times (vertical blue dotted line). 81
- 4.3 Our spin system as a collection of double wells, corresponding to spin- \uparrow (blue oval, left well) and spin- \downarrow (red oval, right well) at each momentum. The intra-well tunnelling is provided by the spin-orbit magnetic field $B_{\text{SOC}}(\mathbf{p})$ (red arrow), which is momentum dependent, while the different wells are coupled to one another via the interaction term $B_{\text{MF}}(t)$ (blue arrow). Arrow thickness denotes the relative strength of interactions and SOC. (Left): Weak interactions ($B_{\text{MF}} \ll B_{\text{SOC}}$), (Right) Strong interactions ($B_{\text{MF}} \gg B_{\text{SOC}}$). See the text for details. 83
- 5.1 **3D Finite-temperature phase diagram of a pseudospin-1/2 Bose gas**– Intra-species interactions are repulsive ($g_{\uparrow\uparrow} = g_{\downarrow\downarrow} = g = 4\pi\hbar^2 a/m > 0$; we set $an^{1/3} = 0.1$), while the inter-species interaction $g_{\uparrow\downarrow}$ varies. T_c is the ideal gas Bose condensation temperature (only $T > T_c$ is shown), $a_{\uparrow\downarrow}$ is the inter-species scattering length, and n is the total density. For $|g_{\uparrow\downarrow}|$ greater than a critical value, system develops ferromagnetic order in z -direction (ZFM)/ x - y plane (TFM) above the superfluid transition. Collapse occurs for sufficiently large negative $g_{\uparrow\downarrow}$ (see Fig. 5.2). Dashed line shows the transition between the normal unpolarized state (UN) and the paired state. TFM is always favored over pairing in 3D. 87
- 5.2 Thermodynamic instability in $g_{\uparrow\downarrow} < 0$ region in 3D. UN is thermodynamically stable for $g > 0$, while the TFM is stable in the region on the right side of the instability lines: dotted line ($an^{1/3} = 0.4$), dashed line ($an^{1/3} = 0.5$) and dashed-dotted line ($an^{1/3} = 0.6$). . . . 94

5.3	Phase diagram in quasi-2D as a function of temperature and interactions for $\eta = 0.1$. We set $a/a_z = 0.02$ and define $T_0 = \hbar^2 n / 2mk_B$. Blue line shows transition between UN and zFM phase, red line shows transition between UN and TFM phase, dashed-dotted black line corresponds to BKT transition temperature calculated for $a_{\uparrow\downarrow} = 0$. The dashed black line represents the transition between UN and the paired phase.	96
6.1	Schematic picture of the Wigner crystal state. Each particle occupies a different box. There is no overlap between particles and the interaction energy is zero.	108
6.2	We show the correlation function $\rho(\mathbf{r})$ for two different states: (a) composite-fermion state $\psi_{B,cf}^{sq}$ (red dash-dotted line) and (b) Jastrow wave-function ψ_J (black line). Here we set $y = 0$ and concentrate at the dependence on x . $\psi_{B,cf}^{sq}$ wave-function has algebraically decaying correlations, i.e. it has a quasi-long range order, while ψ_J has a true long range order (see text for details).	112

List of Abbreviations

SOC	spin-orbit coupling
BEC	Bose-Einstein condensate
NIST	National Institute of Standards and Technology
1D	one dimension
2D	two dimensions
3D	three dimensions
GP	Gross-Pitaevskii
LWS	localized Wannier states
UP	unpolarized
OM	oscillating magnetization
PP	partially polarized
UN	unpolarized normal phase
zFM	z -direction ferromagnet
TFM	transverse ferromagnet
RPA	Random phase approximation
HF	Hartree-Fock
BCS	Bardeen-Cooper-Schrieffer
WC	Wigner crystal

List of Publications

The dissertation is based on the following papers:

1. J. Radić, T. A. Sedrakyan, I. B. Spielman, and V. Galitski, “Vortices in spin-orbit-coupled Bose-Einstein condensates”, *Phys. Rev. A* **84**, 063604 (2011)
2. J. Radić, A. Di Ciolo, K. Sun, and V. Galitski, “Exotic quantum spin models in spin-orbit-coupled Mott insulators”, *Phys. Rev. Lett.* **109**, 085303 (2012)
3. J. Radić, S. S. Natu, and V. Galitski, “Interaction-tuned dynamical transitions in a Rashba spin-orbit-coupled Fermi gas”, *Phys. Rev. Lett.* **112**, 095302 (2014)
4. J. Radić, S. S. Natu, and V. Galitski, “Stoner ferromagnetism in a thermal pseudospin-1/2 Bose gas”, *Phys. Rev. Lett.* **113**, 185302 (2014)
5. J. Radić, S. S. Natu, and V. Galitski, “Strong correlation effects in a two-dimensional Bose gas with quartic dispersion”, *Phys. Rev. A* **91**, 063634 (2015).

Chapter 1: Introduction

Spin is one of the fundamental degrees of freedom in quantum mechanics. It is often visualized as a spinning top from classical mechanics since it carries non-zero angular momentum. However, spin values are quantized and it does not have a true classical mechanics counterpart. For example, if we measure spin angular momentum of an electron (spin $S = 1/2$) in a certain direction, the measurement can result in only two distinct values: spin up ($S_z = 1/2$) or spin down ($S_z = -1/2$).

In this thesis we are interested in systems where spin and orbital degrees of freedom are coupled. This kind of coupling appears naturally in atomic and solid-state systems: in atomic physics, spin-orbit coupling (SOC) comes in as $H_{\text{soc}} \sim \mathbf{L} \cdot \mathbf{S}$, where \mathbf{L} is orbital angular momentum and \mathbf{S} is the spin angular momentum, and it is responsible for fine-structure splitting in atomic spectra.

In solids, in addition to the ever-present $\mathbf{L} \cdot \mathbf{S}$ term, others forms of SOC appear in systems with broken inversion symmetry. For example, this could be a three-dimensional (3D) system with bulk inversion asymmetry or a two-dimensional (2D) electron gas confined in a quantum well, with an asymmetric confinement potential. SOC has proven to be an essential ingredient for various solid-state systems and applications, like topological insulators [1], spintronics [2], creation of Majorana

fermions in semiconductor nano-wires [3, 4], etc.

In this dissertation we explore effects of spin-orbit coupling in ultracold atom systems. Unlike electrons in solids, cold neutral atoms do not naturally experience SOC and it therefore has to be *engineered*. The experimental efforts to create and study SOC and other synthetic gauge fields, together with theoretical investigations of potentially interesting phenomena have recently been quite intense [5, 6], with topics being studied ranging from Bose-Einstein condensation, vortices, strongly correlated states to the creation of topological bands, topological superfluids and Majorana fermions.

The research presented in this dissertation is a contribution to the subject. It contains studies of the effects of SOC in the context of vortices in BECs, effective spin models in optical lattices, magnetization dynamics in Fermi gases, phase diagram of bosons above the superfluid- T_c , and creating strongly-correlated ground states.

1.1 Overview of dissertation

The dissertation covers several different topics related to the effects of spin-orbit coupling in cold-atom systems. These were subject of my research during graduate school under the supervision of my advisor Victor Galitski. The structure of dissertation is as follows: Chapter 1 discusses the origin of SOC in atomic and solid-state systems, and it presents ways to engineer SOC in cold-atom systems. Chapters 2 through 6 contain results of my research.

Chapter 2 discusses ways to create vortices in spin-orbit-coupled Bose-Einstein

Condensates (SOBEC) and it is based on the work done together with Tigran Sedrakyan, Ian Spielman, and Victor Galitski [Phys. Rev. A **84**, 063604 (2011)]. In this chapter we suggest two different methods to induce thermodynamically stable vortex configurations: (1) to rotate both the Raman lasers and the anisotropic trap; and (2) to impose a synthetic Abelian field on top of synthetic spin-orbit interactions. We study vortex configurations by solving the Gross-Pitaevskii equation for several experimentally relevant regimes.

In chapter 3 we study effective spin model that appears as a low-energy Hamiltonian in the Mott-insulator phase of a gas in a 2D optical lattice with SOC. It is based on the work done together with Andrea di Ciolo, Kai Sun and Victor Galitski [Phys. Rev. Lett. **109**, 085303 (2012)]. We calculate parameters of the tight-binding model and derive the low-energy spin Hamiltonian which is a combination of Heisenberg model, quantum compass model and Dzyaloshinskii-Moriya interaction. The Hamiltonian supports a rich classical phase diagram with collinear, spiral and vortex phases.

Chapter 4 discusses interaction-tuned dynamical transitions in a Rashba spin-orbit-coupled Fermi gas. We study the time evolution of the magnetization of a gas, starting from a fully-polarized initial state. We model the dynamics using a Boltzmann equation, which we solve in the Hartree-Fock approximation. The resulting non-linear system of equations gives rise to three distinct dynamical regimes controlled by the ratio of interaction and spin-orbit-coupling strength. The work was done together with Stefan Natu and Victor Galitski [Phys. Rev. Lett. **112**, 095302 (2014)].

In chapter 5 we investigate the phase diagram of two-component bosons at temperatures above the superfluid transition. We find that strong inter-spin interactions can lead to the appearance of magnetically ordered phases. For the case of inter-spin attraction, we also discuss the possibility of a *bosonic* analogue of the Cooper-paired phase. We extend our calculations to a spin-orbit-coupled Bose gas to investigate the possibility of stripe ordering in the normal phase. The work was done together with Stefan Natu and Victor Galitski [Phys. Rev. Lett. **113**, 185302 (2014)].

Chapter 6 considers a two-dimensional Bose gas at zero temperature with an underlying quartic single-particle dispersion in one spatial direction. This Hamiltonian can be realized using either the NIST scheme of spin-orbit coupling [7] or the shaken lattice scheme of Parker *et al.* [8]. By numerically comparing energies of various trial wave-functions, we show that, at low densities, the ground state is strongly correlated, in contrast to a typical mean-field BEC. The work was done together with Stefan Natu and Victor Galitski [Phys. Rev. A **91**, 063634 (2015)].

1.2 Origin of spin-orbit coupling

Before focusing on the effects of SOC, it is important to understand its physical origin. For the beginning, let us consider an electron constrained in x - y plane, moving in an external electric field. In Fig. 1.1(a) the system is shown in the laboratory frame of reference, however if we transfer to the electron's frame [Fig. 1.1(b)], Lorentz transformations lead to appearance of magnetic field \mathbf{B} which is

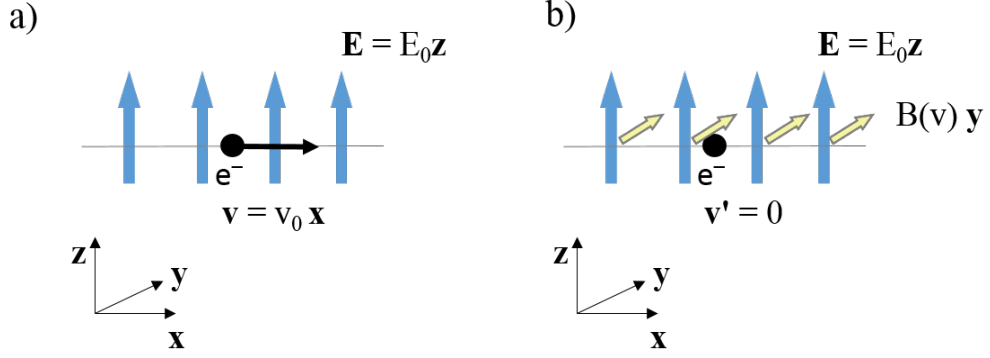


Figure 1.1: Physical origin of SOC: electron confined in x - y plane moving in a static electric field \mathbf{E} (a). In electron's frame of reference, Lorentz transformations generate magnetic field which depends linearly on velocity (b). See the text for details.

perpendicular to electron's momentum and direction of the electric field, and proportional to electron's velocity ($\mathbf{B} \sim p_x \hat{y} - p_y \hat{x}$, where \hat{x} and \hat{y} are unit vectors in x and y direction, respectively). Magnetic field interacts with the electron through the Zeeman term, $H_Z = \boldsymbol{\mu} \cdot \mathbf{B} \sim p_x \sigma_y - p_y \sigma_x$, which is precisely the Rashba SOC. The analysis proves that SOC is a relativistic effect and in what follows we show that it can be derived more rigorously from Dirac equation as a correction to the non-relativistic limit.

The Dirac equation can be written as:

$$i\hbar\partial_t\psi = H\psi, \quad (1.1)$$

$$H = c \boldsymbol{\alpha} \cdot \left(\mathbf{p} - \frac{e}{c} \mathbf{A} \right) + mc^2\beta + eU,$$

where

$$\boldsymbol{\alpha} = \begin{pmatrix} 0 & \boldsymbol{\sigma} \\ \boldsymbol{\sigma} & 0 \end{pmatrix}, \quad \boldsymbol{\beta} = \begin{pmatrix} \mathbb{1}_{2 \times 2} & 0 \\ 0 & -\mathbb{1}_{2 \times 2} \end{pmatrix}, \quad (1.2)$$

(U, \mathbf{A}) is the electromagnetic four-potential, m is the mass of an electron, c is the speed of light in vacuum, e is the charge of an electron, and $\mathbb{1}_{2 \times 2}$ is the 2×2 unit matrix. Since we are interested in the non-relativistic limit, we redefine the zero energy by subtracting mc^2 from the original Hamiltonian:

$$H' = H - mc^2. \quad (1.3)$$

This way a free electron at rest has zero energy. The structure of Dirac equation is such that it is convenient to write the four-component wave-function ψ as

$$\psi = \begin{pmatrix} \phi \\ \chi \end{pmatrix}, \quad (1.4)$$

where ϕ and χ are two-component wave-functions. If we further define $\boldsymbol{\Pi} = \mathbf{p} - e\mathbf{A}/c$, Dirac equation can be written in the form of two coupled equations:

$$i\hbar\partial_t\phi = c (\boldsymbol{\sigma} \cdot \boldsymbol{\Pi}) \chi + eU\phi \quad (1.5)$$

$$i\hbar\partial_t\chi = c (\boldsymbol{\sigma} \cdot \boldsymbol{\Pi}) \phi - (2mc^2 - eU) \chi$$

The fact that we are interested in non-relativistic energies means that $i\hbar\partial_t\chi \sim E \chi \ll mc^2$. Therefore, $i\hbar\partial_t\chi$ term is negligible and $(2mc^2 - eU) \chi \approx c (\boldsymbol{\sigma} \cdot \boldsymbol{\Pi})\phi$.

This allows us to express χ in terms of ϕ :

$$\chi \approx \frac{c (\boldsymbol{\sigma} \cdot \boldsymbol{\Pi})}{2mc^2 - eU} \phi \approx \frac{1}{2mc^2} \left(1 + \frac{eU}{2mc^2} \right) (\boldsymbol{\sigma} \cdot \boldsymbol{\Pi}) \phi, \quad (1.6)$$

and after plugging it into the first equation of (1.5) we arrive at

$$i\hbar\partial_t\phi = \frac{1}{2mc^2} (\boldsymbol{\sigma} \cdot \boldsymbol{\Pi}) \left(1 + \frac{eU}{2mc^2} \right) (\boldsymbol{\sigma} \cdot \boldsymbol{\Pi}) \phi + eU\phi. \quad (1.7)$$

Using the identity $(\boldsymbol{\sigma} \cdot \boldsymbol{\Pi})(\boldsymbol{\sigma} \cdot \boldsymbol{\Pi}) = \Pi^2 + i\boldsymbol{\sigma} \cdot (\boldsymbol{\Pi} \times \boldsymbol{\Pi})$, it is not hard to show that

$$\frac{1}{2m}(\boldsymbol{\sigma} \cdot \boldsymbol{\Pi})(\boldsymbol{\sigma} \cdot \boldsymbol{\Pi}) = \frac{1}{2m} \left(\mathbf{p} - \frac{e\mathbf{A}}{c} \right)^2 - \frac{e}{2m} \boldsymbol{\sigma} \cdot \mathbf{B}. \quad (1.8)$$

What remains is $(e/4m^2)(\boldsymbol{\sigma} \cdot \boldsymbol{\Pi})U(\boldsymbol{\sigma} \cdot \boldsymbol{\Pi})$ operator. The operator contains terms which are second and third order in electromagnetic potentials, however here we are interested only in linear terms and we neglect the rest. Therefore

$$\frac{e}{4m^2}(\boldsymbol{\sigma} \cdot \boldsymbol{\Pi})U(\boldsymbol{\sigma} \cdot \boldsymbol{\Pi}) \approx \frac{e}{4m^2}(\boldsymbol{\sigma} \cdot \mathbf{p})U(\boldsymbol{\sigma} \cdot \mathbf{p}) = \frac{e}{4m^2} (p_k U p_k + i\varepsilon_{klm} \sigma_m p_k U p_l), \quad (1.9)$$

where we used $\sigma_k \sigma_l = \delta_{kl} + i\varepsilon_{klm} \sigma_m$ (ε_{klm} is the third rank antisymmetric tensor). The last term on the right-hand side of (1.9) corresponds to spin-orbit coupling: $i\varepsilon_{klm} \sigma_m p_k U p_l = \boldsymbol{\sigma} \cdot (\nabla U \times \mathbf{p})$. For the moment we neglect the first term on the right-hand side of (1.9) since it is modified when one consistently includes all the corrections up to second order in v^2/c^2 . That leaves us with

$$i\hbar\partial_t\phi = \frac{1}{2m} \left(\mathbf{p} - \frac{e\mathbf{A}}{c} \right)^2 + eU - \frac{e\hbar}{2m} \boldsymbol{\sigma} \cdot \mathbf{B} + \frac{e\hbar}{4m^2 c^2} \boldsymbol{\sigma} \cdot (\nabla\phi \times \mathbf{p}). \quad (1.10)$$

The Dirac equation therefore correctly reproduces both Zeeman term and Pauli spin-orbit coupling. Consistently including all the terms up to second order in v^2/c^2 with the help of Foldy-Wouthuysen transformation [9, 10] results in

$$H = \frac{1}{2m} \left(\mathbf{p} - \frac{e\mathbf{A}}{c} \right)^2 + eU - \frac{p^4}{8m^3 c^2} - \frac{e\hbar}{2m} \boldsymbol{\sigma} \cdot \mathbf{B} - \frac{e\hbar^2}{8m^2 c^2} \nabla \cdot \mathbf{E} + \frac{e\hbar}{4m^2 c^2} \boldsymbol{\sigma} \cdot (\nabla\phi \times \mathbf{p}), \quad (1.11)$$

where, in addition to the terms present in (1.10), there is a correction to kinetic energy (third term), and the Darwin term (fifth term) which leads to a shift in energy of electrons in atomic s orbitals.

The conclusion is that SOC results from a spatially-variable electromagnetic potential U . In the case of a central potential, $U = U(r)$, it reduces to a form familiar from atomic physics:

$$H_{\text{soc}} = \frac{1}{2m^2c^2} \frac{1}{r} \frac{\partial U}{\partial r} \mathbf{L} \cdot \mathbf{S}, \quad (1.12)$$

where $\mathbf{S} = \boldsymbol{\sigma}/2$. The Pauli expression for SOC (Eq. 1.10) makes it clear that the coupling strength is appreciable only for large velocities, strong variation in potential and small mass.

In solids, Pauli expression leads to additional types of SOC when the inversion symmetry is broken. For example, in 3D materials with zinc blende structure (bulk inversion asymmetry) Pauli SOC term leads to the so called cubic Dresselhaus SOC [10, 11], $H = (\hbar/2)\boldsymbol{\sigma} \cdot \boldsymbol{\Omega}_{\text{D3}}(\mathbf{p})$, where

$$\boldsymbol{\Omega}_{\text{D3}}(\mathbf{p}) = \beta (p_x(p_y^2 - p_z^2), p_y(p_z^2 - p_x^2), p_z(p_x^2 - p_y^2)), \quad (1.13)$$

and β is the coupling strength. If we confine electrons to move in a 2D plane, the Dresselhaus SOC reduces to $H = \gamma(p_x\sigma_x - p_y\sigma_y)$, where $\gamma \sim \beta\langle k_z^2 \rangle$ and we assumed confinement in z -direction [10]. Another source of spin-orbit coupling in 2D electron systems is the asymmetry of the confining potential, also known as structural inversion asymmetry. Here it was shown by Rashba that the Pauli term leads to $H = \alpha(p_y\sigma_x - p_x\sigma_y)$, known as Rashba SOC [10, 12]. Materials consisting of elements with large atomic mass typically have stronger SOC, since the potential U , generated by atomic cores, is stronger.

Unfortunately, in cold atom systems SOC is completely negligible: the velocities are extremely small ($v \sim 1$ cm/s), external electric fields are weak, and the mass

of atoms is considerably greater than the electron mass (here we notice that neutral atoms do not satisfy Dirac equation, however we believe that Pauli's expression for SOC can still give an estimate for the strength of the effect). The only way then to have SOC in cold atom systems is to engineer it and this is the topic of the next section.

1.3 Synthetic spin-orbit coupling for cold gases

Cold atoms are very versatile and tunable system which enables us to study various many-body phenomena from solid-state physics in a new and complementary way [13]. For some of those phenomena, like topological insulators and Majorana fermions in semiconductor nano-wires, SOC is an essential ingredient. Unfortunately, SOC does not occur naturally in cold atom systems and the only way around is to find a way to engineer it. This is similar to the Lorentz force, which does not occur naturally for neutral atoms and it has to be created synthetically. Both synthetic SOC and magnetic field have been created experimentally [7, 14–16] and here I explain ways to generate synthetic SOC.

1.3.1 Tripod scheme

In 2005, Ruseckas *et al.* proposed a method of engineering non-Abelian gauge fields for cold atoms [17]. The proposal is based on the so-called tripod scheme where three internal atomic states are coupled to the fourth state using spatially

varying laser fields [Fig. 1.2(a)]. The Hamiltonian of the system is

$$\hat{H} = \frac{\hat{\mathbf{p}}^2}{2m} + V(\mathbf{r}) + \hat{H}_{\text{AL}}(\mathbf{r}), \quad (1.14)$$

$$\hat{H}_{\text{AL}} = \hbar(\Omega_1|0\rangle\langle 1| + \Omega_2|0\rangle\langle 2| + \Omega_3|0\rangle\langle 3|) + \text{H.c.},$$

where \hat{H}_{AL} is the atom-laser interaction Hamiltonian and Ω_j are spatially varying couplings, and $V(\mathbf{r})$ is an external potential. Hamiltonian \hat{H}_{AL} has two degenerate “dark states” with energy $E = 0$: $|\chi_1\rangle = -\Omega_3|1\rangle + \Omega_1|3\rangle$ and $|\chi_2\rangle = -\Omega_2|1\rangle + \Omega_1|2\rangle$ (not orthonormalized). The two other eigenstates ($|\chi_3\rangle$ and $|\chi_4\rangle$) have the energies $E_{3,4} = \pm\sqrt{|\Omega_1|^2 + |\Omega_2|^2 + |\Omega_3|^2}$. The crucial property of dark states is that they do not contain the high-energy $|0\rangle$ state which, at least in principle, means there should be no problems with spontaneous emission. In what follows, the main assumption is that atom-laser coupling is much larger than the kinetic energy of a particle, that is $\Omega_j \gg \langle \hat{\mathbf{p}}^2 \rangle / 2m$. In that case, when we load the atoms into the dark-states subspace, we expect them to stay there as long as their kinetic energy is small (kinetic term couples eigenstates of \hat{H}_{AL}). Since Ω_j are spatially varying, the structure of dark states is spatially dependent and this causes a slowly-moving atom to experience an effective non-Abelian gauge field [17]:

$$\hat{H} = \frac{1}{2m} \left[\hat{\mathbf{p}} - \hat{\mathbf{A}}(\mathbf{r}) \right]^2 + \hat{V}(\mathbf{r}) + \hat{\Phi}(\mathbf{r}), \quad (1.15)$$

where $\hat{\mathbf{A}}$, \hat{V} and $\hat{\Phi}$ are 2×2 matrices:

$$\mathbf{A}_{m,n} = i\hbar \langle \chi_m(\mathbf{r}) | \nabla \chi_n(\mathbf{r}) \rangle,$$

$$V_{m,n} = \langle \chi_m(\mathbf{r}) | V | \chi_n(\mathbf{r}) \rangle,$$

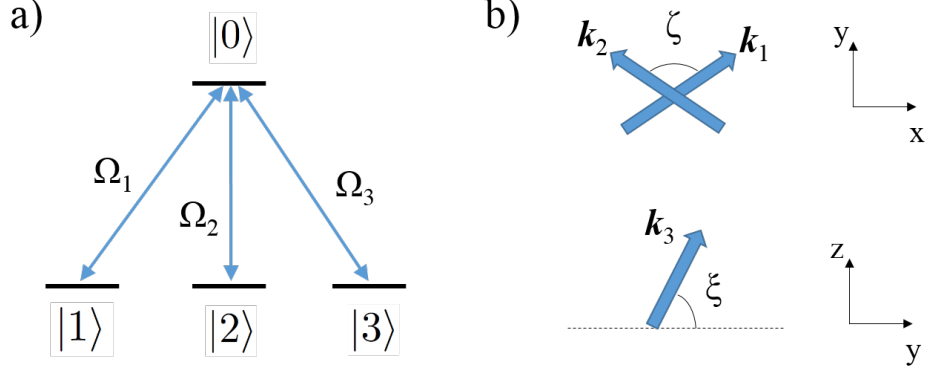


Figure 1.2: Tripod scheme: (a) three low-lying internal atomic states are (nearly) resonantly coupled to an excited state using lasers. The scheme produces an effective non-Abelian gauge field for slowly-moving atoms. (b) Laser arrangement for creating SOC.

$$\Phi_{k,n} = \frac{1}{2m} \sum_{l=3}^4 \mathbf{A}_{k,l} \mathbf{A}_{l,n}.$$

Therefore, by varying laser arrangements and the corresponding $\Omega_j(\mathbf{r})$, it is clearly possible to create different non-Abelian gauge fields [17]. However, it was Stanescu *et al.* who first realized this setup could be used to create effective SOC [18]. To understand this, we notice that SOC can be thought of as a non-Abelian gauge field. That is, a Hamiltonian with a general combination of Rashba and Dresselhaus SOC, $H = \mathbf{p}^2/2m + \alpha(p_y\sigma_x - p_x\sigma_y) + \beta(p_x\sigma_x - p_y\sigma_y)$, can be written in the form of Eq.(1.15), with $\hat{A}_x = -\alpha\sigma_y + \beta\sigma_x$, $\hat{A}_y = \alpha\sigma_x - \beta\sigma_y$. Stanescu *et al.* showed the tripod scheme can produce the following SOC:

$$\hat{H}_{\text{soc}} = -v_0 p_x \sigma_y - v_1 p_y \sigma_z, \quad (1.16)$$

where $v_0 = v_\phi \cos \theta$, $v_1 = v_s \sin^2 \theta / 2$, and $mv_\phi = 2k_1 \sin(\zeta/2)$, $mv_s = k_3 \cos \xi - k_1 \cos(\zeta/2)$. Here \mathbf{k}_1 , \mathbf{k}_2 and \mathbf{k}_3 are the wave-vectors of lasers used in the scheme

[Fig. 1.2(b)], while ζ and ξ describe angles between the lasers.

Unfortunately, in terms of experiments, the tripod scheme is not very promising. The first reason is the fact that degenerate dark states are not the ground state of the atom-laser-interaction Hamiltonian which would cause atoms to gradually escape from the dark-states manifold. The second reason is the (near) resonant coupling to the excited $|0\rangle$ state. While dark states do not contain the excited state, in reality it would be difficult to contain atoms to populate only the dark states and spontaneous emission would be a problem. Therefore, we now concentrate on a scheme for generating SOC that was experimentally realized [7] and which is based on Raman coupling.

1.3.2 Raman coupling

Consider a setup in Fig. 1.3: two lower-energy states are coupled by lasers to a high-energy state. The laser frequencies are such that $\omega_1 - \omega_2 \approx \varepsilon_2 - \varepsilon_1$, $|\omega_1 - \omega_2| \ll \omega_1$, and $\omega_1 \approx \varepsilon_3 - \varepsilon_1$, that is, they are close to resonance. The end result is that although the two lower-energy states are not coupled by lasers directly, they become coupled via second order (two-photon) process.

Lasers couple internal states via dipolar coupling, $H_{\text{dp}} = -\hat{\mathbf{d}} \cdot \mathbf{E}$, where $\hat{\mathbf{d}} = e\hat{\mathbf{r}}$ is the electron dipole operator and \mathbf{E} is the electric field. The Hamiltonian of our

system is then

$$\begin{aligned}
H(t) &= \begin{pmatrix} 0 & 0 & \mathbf{d}_{13} \cdot \mathbf{E}(\mathbf{r}, t) \\ 0 & \varepsilon_2 & \mathbf{d}_{23} \cdot \mathbf{E}(\mathbf{r}, t) \\ c.c. & c.c. & \varepsilon_3 \end{pmatrix} \\
&= \begin{pmatrix} 0 & 0 & \Omega_{11} \cos(\mathbf{k}_1 \cdot \mathbf{r} - \omega_1 t) + \Omega_{12} \cos(\mathbf{k}_2 \cdot \mathbf{r} - \omega_2 t) \\ 0 & \varepsilon_2 & \Omega_{21} \cos(\mathbf{k}_1 \cdot \mathbf{r} - \omega_1 t) + \Omega_{22} \cos(\mathbf{k}_2 \cdot \mathbf{r} - \omega_2 t) \\ c.c. & c.c. & \varepsilon_3 \end{pmatrix}, \tag{1.17}
\end{aligned}$$

where $\mathbf{d}_{ij} = \langle i | \hat{\mathbf{d}} | j \rangle$, $\mathbf{E} = \mathbf{E}_{01} \cos(\mathbf{k}_1 \cdot \mathbf{r} - \omega_1 t) + \mathbf{E}_{02} \cos(\mathbf{k}_2 \cdot \mathbf{r} - \omega_2 t)$ is the electric field created by the lasers, ε_j are energies of the states (we choose $\varepsilon_1 = 0$), and $\Omega_{ij} = \mathbf{d}_{i3} \cdot \mathbf{E}_{0j}$. Next we apply a time-dependent unitary transformation to our system, that is, we transfer to the rotating frame of reference:

$$\psi' = U\psi, \quad H' = UH U^\dagger - iU \partial_t U^\dagger, \tag{1.18}$$

where

$$U = \begin{pmatrix} 1 & 0 & 0 \\ 0 & e^{i(\omega_1 - \omega_2)t} & 0 \\ 0 & 0 & e^{i\omega_1 t} \end{pmatrix}. \tag{1.19}$$

This results in

$$H' = \begin{pmatrix} 0 & 0 & (\Omega_{11}/2)e^{-i\mathbf{k}_1 \cdot \mathbf{r}} + (\Omega_{12}/2)e^{-i\mathbf{k}_1 \cdot \mathbf{r}} e^{-i(\omega_1 - \omega_2)t} \\ 0 & \delta & (\Omega_{21}/2)e^{-i\mathbf{k}_1 \cdot \mathbf{r}} e^{i(\omega_1 - \omega_2)t} + (\Omega_{22}/2)e^{-i\mathbf{k}_2 \cdot \mathbf{r}} \\ c.c. & c.c. & \Delta \end{pmatrix}, \tag{1.20}$$

where $\delta = \varepsilon_2 - (\omega_1 - \omega_2)$ and $\Delta = \varepsilon_3 - \omega_1$. Here we have performed a rotating wave approximation, that is we neglected the fast-oscillating terms like $e^{-2i\omega_1 t}$ since

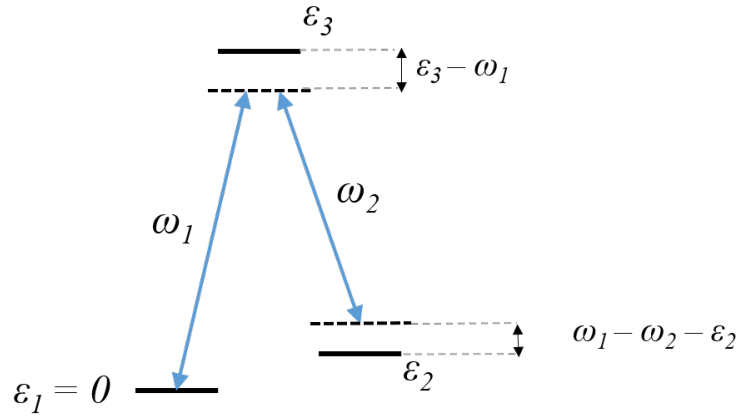


Figure 1.3: Raman coupling: two lasers with similar frequencies ($\omega_1 - \omega_2 \approx \varepsilon_2 - \varepsilon_1 \ll \varepsilon_3$) couple low-energy states $|1\rangle$ and $|2\rangle$ to the high-energy state $|3\rangle$. This effectively introduces coupling between $|1\rangle$ and $|2\rangle$ as a second-order process.

$\omega_1 \approx \omega_2$ frequency is much bigger than any other energy scale in the Hamiltonian.

We notice that Δ is now greater than any other energy/frequency scale in the problem and since we are interested in the “low-energy physics” of the system, we can adiabatically eliminate state $|3\rangle$. If we write the Schrödinger equation of the problem as $i\partial_t \vec{c} = H' \vec{c}$, where $\vec{c} = (c_1, c_2, c_3)$, then $i\partial_t c_3 \ll \Delta c_3$ and $c_3 \approx -(H'_{31} c_1 + H'_{32} c_2)/\Delta$. We then plug in expression for c_3 into equations for $i\partial_t c_1$ and $i\partial_t c_2$ and this produces an effective 2×2 Hamiltonian:

$$H_2 = \begin{pmatrix} -\frac{|H'_{13}|^2}{\Delta} & -\frac{H'_{13}(H'_{23})^*}{\Delta} \\ -\frac{H'_{23}(H'_{13})^*}{\Delta} & -\frac{|H'_{23}|^2}{\Delta} + \delta \end{pmatrix}, \quad (1.21)$$

and after neglecting fast oscillating terms (since $\omega_1 - \omega_2 \gg \delta$), the Hamiltonian becomes

$$H_2 = \begin{pmatrix} -\frac{|\Omega_{11}|^2 + |\Omega_{12}|^2}{4\Delta} & \frac{\Omega_{11}\Omega_{22}^*}{4\Delta} e^{-i(\mathbf{k}_1 - \mathbf{k}_2) \cdot \mathbf{r}} \\ c.c. & \delta - \frac{|\Omega_{22}|^2 + |\Omega_{21}|^2}{4\Delta} \end{pmatrix}. \quad (1.22)$$

Raman lasers therefore introduced coupling between the two low-energy states.

Strength of the coupling is proportional to the intensity of lasers, and inversely proportional to detuning Δ , $\Omega_{11}\Omega_{22}/\Delta \sim \mathbf{E}_0^2/\Delta$. The population of the high-energy state is $|c_3|^2 \sim \Omega/\Delta$. Typically the goal is to make $|c_3|^2$ as small as possible since population in $|3\rangle$ is susceptible to spontaneous emission. This can be achieved with strong lasers: by increasing intensity and detuning Δ while keeping the effective coupling strength $|\Omega|^2/\Delta$ constant, $|c_3|^2$ is reduced.

1.3.3 Spin-orbit coupling with Raman lasers

Synthetic SOC for cold gases was first experimentally achieved by the NIST group in 2011 [7], using a method based on Raman coupling, which I now explain. Let us consider ^{87}Rb atom: the ground state has total spin $F = 1$ and it is therefore three-fold degenerate (the total spin F is the sum of orbital angular momentum l , electron spin $s = 1/2$ and nuclear spin $I = 3/2$; in the ground state of ^{87}Rb $l = 0$). First, a magnetic field is applied to split the ground state degeneracy. The resulting energies are $\varepsilon(m_z = -1) = \hbar\omega_z$, $\varepsilon(m_z = 0) = 0$, and $\varepsilon(m_z = 1) = -\hbar\omega_z - \hbar\omega_q$, where $\hbar\omega_z$ and $\hbar\omega_q$ are the linear and quadratic Zeeman splitting. Next we introduce two Raman lasers with wave-vectors \mathbf{k}_1 and \mathbf{k}_2 (Fig. 1.4). Since the quadratic Zeeman splitting is small ($\omega_q \ll \omega_z$), Raman lasers effectively introduce coupling between $|m_z = -1\rangle$ and $|m_z = 0\rangle$, and $|m_z = 0\rangle$ and $|m_z = 1\rangle$ states. The effective Hamiltonian which results after transforming to the rotating frame of reference, neglecting fast-oscillating terms, and adiabatically eliminating the high-energy state

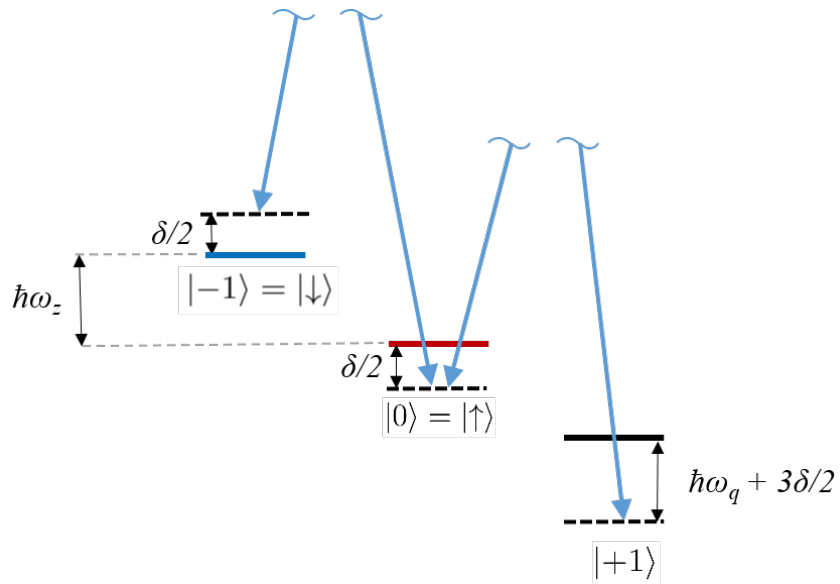


Figure 1.4: Generating SOC with Raman lasers: two Raman lasers create spatially varying coupling between $|1\rangle$ and $|0\rangle$, and between $|0\rangle$ and $| -1\rangle$ states. For large quadratic Zeeman shift ($\hbar\omega_q$), state $|1\rangle$ can be neglected and the remaining two-level system can be described in a pseudospin-1/2 notation.

is [7]:

$$H = \frac{\hbar^2 \hat{\mathbf{k}}^2}{2m} \mathbb{1} + \begin{pmatrix} 3\delta/2 + \hbar\omega_q & 0 & 0 \\ 0 & \delta/2 & 0 \\ 0 & 0 & -\delta/2 \end{pmatrix} + \frac{\Omega}{2} \begin{pmatrix} 0 & e^{-i2k_L x} & 0 \\ e^{i2k_L x} & 0 & e^{-i2k_L x} \\ 0 & e^{i2k_L x} & 0 \end{pmatrix}, \quad (1.23)$$

where Ω is the Raman-coupling strength, $\delta = \hbar(\omega_1 - \omega_2 - \omega_z)$ is detuning from the Raman-resonance, $\hat{\mathbf{k}} = -i\nabla$, and the Hamiltonian is written in the $\{|m_F = 1\rangle, |0\rangle, |-1\rangle\}$ basis. If the quadratic Zeeman splitting, $\hbar\omega_q$, is made large enough ($\hbar\omega_q \gg \Omega, \delta$), $|m_F = 1\rangle$ state is effectively decoupled from the rest of the system and we can then focus on the remaining two states which we label as $|m_F = 0\rangle = |\uparrow\rangle$, $|m_F = -1\rangle = |\downarrow\rangle$, i.e. we use a pseudospin-1/2 notation. The corresponding Hamiltonian is then

$$H = \frac{\hbar^2 \hat{\mathbf{k}}^2}{2m} \mathbb{1} + \frac{\Omega}{2} [\cos(2k_L x) \sigma_x - \sin(2k_L x) \sigma_y] + \frac{\delta}{2} \sigma_z. \quad (1.24)$$

However, the presence of SOC in (1.24) is still not obvious, so we apply a unitary transformation $U = \exp(-ik_L x \sigma_z)$. The transformed Hamiltonian is

$$H = \frac{\hbar^2 \hat{\mathbf{k}}^2}{2m} \mathbb{1} + \frac{\hbar^2 k_L \hat{k}_x}{m} \sigma_z + \frac{\Omega}{2} \sigma_x + \frac{\delta}{2} \sigma_z. \quad (1.25)$$

The presence of SOC is now clear: the Hamiltonian contains a term which couples \hat{k}_x and σ_z , alongside with Zeeman-like terms.

Diagonalization of Hamiltonian (1.25) reveals an interesting spectrum consisting of two bands (Fig. 1.5). For $\delta = 0$ and $\Omega < 4E_L$ ($E_L = \hbar^2 k_L^2 / 2m$), the lower band has two degenerate minima, and these merge to a single minimum for $\Omega \geq 4E_L$. This degeneracy is particularly interesting in the case of low-temperature bosons since it

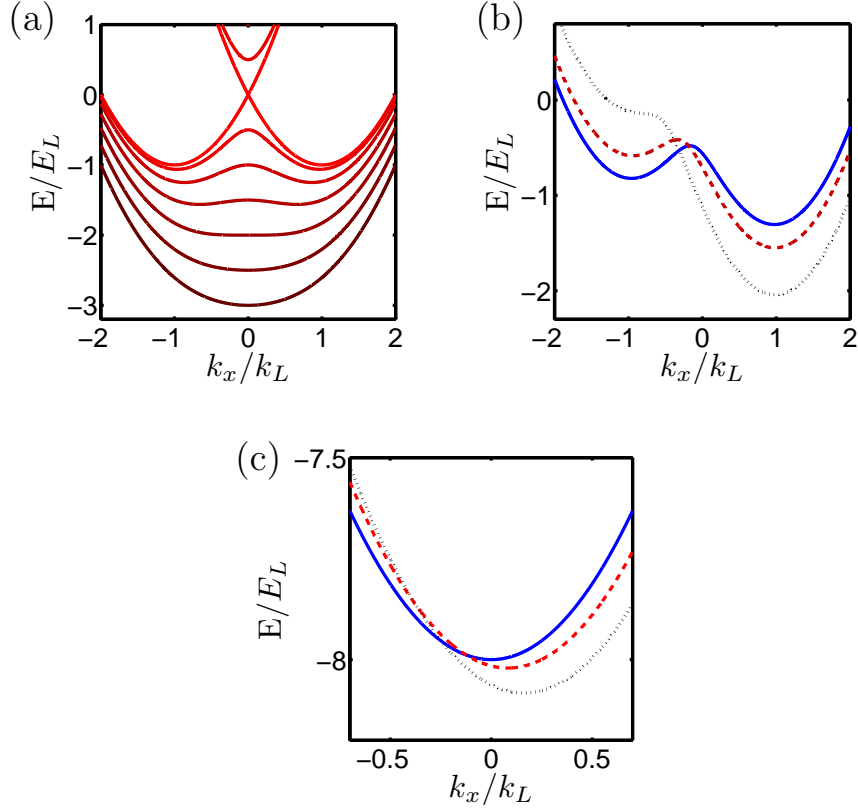


Figure 1.5: The energy spectrum of Hamiltonian (1.25). In (a) spectra for different Ω (from $\Omega = 0$ to $\Omega = 6 E_L$) and $\delta = 0$ are shown (spectrum for $\Omega = 0$ is at the top while spectrum for $\Omega = 6 E_L$ is at the bottom). The effect of δ in small Ω regime is shown in (b) ($\Omega = 1 E_L$, $\delta = 0.5 E_L$ (solid blue line), $\delta = 1 E_L$ (dashed red line) and $\delta = 2 E_L$ (dotted black line)). The effect of δ in large Ω regime is shown in (c) ($\Omega = 16 E_L$, $\delta = 0 E_L$ (solid blue line), $\delta = 1 E_L$ (dashed red line) and $\delta = 2 E_L$ (dotted black line)). δ changes position and energy of the minimum.

is not immediately clear at which minimum particles should condense [19, 20]. At $\Omega = 4 E_L$ the dispersion is quartic in k_x near the minimum. This has interesting consequences which we explore in chapter 6.

Important thing to notice in (1.25) is that the strength of SOC term is independent of the Raman coupling strength Ω . Naively, one could then think that SOC exists even in the absence of Raman coupling. However, this is not true and it can be shown that in the case of $\Omega = 0$ there exists a unitary transformation which con-

nects (1.25) to an ordinary Hamiltonian containing only usual kinetic and Zeeman terms.

1.3.4 Other proposals for creating synthetic SOC

The NIST type of SOC that we have just covered is quite simple to realize experimentally and there are several groups which have been doing experiments using the method [21–23]. However, this kind of SOC is very specific: it is one-dimensional and unadjustable, and we would like to be able to generate more general types of SOC (for example, realizing Rashba SOC would enable experimental studies of various interesting phenomena [24–26]). Another issue is that Raman coupling suffers from spontaneous emission, because even though the occupation of the high-energy state is very small, it is still finite. Possible resolution of this problem would be to construct an atom-chip where SOC would be generated by direct coupling of states in the $F = 1$ ground-state manifold using radio-frequency electro-magnetic fields [27]. This way the high-energy state and the associated spontaneous emission would be avoided.

There have been several proposals for realizing more general types of SOC and here I list some of them. (a) tripod scheme [18], which we have already discussed, (b) cyclically-coupled-states method [28]: it produces Rashba SOC with a controllable Dresselhaus contribution. The method is based on Raman coupling, however instead of having two Raman lasers which couple two internal states, here there are five Raman lasers which couple four internal states. Higher number of lasers

and internal states makes it more difficult to realize experimentally and it leads to higher heating and losses relative to the original NIST scheme. (c) pulsed magnetic fields method [29,30]: here SOC is generated by a sequence of pulsed inhomogeneous magnetic fields which imprint suitable phase gradients on the atoms. The resulting “time-averaged” Hamiltonian approximates Rashba SOC (both 2D and 3D SOC can be generated). This proposal does not suffer from spontaneous emission, however it relies on time-dependent driving which often leads to heating.

Chapter 2: Vortices in Spin-Orbit-Coupled Bose-Einstein Condensates

2.1 Introduction

The concept of spin-orbit-coupled BEC was first proposed by Stanescu *et al.* [19] as a state of pseudospin-1/2 (two-component) bosons under the influence of synthetic SOC. There and in subsequent publications [20, 31–34] it was shown that the corresponding free-particle energy spectrum with double-minima at finite momenta leads to different types of ground states depending on interparticle interactions. For example, if particles condense only in one of the two minima, the state is called a plane-wave BEC and it has spatially-uniform density. However, if bosons condense in both minima (or a superposition of the minima), the resulting state is called a stripe BEC since it has areas with higher and lower density, resembling stripes [20,31]. The first spin-orbit-coupled BEC was experimentally realized by Lin *et al.* [7] in 2011, and transitions between plane-wave and stripe BEC phases were observed more recently in Ref. [23].

It is even more interesting to consider the case of Rashba SOC where the minimum of the energy spectrum has a ring degeneracy. There the ground state of

bosons is generally still described by either a plane-wave or stripe BEC [24, 25, 31]. However, this changes significantly in the case of 2D bosons at low densities [26] and it will be discussed later in chapter 6.

Among the obvious questions about the spin-orbit BECs is the physics of topological excitations - vortices - that play a central role in the physics of conventional BECs. This is the subject of this chapter, where we focus primarily on exploring experimentally-relevant methods that can be used to nucleate static vortex structures in spin-orbit BECs. In contrast to the conventional condensates, the situation here is shown to be significantly more complicated as the vortex physics is obscured by the interplay of external perturbations intended to create them and the hyperfine structure underlying the synthetic spin-orbit-coupling setup.

It is widely known and often taken for granted that rotating a Bose-Einstein condensate gives rise to the formation of vortices that arrange themselves into static vortex lattice structures. However, this picture is not in fact an obvious outcome of rotation, which represents a *time-dependent perturbation* due to a rotating anisotropic trap potential. The many subtleties involved in understanding the fundamentals of the related phenomena are discussed in detail in the reviews by Leggett [35, 36], but the main conclusion is indeed that the physics of a one-component BEC confined to a spinning anisotropic trap can be mapped onto a statistical-mechanical problem of the BEC with an effective *time-independent* Hamiltonian, $H_{\text{eff}} = H - \boldsymbol{\omega}_r \cdot \mathbf{L}$, which describes the system in a rotating frame of reference (here, \mathbf{L} is the orbital angular momentum operator and $\boldsymbol{\omega}_r$ is the frequency of rotation).

A naive expectation therefore is that to rotate an anisotropic trap would be a straightforward means to create vortex structures in spin-orbit-coupled BECs as well. However, here we show that this is *not so* and other, more sophisticated methods have to be involved in order to create static vortex structures. We show that the problem with rotation arises here because atoms are not influenced by the trapping potential only, but also by the lasers which create spin-orbit coupling in the first place. Therefore, if only the anisotropic potential rotates, it is in general impossible to choose a frame of reference where the Hamiltonian is time-independent, because the “spin-orbit-coupling lasers”, stationary in the lab frame, are rotating in the rotating frame, generally resulting in non-trivial dynamics in any rotating frame. While there do exist rare degenerate cases, where a unitary transformation can be found that eliminates time-dependence from the non-interacting Hamiltonian, the interaction terms generally become time-dependent under the unitary transformation, resulting again in a non-equilibrium problem. Hence, we argue that the residual time-dependence appears to be an essential and unwelcome property of a spin-orbit-coupled BEC with rotating anisotropic potential (at least for the realistic laser schemes currently known to us). We believe that while the specifics of time-evolution of spin-orbit-coupled BECs with rotating trap are sensitive to details of both the laser setup used and interactions, the typical scenario will involve non-universal dynamics that would inevitably lead to heating and destruction of the coherent state in contrast to the conventional BECs.

It is therefore desirable to develop other experimentally-relevant methods to create vortices, like rotation or a magnetic field, for spin-orbit-coupled BECs. Two

other ways suggested here and examined in detail are as follows: (i) to rotate both the lasers creating spin-orbit coupling and the trap, if the latter is anisotropic, or just the lasers for an isotropic trap (note that to rotate an isotropic trap has no meaning); (ii) To combine synthetic spin-orbit-couplings with a synthetic Abelian magnetic field. Theoretically, both methods are shown to give rise to interesting phenomena, including the appearance of sought-after static vortices and vortex lattices, parity effects in vortex nucleation, and real-space splitting of the spin-orbit BEC where the left- and right-moving parts are physically separated (an effect which bears some similarity to the spin-Hall effect known in condensed matter spintronics).

The chapter is structured as follows: Sec. 2.2 derives effective Hamiltonians corresponding to a rotating trapping potential and/or rotating “spin-orbit lasers” for various spin-orbit-coupled laser schemes. In Sec. 2.3, we solve the Gross-Pitaevskii equation to describe individual vortices and collective vortex structures for the laser scheme described in Ref. [7] with a rotating trap and Raman lasers. In Sec. 2.4, we investigate vortex nucleation and other effects associated with a synthetic magnetic field that can be imposed on top of the spin-orbit coupled system used in [7] by applying a spatially dependent Zeeman field.

2.2 Rotation in systems with engineered spin-orbit coupling

In this section, we investigate the effect of rotation of an anisotropic trapping potential and/or spin-orbit lasers in three different laser schemes that have been proposed to create effective spin-orbit couplings. To distinguish between the

different schemes, we will refer to the setup used in Ref. [7] as “M-scheme,” the proposal described in Refs. [17,18] as “tripod-scheme,” and the proposal of Ref. [28] as “4-level-scheme.”

2.2.1 M-scheme

We first focus on the scheme that was experimentally realized [7] and investigate the Hamiltonian for the case in which both trap and spin-orbit-coupling lasers are rotating about the z -axis. The atoms in [7] are under the influence of three external sources: trapping potential, Raman lasers which create spin-orbit coupling and magnetic field which creates Zeeman splitting (aligned along \hat{y} direction). If we wanted to get a time-independent Hamiltonian in the rotating frame we would have to rotate trapping potential, Raman lasers and magnetic field. To make things easier it is possible to change direction of the magnetic field to be along z -axis, which makes rotation of magnetic field about the z -axis unnecessary. If the change of the direction of magnetic field is accompanied by change in polarization of Raman lasers (the direction of lasers stays the same) the system is described by the same effective equations as in [7]. It is also important to note that, in the case of an isotropic trap, rotation of the trap does not have any effect and in that case rotating only the Raman lasers suffices. The stationary system is described by the following

Hamiltonian (see methods in [7]):

$$\hat{H}_0 = \left[\frac{\hbar^2 \hat{\mathbf{k}}^2}{2m} + V(\mathbf{r}) \right] \check{1} + \begin{pmatrix} \hbar(-\omega_z + \omega_q) & 0 & 0 \\ 0 & 0 & 0 \\ 0 & 0 & \hbar\omega_z \end{pmatrix} \quad (2.1)$$

$$+ \sqrt{2}\Omega \check{\sigma}_{3,x} \cos(2k_L x + \Delta\omega_L t),$$

where $\hat{\mathbf{k}} = -i\nabla$, $V(\mathbf{r})$ is the trapping potential, $\check{1}$ is the 3×3 identity matrix, $\check{\sigma}_{3,x,y,z}$ are the 3×3 spin matrices, $k_L = \sqrt{2}\pi/\lambda$, Ω is the Raman coupling strength, ω_z and ω_q are the linear and quadratic Zeeman shifts, respectively. Here λ is the wavelength and $\Delta\omega_L$ is the frequency difference of the two Raman beams used in the M-scheme. The Hamiltonian is written in the basis of hyperfine states $\{|m_F = +1\rangle, |m_F = 0\rangle, |m_F = -1\rangle\}$ which are quantized in \hat{z} direction (direction of the external magnetic field).

When the trap and Raman lasers rotate with a constant frequency ω_r about the z -axis, the Hamiltonian \hat{H}_{rot} in the laboratory frame can be obtained from Eq. (2.1) using the following substitutions:

$$V(x, y, z) \rightarrow V(x(t), y(t), z)$$

$$\check{\sigma}_{3,x} \cos(2k_L x + \Delta\omega_L t) \rightarrow \check{\sigma}_{3,x}(t) \cos(2k_L x(t) + \Delta\omega_L t), \quad (2.2)$$

where

$$x(t) = x \cos(\omega_r t) + y \sin(\omega_r t)$$

$$y(t) = y \cos(\omega_r t) - x \sin(\omega_r t) \quad (2.3)$$

$$\check{\sigma}_{3,x}(t) = \check{\sigma}_{3,x} \cos(\omega_r t) + \check{\sigma}_{3,y} \sin(\omega_r t).$$

The Hamiltonian \hat{H}_{rot} can be also written in a more compact form:

$$\hat{H}_{\text{rot}} = e^{-i\omega_r t(\hat{L}_z + \hat{S}_z)/\hbar} \hat{H}_0 e^{i\omega_r t(\hat{L}_z + \hat{S}_z)/\hbar}, \quad (2.4)$$

where $\hat{\mathbf{L}}$ is the orbital angular momentum operator and $\hat{\mathbf{S}}$ is the spin operator, and \hat{L}_z and \hat{S}_z are their z -components: $\hat{L}_z = \hbar(x\hat{k}_y - y\hat{k}_x)\check{1}$, $\hat{S}_z = \hbar\check{\sigma}_{3,z}$.

The Hamiltonian (2.4) is time-dependent in the laboratory frame, but we show below that this time-dependence can be eliminated by a unitary transform. Recall that an arbitrary unitary transform, $\hat{U}(t)$, of the Hamiltonian \hat{H} produces a new Hamiltonian, \hat{H}' , as follows

$$\hat{H}' = \hat{U}\hat{H}\hat{U}^\dagger - i\hbar\hat{U}\frac{\partial\hat{U}^\dagger}{\partial t}. \quad (2.5)$$

We first go to the rotating frame of reference (rotating together with both the trap and the lasers) [37]: $|\psi_{RF}\rangle = \hat{U}(t)|\psi\rangle$, where $\hat{U}(t) = \exp[i\omega_r t(\hat{L}_z + \hat{S}_z)/\hbar]$. Eq. (2.5) yields

$$\hat{H}_{RF} = \hat{H}_0 - \omega_r(\hat{L}_z + \hat{S}_z), \quad (2.6)$$

where \hat{H}_{RF} denotes the Hamiltonian in the rotating frame. The remaining time-dependence, arising from the oscillating Raman laser fields in \hat{H}_0 , can be removed in the framework of the rotating wave approximation. To obtain an effective description of the system in terms of two internal pseudo-spin states, we follow [7] and choose the quadratic Zeeman shift $\hbar\omega_q$ to be large enough, so that the state $|m_z = 1\rangle$ can be neglected. Using the pseudo-spin-1/2 labels for internal states, we get, $|\uparrow\rangle \equiv |m_z = 0\rangle$, $|\downarrow\rangle \equiv |m_z = -1\rangle$. The final Hamiltonian can be expressed in the form used in Ref. [7] (a detailed derivation is much analogous to Ref. [7] and is

presented in appendix A.1) as follows,

$$\hat{H}_{RF,2} = \left[\frac{\hbar^2 \hat{\mathbf{k}}^2}{2m} + V(\mathbf{r}) - \omega_r \hat{L}_z \right] \check{\mathbb{1}} + \frac{\hbar^2 k_L}{m} \hat{k}_x \check{\sigma}_z + \frac{\Omega}{2} \check{\sigma}_x + \hbar \omega_r k_L y \check{\sigma}_z + \begin{pmatrix} 0 & 0 \\ 0 & \hbar \omega_r - \delta \end{pmatrix}, \quad (2.7)$$

where $\check{\mathbb{1}}$ is 2×2 unit matrix, $\check{\sigma}_{x,y,z}$ are 2×2 Pauli matrices and $\delta = \hbar(\Delta\omega_L - \omega_z)$ is a detuning from the Raman resonance. Since the resulting Hamiltonian is time-independent in the rotating frame, it leads to the appearance of stationary vortex structures studied below in Sec. 2.3.

In the case where *only* the anisotropic trap is rotating, the Hamiltonian in the laboratory frame is given by (2.1), with $V(x, y, z) \rightarrow V(x(t), y(t), z)$. Importantly, if we go to the rotating frame and make the rotating wave approximation (exactly as in the above), we are still left with a time-dependence (for details see appendix A.2):

$$\hat{H}'_{RF,2} = \left[\frac{\hbar^2 \hat{\mathbf{k}}^2}{2m} + V(\mathbf{r}) - \omega_r \hat{L}_z \right] \check{\mathbb{1}} + \frac{\hbar^2 k_L}{m} \hat{k}_x(t) \check{\sigma}_z + \frac{\Omega}{2} \check{\sigma}_x + \frac{\delta}{2} \check{\sigma}_z, \quad (2.8)$$

where $\hat{k}_x(t) = \hat{k}_x \cos(\omega_r t) - \hat{k}_y \sin(\omega_r t)$.

2.2.2 Tripod scheme

We now concentrate on the proposal described in Refs. [17, 18], which uses a so-called “tripod scheme,” that consists of three degenerate ground states of an atom coupled to an excited state. The resulting energy spectrum includes two degenerate “dark” states and two “bright” states (one of the bright states is higher and the other is lower in energy with respect to degenerate dark states). In the strong coupling

regime and within the adiabatic approximation, the energy difference between the dark and bright states is very large compared to other characteristic energies of the system. In this case, a coupling between the dark and bright states is negligible, and consequently if the atoms are initially within the dark states subspace, they are expected to stay there for a long time. From now on, we use pseudospin-1/2 notation for the two degenerate dark states.

The effective stationary Hamiltonian (projected onto the dark-state subspace) reads:

$$\hat{H} = \left[\frac{\hat{\mathbf{p}}^2}{2m} + w(\mathbf{r}) \right] \check{1} - v_0 \hat{p}_x \check{\sigma}_y - v_1 \hat{p}_y \check{\sigma}_z + \delta_0 \check{\sigma}_z, \quad (2.9)$$

where $\mathbf{p} = -i\hbar\nabla$, $w(\mathbf{r})$ is a spin-independent part of the trapping potential, v_0 and v_1 characterize the strength and type of spin-orbit coupling, and δ_0 is the effective Zeeman splitting (see section 1.3.1 for details). $\check{1}$ is a 2×2 unit matrix, $\check{\sigma}_{x,y,z}$ are 2×2 Pauli matrices.

We first investigate the case with both the trap and the spin-orbit lasers rotating. The derivation, presented in appendix A.3, leads to the following Hamiltonian in the rotating frame

$$\begin{aligned} \hat{H}_{RF,2} = & \left[\frac{\hat{\mathbf{p}}^2}{2m} + w(\mathbf{r}) - \omega_r \hat{L}_z \right] \check{1} - v_0 \hat{p}_x \check{\sigma}_y - v_1 \hat{p}_y \check{\sigma}_z + \delta_0 \check{\sigma}_z + m\hbar\omega_r (v_1 x \check{\sigma}_z - v_0 y \check{\sigma}_y) \\ & - \hbar\omega_r \begin{pmatrix} \sin^2 \phi & \sin \phi \cos \phi \cos \theta \\ \sin \phi \cos \phi \cos \theta & \cos^2 \theta \cos^2 \phi - \sin^2 \theta \end{pmatrix}, \end{aligned} \quad (2.10)$$

where $\phi = mv_0 x / \cos \theta$, $\delta_0 = \sin^2 \theta \{ \delta - [(\frac{v_0}{\cos \theta})^2 + (\frac{v_1}{\sin^2(\theta/2)})^2] / 2 \} / 2$, and θ is a constant. Let us note here that in Ref. [38] the tripod scheme under rotation has

already been considered, however with slightly different results (the spin angular momentum part $(-\omega_r \hat{S}_z)$ was ignored in Ref. [38]).

Our result (2.10), together with Eq. (2.7) for the M-scheme, clearly shows that the effect of rotation in systems with synthetic spin-orbit interaction does not reduce to just adding the $-\omega_r L_z$ term for the Hamiltonian in the rotating frame, but also produces other position-dependent terms, which depend on a particular scheme.

We now consider the tripod scheme with only the trap rotating. We first address the following question: if the trapping potential is time-dependent, can we get the effective pseudo-spin Hamiltonian in the laboratory frame just by changing $V \rightarrow V(t)$ in (2.9); or in other words, are we still allowed to restrict to the dark-state subspace if the external potential is time dependent? The answer is certainly “yes,” if the trapping potential is the same for all three degenerate ground states (which is most often the case for optical trapping), because this kind of time-dependent potential does not couple the dark and bright states.

In a general tripod scheme however, the trapping potential is not spin independent ($\hat{V}(\mathbf{r}) = \sum_j V_j(\mathbf{r})|j\rangle\langle j|$, $V_1 = V_2 = w(\mathbf{r})$ and $V_3 = w(\mathbf{r}) + \delta$). To better understand this, let us choose states $\{|1\rangle, |2\rangle, |3\rangle\}$ to be eigenstates of \hat{S}_z (z-component of the total spin operator). Then, the rotation of the trapping potential about the z-axis is described by: $V_1 = V_2 = w'(\mathbf{r}, t)$ and $V_3 = w'(\mathbf{r}, t) + \delta$, where $w'(\mathbf{r}, t) = e^{-i\omega_r t \hat{L}_z / \hbar} w(\mathbf{r}) e^{i\omega_r t \hat{L}_z / \hbar}$. We can therefore separate $\hat{V}(\mathbf{r})$ into a stationary spin-dependent term and a time-dependent but spin-independent term: $\hat{V}(\mathbf{r}, t) = \delta|3\rangle\langle 3| + w'(\mathbf{r}, t)(|1\rangle\langle 1| + |2\rangle\langle 2| + |3\rangle\langle 3|)$. Therefore the time-dependent part of trapping potential is spin independent and it will not couple dark and bright

states. With this, the tripod system with a trap rotating about the z-axis is described by

$$\hat{H} = \left[\frac{\hat{\mathbf{P}}^2}{2m} + w'(\mathbf{r}, t) \right] \check{1} - v_0 \hat{p}_x \check{\sigma}_y - v_1 \hat{p}_y \check{\sigma}_z + \delta_0 \check{\sigma}_z. \quad (2.11)$$

We now make the following transformation: $\hat{U}(t) = \exp[i\omega_r t(\hat{L}_z/\hbar + \check{\sigma}_x/2)]$, which gives:

$$\begin{aligned} \hat{H}' = & \left[\frac{\hat{\mathbf{P}}^2}{2m} + w(\mathbf{r}) - \omega_r \hat{L}_z \right] \check{1} - v_0 \hat{p}_x(t) \check{\sigma}_y(t) \\ & - v_1 \hat{p}_y(t) \check{\sigma}_z(t) + \delta_0 \check{\sigma}_z(t) - \frac{\hbar\omega_r}{2} \check{\sigma}_x, \end{aligned} \quad (2.12)$$

where

$$\begin{aligned} \hat{p}_x(t) &= \hat{p}_x \cos(\omega_r t) - \hat{p}_y \sin(\omega_r t), \\ \hat{p}_y(t) &= \hat{p}_y \cos(\omega_r t) + \hat{p}_x \sin(\omega_r t), \\ \check{\sigma}_y(t) &= \check{\sigma}_y \cos(\omega_r t) - \check{\sigma}_z \sin(\omega_r t), \\ \check{\sigma}_z(t) &= \check{\sigma}_z \cos(\omega_r t) + \check{\sigma}_y \sin(\omega_r t). \end{aligned} \quad (2.13)$$

The Hamiltonian (2.12) is generally time-dependent. However in the case of Rashba coupling ($v_0 = v_1 = v$) and $\delta_0 = 0$, this *non-interacting part* of the Hamiltonian becomes static and reads,

$$\hat{H}' = \left[\frac{\hat{\mathbf{P}}^2}{2m} + w(\mathbf{r}) - \omega_r \hat{L}_z \right] \check{1} - v(\hat{p}_x \check{\sigma}_y + \hat{p}_y \check{\sigma}_z) - \frac{\hbar\omega_r}{2} \check{\sigma}_x. \quad (2.14)$$

2.2.3 4-level scheme

Here we study the 4-level-scheme [28] for the case where only the trap is rotating. The stationary effective Hamiltonian (projected to the lowest energy states) is given by [28]:

$$\hat{H} = \left[\frac{\hbar^2 \hat{\mathbf{k}}^2}{2m} + V(\mathbf{r}) \right] \check{1} + \alpha(\check{\sigma}_x \hat{k}_y - \check{\sigma}_y \hat{k}_x) + \beta(\check{\sigma}_x \hat{k}_y + \check{\sigma}_y \hat{k}_x) + \frac{\Delta_z}{2} \check{\sigma}_z, \quad (2.15)$$

where α and β denote strengths of Rashba and Dresselhaus couplings respectively (in this scheme, α is fixed and β can be tuned), and Δ_z is an effective Zeeman field. Per the same arguments as in the tripod scheme, we are allowed to simply replace $V \rightarrow V(t)$ in (2.15) (if an external potential is time-dependent; note also, that the trapping potential here is spin independent). The rotating trap potential reads: $V(\mathbf{r}, t) = e^{-i\omega_r t \hat{L}_z / \hbar} V(\mathbf{r}) e^{i\omega_r t \hat{L}_z / \hbar}$. We now make the following transformation: $\hat{U}(t) = \exp[i\omega_r t (\hat{L}_z / \hbar + \check{\sigma}_z / 2)]$, which gives:

$$\begin{aligned} \hat{H}' = & \left[\frac{\hbar^2 \hat{\mathbf{k}}^2}{2m} + V(\mathbf{r}) - \omega_r \hat{L}_z \right] \check{1} + \alpha (\check{\sigma}_x \hat{k}_y - \check{\sigma}_y \hat{k}_x) + \left(\frac{\Delta_z}{2} - \frac{\hbar \omega_r}{2} \right) \check{\sigma}_z \\ & + \beta \left\{ [\check{\sigma}_y \cos(2\omega_r t) + \check{\sigma}_x \sin(2\omega_r t)] \hat{k}_x + [\check{\sigma}_x \cos(2\omega_r t) - \check{\sigma}_y \sin(2\omega_r t)] \hat{k}_y \right\}. \end{aligned} \quad (2.16)$$

Again, this *non-interacting part* of the Hamiltonian is in general time-dependent, however for pure Rashba coupling ($\beta = 0$), it becomes time-independent.

Note that to get the full Hamiltonian in the rotating frame, we must also include interactions between the bosons and apply to them the same transformations as in the non-interacting part above. If both the trap and spin-orbit lasers rotate, the corresponding unitary operator, $\hat{U}(t) = \exp[i\omega_r t (\hat{L}_z + \hat{S}_z) / \hbar]$, describes a spatial rotation about the z-axis. If the bare interactions are rotationally-invariant, the interaction part of the Hamiltonian does not change in the rotating frame. In contrast to this result however, if only the trap is rotating, the interactions will generally acquire time-dependence as well (we have found a few very special cases - with serious constraints on the parameters of the system - where a unitary transform can be found that makes both the pure Rashba non-interacting part and interactions

time-independent, but whether these degenerate cases can be realized experimentally remains unclear at this stage).

2.3 Creating vortices by rotation

In the previous section, we have shown that the Hamiltonian for the M-scheme in the presence of a rotating trap and Raman lasers becomes time-independent in the rotating frame. In analogy with the physics of “ordinary” BEC under rotation, there will be thermal equilibration in the system and vortices will form in the condensate.

Let us assume that the trapping frequency in \hat{z} direction ω_z is so large that the system is an effective 2D system, where the motion in \hat{z} direction is effectively frozen (this can be achieved by applying a 1D optical lattice in \hat{z} direction). We also assume the interaction part of the Hamiltonian to have the form:

$$\hat{H}_{int} = \int d^2r \left(\frac{1}{2}G_1\hat{\rho}_\uparrow^2 + \frac{1}{2}G_2\hat{\rho}_\downarrow^2 + G_{12}\hat{\rho}_\uparrow\hat{\rho}_\downarrow \right), \quad (2.17)$$

where G_1 , G_2 and G_{12} are effective 2D interaction strengths and are related to 3D interaction strengths: $G_1 = G_1^{3d}/(\sqrt{2\pi}l_z)$, $G_2 = G_2^{3d}/(\sqrt{2\pi}l_z)$ and $G_{12} = G_{12}^{3d}/(\sqrt{2\pi}l_z)$, where $l_z = \sqrt{\hbar/(m\omega_z)}$. $\hat{\rho}_\uparrow$ and $\hat{\rho}_\downarrow$ are density operators for $|\uparrow\rangle$, $|\downarrow\rangle$ states (normal ordering of the corresponding creation/annihilation operators is implied).

We are interested in finding the ground state configuration of bosons in a rotating system described by (2.7,2.17). First, we have to make an assumption about the ground state and we assume below that (at the mean-field level) all atoms occupy the same single-particle state described by the spinor wave-function, $(\psi_\uparrow(\mathbf{r}), \psi_\downarrow(\mathbf{r}))$ (we also call it condensate wave-function). The condensate wave-function satisfies

the Gross-Pitaevskii (GP) equations below:

$$\begin{aligned}
\mu\psi_{\uparrow} = & \left[-\frac{\hbar^2}{2m}\nabla^2 - i\frac{\hbar^2 k_L}{m}\frac{\partial}{\partial x} + V(\mathbf{r}) - \omega_r(\hat{L}_z - \hbar k_L y) \right. \\
& \left. + NG_1|\psi_{\uparrow}|^2 + NG_{12}|\psi_{\downarrow}|^2 \right] \psi_{\uparrow} + \frac{\Omega}{2}\psi_{\downarrow} \\
\mu\psi_{\downarrow} = & \left[-\frac{\hbar^2}{2m}\nabla^2 + i\frac{\hbar^2 k_L}{m}\frac{\partial}{\partial x} + V(\mathbf{r}) - \omega_r(\hat{L}_z + \hbar k_L y - \hbar) \right. \\
& \left. - \delta + NG_2|\psi_{\downarrow}|^2 + NG_{12}|\psi_{\uparrow}|^2 \right] \psi_{\downarrow} + \frac{\Omega}{2}\psi_{\uparrow} \quad (2.18)
\end{aligned}$$

where N is the total number of particles and μ is the Lagrange multiplier associated with the constraint $\int d^2r (|\psi_{\uparrow}|^2 + |\psi_{\downarrow}|^2) = 1$ (it can be shown that μ has a physical meaning of chemical potential [35]). We solve the GP equations by using norm-preserving imaginary time propagation method (see for example Ref. [37, 39]).

We consider a trapping potential of the following form: $V = \frac{1}{2}m\omega^2(x^2 + \gamma^2 y^2)$, where ω and $\gamma\omega$ are trapping frequencies in the \hat{x} and \hat{y} direction. It is convenient to measure lengths in the units of the harmonic oscillator length, $a_0 = \sqrt{\hbar/(m\omega)}$ and energy in terms of $\hbar\omega$. If we introduce dimensionless position variable $\mathbf{r}' = \mathbf{r}/a_0$, the corresponding ‘‘dimensionless GP equations’’ read

$$\begin{aligned}
\mu\psi_{\uparrow} = & \left[-\frac{1}{2}\nabla'^2 - ik'_L\frac{\partial}{\partial x'} + \frac{1}{2}(x'^2 + \gamma^2 y'^2) \right. \\
& \left. - \omega'_r(\hat{L}'_z - k'_L y') + g_1|\psi_{\uparrow}|^2 + g_{12}|\psi_{\downarrow}|^2 \right] \psi_{\uparrow} + \frac{\Omega'}{2}\psi_{\downarrow} \\
\mu\psi_{\downarrow} = & \left[-\frac{1}{2}\nabla'^2 + ik'_L\frac{\partial}{\partial x'} + \frac{1}{2}(x'^2 + \gamma^2 y'^2) - \delta' \right. \\
& \left. - \omega'_r(\hat{L}'_z + k'_L y' - 1) + g_2|\psi_{\downarrow}|^2 + g_{12}|\psi_{\uparrow}|^2 \right] \psi_{\downarrow} + \frac{\Omega'}{2}\psi_{\uparrow}, \quad (2.19)
\end{aligned}$$

where $k'_L = k_L a_0$, $\Omega' = \Omega/(\hbar\omega)$, $\delta' = \delta/(\hbar\omega)$, $\omega'_r = \omega_r/\omega$, $\hat{L}_z = -i(x'\partial_{y'} - y'\partial_{x'})$, $g_1 = NG_1/(\hbar\omega a_0^2)$, $g_2 = NG_2/(\hbar\omega a_0^2)$ and $g_{12} = NG_{12}/(\hbar\omega a_0^2)$.

In simulations for the rotating system we consider ^{87}Rb atoms and we use the experimentally-relevant parameters: $\lambda = 804.1$ nm, $\omega = 2\pi \times 50$ Hz and $\gamma = 1$. These parameters give $a_0 = \sqrt{\hbar/m\omega} = 1.52$ μm , $k'_L = 8.42$. From now on we express length in units of a_0 and momentum \mathbf{k} in units of $1/a_0$ (coordinates (x, y) and (k_x, k_y) in figures are also given in the units of a_0 and $1/a_0$). We performed simulations specifically for the rotation frequency $\omega_r = 0.7 \omega$ and for three different coupling strengths: no coupling ($\Omega = 0$), weak coupling ($\Omega = 2 E_L$), and strong coupling ($\Omega = 10 E_L$), where $E_L = \hbar^2 k_L^2/2m$ is the recoil energy ($E_L = 35.4 \hbar\omega$). In simulations we choose $g_1 = 1000$, $g_2 = 995$, $g_{12} = 995$. The ratio between g_1 , g_2 and g_{12} corresponds to interaction coefficients in ^{87}Rb (the interaction coefficients for ^{87}Rb in states $\{|F = 1, m = 0\rangle, |F = 1, m = -1\rangle\}$ are given in Ref. [7]). If we assume $\omega_z = 2\pi \times 2$ kHz, the number of particles corresponding to chosen interaction coefficients is $N \approx 10^4$. We also set $\delta - \hbar\omega_r = 0$.

Without rotation and spin-orbit coupling, $|\uparrow\rangle$ and $|\downarrow\rangle$ components are miscible for our choice of interaction parameters. In the case of rotation and no spin-orbit coupling there are several different phases depending on ω_r and ratio of interaction coefficients [40]: triangular lattice, square lattice, stripe or double-core vortex lattice and vortex sheet. Since our Hamiltonian is almost equivalent to the Hamiltonian in Ref. [40] for $\Omega = 0$ and $\delta - \hbar\omega_r = 0$ (there is a very small difference in interaction coefficients; the equivalence of non-interaction part of two systems is clear from Eq.(A.3)) we reproduced results of Ref. [40].

The results for $\Omega = 0$ are shown in Fig. 2.1(a), which displays densities of the $|\uparrow\rangle$ and $|\downarrow\rangle$ components forming spatially-separated density stripes with lines of vortices along the minima of the density. As expected, our results reproduce stripe vortex lattice phase described in Ref. [40]. Note that for $\Omega = 0$, the Hamiltonian (2.7) conserves number of the $|\uparrow\rangle$ and $|\downarrow\rangle$ particles separately. We have chosen $N_\uparrow = N_\downarrow$ ($N_i = \int d^2r |\psi_i|^2$).

A weak spin-orbit coupling ($\Omega = 2 E_L$) (Fig. 2.1(b)) does not appear to lead to significant qualitative changes in the observed behavior: densities of the $|\uparrow\rangle$ and $|\downarrow\rangle$ components are still spatially separated and there are lines of vortices along the density minima of each component.

A significant change comes in the strong-coupling regime: see the $\Omega = 10 E_L$ data shown in Fig. 2.1(c). The vortices arrange themselves in a lattice in $|\uparrow\rangle$ and $|\downarrow\rangle$ components and densities of both components are almost identical. This behavior can be understood from the following part of the Hamiltonian (2.7):

$$\hat{H}' = \frac{\hbar^2 \hat{k}_x^2}{2m} \check{1} + \frac{\hbar^2 k_L \hat{k}_x}{m} \check{\sigma}_z + \frac{\Omega}{2} \check{\sigma}_x. \quad (2.20)$$

The spectrum of (2.20) for different Ω 's is shown in Fig. 1.5(a). For large Ω , it consists of two bands with an energy separation much larger than all other characteristic energies of the system. Therefore, our system is “confined” to the lower band with a single minimum, which effectively makes it a single-component system. This explains almost identical densities of the two components in Fig. 2.1(c).

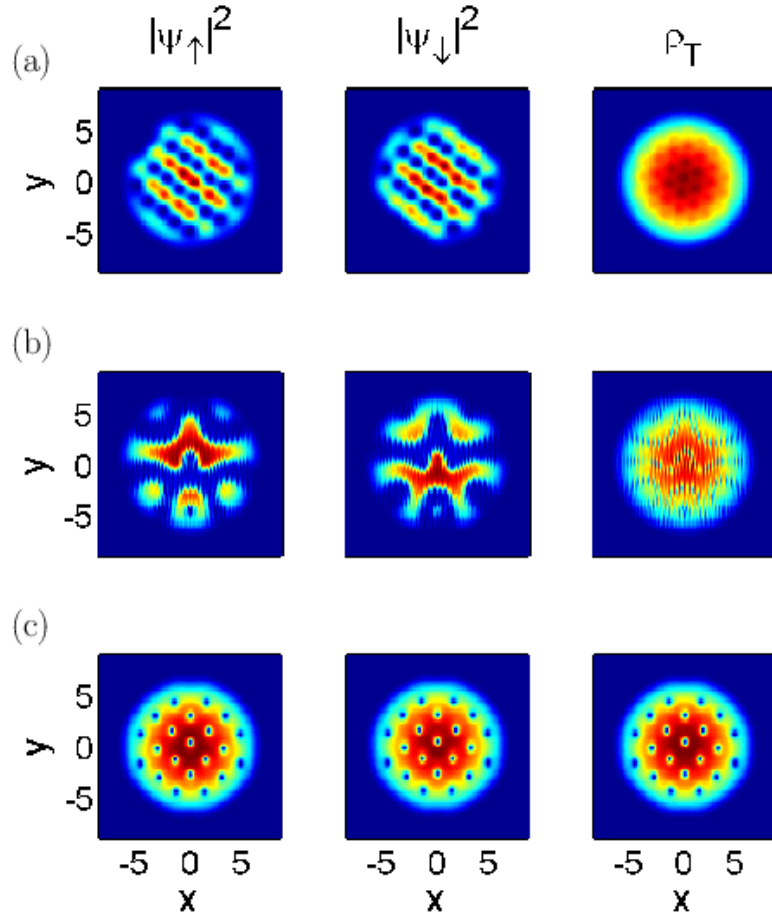


Figure 2.1: The density profiles for the rotating spin-orbit-coupled BEC are shown. The first, second and third columns show density of $|\uparrow\rangle$ component ($|\psi_\uparrow|^2$), density of $|\downarrow\rangle$ component ($|\psi_\downarrow|^2$) and the total density ($\rho_T = |\psi_\uparrow|^2 + |\psi_\downarrow|^2$), respectively. Figure (a) shows results for $\Omega = 0$ which are characterized by density stripes and lines of vortices in both components. The results for $\Omega = 2 E_L$ (b) are qualitatively similar to the $\Omega = 0$ case. Figure (c) shows results for $\Omega = 10 E_L$; a vortex lattice is formed in both components and densities of the two components are almost identical.

2.4 Creating vortices by spatially-dependent detuning

2.4.1 The model

Vortices in spin-orbit systems like [7] can be created without any rotation, but by imposing an additional synthetic magnetic field. In [41], it has been shown that a spatially-dependent detuning, δ , in the M-scheme results in a synthetic magnetic field, which creates vortices in the strong Raman coupling (Ω) regime. Our goal is to investigate the same system for a wide range of Ω (from weak to strong Raman coupling) and to see what kind of vortex structures it yields.

The setup is described by the following effective Hamiltonian (see [7, 41]):

$$\hat{H} = \left(\frac{\hbar^2 \hat{\mathbf{k}}^2}{2m} + V \right) \check{1} + \frac{\hbar^2 k_L \hat{k}_x}{m} \check{\sigma}_z + \frac{\Omega}{2} \check{\sigma}_x + \frac{\delta(y)}{2} \check{\sigma}_z, \quad (2.21)$$

where spatially-dependent $\delta(y)$ can be created in a laboratory by applying spatially-dependent magnetic field (see [14]).

We again assume strong confinement in the \hat{z} direction and describe interactions by equation (2.17). We are looking for the ground state in the same way as in the rotating case and following the same steps we get the “dimensionless GP equations”:

$$\begin{aligned} \mu \psi_{\uparrow} = & \left[-\frac{1}{2} \nabla'^2 - ik'_L \frac{\partial}{\partial x'} + \frac{1}{2} (x'^2 + \gamma^2 y'^2) \right. \\ & \left. + \frac{\delta'(y')}{2} + g_1 |\psi_{\uparrow}|^2 + g_{12} |\psi_{\downarrow}|^2 \right] \psi_{\uparrow} + \frac{\Omega'}{2} \psi_{\downarrow} \end{aligned}$$

$$\mu\psi_{\downarrow} = \left[-\frac{\hbar^2}{2m}\nabla'^2 + ik'_L\frac{\partial}{\partial x'} + \frac{1}{2}(x'^2 + \gamma^2 y'^2) - \frac{\delta'(y')}{2} + g_2|\psi_{\downarrow}|^2 + g_{12}|\psi_{\uparrow}|^2 \right] \psi_{\downarrow} + \frac{\Omega'}{2}\psi_{\uparrow}. \quad (2.22)$$

Parameters Ω' , δ' , k'_L , g_1 , g_2 , g_{12} are defined in the same way as in (2.19). Equations (2.22) are solved using the same method as in Sec. 2.3.

2.4.2 Qualitative discussion

To get a better understanding of the model, we investigate Hamiltonian (2.21) in more detail. It is instructive to first focus on the following part of (2.21):

$$\hat{H}' = \frac{\hbar^2 \hat{k}_x^2}{2m} \check{1} + \frac{\hbar^2 k_L \hat{k}_x}{m} \check{\sigma}_z + \frac{\Omega}{2} \check{\sigma}_x + \frac{\delta}{2} \check{\sigma}_z. \quad (2.23)$$

We first assume that δ is constant in space. In that case Hamiltonian (2.23) can be easily diagonalized in the momentum basis: $U^\dagger(k_x)H'(k_x)U(k_x) = \begin{pmatrix} E_+(k_x) & 0 \\ 0 & E_-(k_x) \end{pmatrix}$. The resulting spectrum consists of an upper(+) and lower(-) band, as shown in Fig. 1.5. The gap separating the bands is large compared to other characteristic energies of the system and it is safe to assume that the condensate occupies only the states in the lower band. In Fig. 1.5(a), spectra for different coupling strengths Ω and $\delta = 0$ are shown. For $\Omega < 4 E_L$, the spectrum has two minima and BEC will involve states near both left and right minima. At $\Omega = 4 E_L$, there is a transition from a spectrum with two minima to a spectrum with one minimum, which changes the structure of the condensate wave-function. I.e., for $\Omega > 4 E_L$, the BEC is expected to occupy only states with momentum around $k_x = 0$.

The effect of detuning δ in the low- Ω regime is shown in Fig. 1.5(b). We see

that δ shifts the energies and positions of the left and right minima. In the case of constant δ , the BEC would occupy only the states around the global minimum (for example, the right minimum in Fig. 1.5(b)). Those cases have been tested experimentally in [7]. Now, consider a spatially-dependent $\delta(y)$. We will consider it to be a linear function of y : $\delta(y) = \delta_0 + \beta y$, which is the simplest and the most experimentally relevant regime. The interesting physics is evident from the following arguments: for constant detuning, the spectrum around a minimum can be simply described by $(k_x - k_{\min})^2/(2m_{\text{eff}}) + E_{\min}$ [we use dimensionless variables, see (2.19)], where m_{eff} , k_{\min} , E_{\min} are the effective mass, position of the minimum, and the energy at the minimum, respectively. Note that all these quantities depend on δ . If δ is y -dependent, the values of m_{eff} , k_{\min} , E_{\min} will also become spatially-dependent. Hence, the spectrum around the minimum can now be written as: $[k_x - k_{\min}(y)]^2/(2m_{\text{eff}}) + E_{\min}(y)$ which describes particles moving in an effective gauge field $(\mathbf{A}, \Phi) = (k_{\min}(y), 0, 0, E_{\min}(y))$ with a spatially-varying effective mass $m_{\text{eff}}(y)$ [41]. The spatially-dependent vector potential \mathbf{A} induces an effective magnetic field ($\mathbf{B}_{\text{eff}} = \nabla \times \mathbf{A}$), which may lead to creation of vortices if strong enough. This approximation provides a good description of the system only if the particles at some point y have the momentum k_x near the minimum. Our numerical simulations presented below indicate that this approximation in fact gives a very good qualitative description in a wide parameter range.

We calculate parameters $m_{\text{eff}}(y)$, $k_{\min}(y)$, and $E_{\min}(y)$ by diagonalizing (2.23) for different y 's since $\delta = \delta(y)$. The procedure of deriving effective equations for lower band for Hamiltonian (2.21) in high Ω (single minimum) regime is described

in Ref. [41]. Let us note however, that the method we use to find the ground state, i.e. numerically solving equations (2.22), is exact (in particular, we do not limit our system to lower band and we do not simplify interaction terms).

2.4.3 Results

In simulations for a system with a spatially-dependent detuning δ we use the same experimental parameters as in the simulations of a rotating system, which gives $a_0 = \sqrt{\hbar/(m\omega)} = 1.52 \mu\text{m}$ and $k'_L = 8.42$. We choose interaction parameters to be $g_1 = 1600$, $g_2 = 1593$, $g_{12} = 1593$ and constant part of detuning $\delta_0 = 0$. The results for $\Omega = 0$, $\beta = 4 \hbar\omega/a_0$ and $\gamma = 1$ are shown in Fig. 2.2. Here we have chosen $N_\uparrow = N_\downarrow$ since for $\Omega = 0$ Hamiltonian conserves number of the $|\uparrow\rangle$ and $|\downarrow\rangle$ particles separately. The results are straightforward to understand, i.e. in this case, we can write the Hamiltonian (2.21) as

$$\hat{H} = \begin{pmatrix} H_\uparrow & 0 \\ 0 & H_\downarrow \end{pmatrix}, \quad (2.24)$$

where $H_\uparrow = \frac{\hbar^2}{2m} (\hat{\mathbf{k}}^2 + 2k_L \hat{k}_x) + V_\uparrow(\mathbf{r})$, $H_\downarrow = \frac{\hbar^2}{2m} (\hat{\mathbf{k}}^2 - 2k_L \hat{k}_x) + V_\downarrow(\mathbf{r})$ and $V_\uparrow(\mathbf{r}) = V(\mathbf{r}) + \delta(y)/2$, $V_\downarrow(\mathbf{r}) = V(\mathbf{r}) - \delta(y)/2$. We see that motion of $|\uparrow\rangle$ and $|\downarrow\rangle$ particles is decoupled in \hat{H} and that they experience different potentials $V_\uparrow(\mathbf{r})$, $V_\downarrow(\mathbf{r})$. Detuning gradient β shifts the minima of $V_\uparrow(\mathbf{r})$ ($V_\downarrow(\mathbf{r})$) for $y_0 = \beta/(2m\omega^2\gamma^2)$ in the positive/negative \hat{y} direction and therefore, the centers of the $|\uparrow\rangle$ and $|\downarrow\rangle$ densities are shifted from the origin by $\pm y_0$ (the origin is located in the minimum of $V(\mathbf{r})$), see Fig. 2.2(b). Also, it is clear from \hat{H} and Fig. 1.5(a) that the momentum dis-

tribution of $|\uparrow\rangle$ ($|\downarrow\rangle$) particles will be centered around $\mathbf{k} = (-k_L, 0)$ ($\mathbf{k} = (k_L, 0)$), see Fig. 2.2(c) (in dimensionless units k_L is simply replaced by k'_L). The effect of repulsive interactions between the particles with different spins is clearly seen (the overlap between $|\uparrow\rangle$ and $|\downarrow\rangle$ densities is quite small).

If we introduce a finite Ω , the Hamiltonian becomes: $\hat{H} = \begin{pmatrix} H_\uparrow & \Omega/2 \\ \Omega/2 & H_\downarrow \end{pmatrix}$, i.e. Ω -term creates coupling between $|\uparrow\rangle$ and $|\downarrow\rangle$ particles. If $\delta = \text{const} = 0$ and Ω is small, the states around the left (right) minimum in the spectrum in Fig. 1.5(a) still consist mainly of the $|\uparrow\rangle$ ($|\downarrow\rangle$) particles, but there is also some admixture of the component with the opposite spin, which grows with Ω . It means that $\psi_\uparrow(\mathbf{r})$ ($\psi_\downarrow(\mathbf{r})$) will mainly consist of states with momentum around the left (right) minimum, but also of states around the right (left) minimum. We can therefore write:

$$\begin{pmatrix} \psi_\uparrow(\mathbf{r}) \\ \psi_\downarrow(\mathbf{r}) \end{pmatrix} = \begin{pmatrix} \psi_{\uparrow L}(\mathbf{r}) \\ \psi_{\downarrow L}(\mathbf{r}) \end{pmatrix} + \begin{pmatrix} \psi_{\uparrow R}(\mathbf{r}) \\ \psi_{\downarrow R}(\mathbf{r}) \end{pmatrix}, \quad (2.25)$$

where $\psi_{\uparrow L}(\mathbf{r})$ and $\psi_{\downarrow L}(\mathbf{r})$ consist only of states with momenta around the left peak, while $\psi_{\uparrow R}(\mathbf{r})$ and $\psi_{\downarrow R}(\mathbf{r})$ consist only of the states with momenta around the right peak of the momentum distribution. We therefore call $(\psi_{\uparrow L}, \psi_{\downarrow L})$ and $(\psi_{\uparrow R}, \psi_{\downarrow R})$ the left and right wave-function. In the spatially-dependent detuning case it may happen that momentum distribution is separated in two peaks (i.e., there exist “left”- and “right-movers”) even for $\Omega > 4 E_L$ (see for example Fig. 2.6(c)). In that case also the notion of left and right wave-function applies.

To investigate the effect of Ω , which couples $|\uparrow\rangle$ and $|\downarrow\rangle$ states, we consider the regime with $\Omega = 3 E_L$ and $\beta = 8 \hbar\omega/a_0$ (Fig. 2.3). The total density $\rho_T(\mathbf{r})$ is shown in Fig. 2.3(a) and there is a characteristic series of minima along the \hat{x}

direction at $y = 0$, which come from vortices in the ψ_\uparrow and ψ_\downarrow wave-functions, see Fig. 2.3(b), which are positioned along x and near $y = 0$. We have checked that the phase winding around zero density points of ψ_\uparrow and ψ_\downarrow is -2π . Since vortices in $|\downarrow\rangle$ and $|\uparrow\rangle$ components are slightly displaced from $y = 0$, the density at minima in ρ_T are close to, but not exactly equal to zero.

To explain the existence of the line of vortices in the $|\uparrow\rangle$ and $|\downarrow\rangle$ components, we examine the left and right wave-functions. Fig. 2.4(a) displays $|\psi_{\uparrow L}|^2$ and $|\psi_{\uparrow R}|^2$ (note that the amplitude of $\psi_{\uparrow R}$ is considerably smaller than the amplitude of $\psi_{\uparrow L}$: $\int d^2r |\psi_{\uparrow R}|^2 = 0.05$ and $\int d^2r |\psi_{\uparrow L}|^2 = 0.45$). The momentum distribution in Fig. 2.3(c) shows that the wave-packet, $\psi_{\uparrow L}$, has an average momentum of $k_{\text{left}} = -0.8 k'_L$ and $\psi_{\uparrow R}$ has an average momentum of $k_{\text{right}} = 0.8 k'_L$. Since ψ_\uparrow is a superposition of the left- and right-movers, $\psi_\uparrow = \psi_{\uparrow L} + \psi_{\uparrow R}$, the appearance of the line of vortices at overlapping region is expected. The separation of vortices d is then simply given by $(k_{\text{right}} - k_{\text{left}})d = 2\pi$ or $d = 2\pi/(k_{\text{right}} - k_{\text{left}})$. The analytical expression for d fits perfectly well to our numerical data.

To explain the density profile and momentum distribution, it is useful to consider an effective gauge-field picture. The effective gauge field (\mathbf{A}, Φ) , where $\mathbf{A} = (k_{\text{min}}(y), 0, 0)$ and $\Phi = E_{\text{min}}(y)$ can be calculated by diagonalizing H' . From now on we use the following notation: $A(y) = k_{\text{min}}(y)$ and $\Phi(y) = E_{\text{min}}(y)$. As discussed earlier, we may approximate the low-energy band physics by the following Hamiltonian (we use again the dimensionless variables, where the lengths are

measured in terms of a_0 and the wave-vectors, k , in terms of $1/a_0$):

$$H_{\text{EGF}} = \frac{1}{2m_{\text{eff}}(y)} [k_x - A(y)]^2 + \frac{1}{2}k_y^2 + \Phi(y) + V(\mathbf{r}), \quad (2.26)$$

where $V(\mathbf{r}) = \frac{1}{2}(x^2 + \gamma^2 y^2)$. For $\Omega \geq 4E_L$ there is a single local minimum in lower band of the Hamiltonian (2.23) spectrum for any δ . For $\Omega < 4E_L$ the spectrum has two minima for $\delta = 0$, however when δ becomes large enough the spectrum has a single local minimum (Fig. 1.5(b)). The spectrum around each local minimum can be approximated by the form given in (2.26), and therefore there will be $A_L(y)$, $\Phi_L(y)$, $m_{\text{eff,L}}(y)$ corresponding to the left minimum and $A_R(y)$, $\Phi_R(y)$, $m_{\text{eff,R}}(y)$ corresponding to the right minimum of the spectrum. Left-movers feel the “left gauge field” $(A_L(y), 0, 0, \Phi_L(y))$ while right-movers feel the “right gauge field” $(A_R(y), 0, 0, \Phi_R(y))$.

To get the effective potential in \hat{y} direction acting on left- and right-movers we define: $V_{\text{eff,L}}(y) = \Phi_L(y) + \frac{1}{2}\gamma^2 y^2$, $V_{\text{eff,R}}(y) = \Phi_R(y) + \frac{1}{2}\gamma^2 y^2$. In Fig. 2.5 we show $\Phi_{\text{L/R}}(y)$, $V_{\text{eff,L/R}}(y)$, $A_{\text{L/R}}(y)$ and $1/m_{\text{eff,L/R}}(y)$ for $\Omega = 3 E_L$ and $\beta = 8 \hbar\omega/a_0$. $V_{\text{eff,L/R}}$ have minima at $y_{0,R/L} = \pm 3.2$ which explains the total density profile (Fig. 2.3(a)) which has maxima at $y = \pm 3.2$. The position of two peaks in momentum distribution in Fig. 2.3(c) can be understood as follows: for particles positioned near the minimum of $V_{\text{eff,L}}$ in Fig. 2.5(b), it is energetically favorable to have the \hat{x} -component of momentum approximately equal to $A(y_{0,L})$ and the \hat{y} -component near zero (see equation (2.26)). Fig. 2.5(c) shows that $A(y_{0,L}) \approx -0.79 k'_L$, while from Fig. 2.3 (c), we see that the momentum distribution is centered around $k_x = -0.80 k'_L$. The same explanation applies for the momentum distribution

of right-movers.

To investigate the regime with a single minimum in the spectrum ($\Omega \geq 4 E_L$) we did calculations for parameters: $\Omega = 5 E_L$, $\beta = 12 \hbar\omega/a_0$ and $\gamma = 1$ (Fig. 2.6). In this “single-minimum” case one might expect momentum distribution to be concentrated around a single point as was observed in Ref. [7]. However, in spatially-dependent-detuning case this is not necessarily true: the momentum distribution (Fig. 2.6(c)) shows two peaks around $k_x = \pm 0.55 k'_L$. Also, the total density (Fig. 2.6(a)) has a characteristic series of minima along $y = 0$ line which come from vortices in the ψ_\uparrow and ψ_\downarrow wave-functions (Fig. 2.6(b)) created in the overlapping region of left- and right-movers. The results can again be explained by the effective gauge field. The effective potential in \hat{y} direction $V_{\text{eff}}(y) = \Phi(y) + \frac{1}{2}\gamma^2 y^2$ (Fig. 2.7(a)) has two minima at $y_{0,R/L} = \pm 3.4$ which explains the density distribution which has maxima at $y = \pm 3.3$. Also, equation (2.26) tells us it is energetically favourable for particles near the left (right) minimum of $V_{\text{eff}}(y)$ to have momentum around $A(y_{0,L}) = -0.56 k'_L$ ($A(y_{0,R}) = 0.56 k'_L$) (Fig. 2.7(c)) which explains momentum distribution. We also note that in Fig. 2.7(c) $A(y)$ has a large gradient and therefore magnetic field ($B_{\text{eff}} \sim \partial A/\partial y$) is strong around $y = 0$ which may serve as an alternative explanation of line of vortices appearing in Fig. 2.6(a).

We now study the system with strong Raman coupling Ω and weak detuning gradient β (i.e. β is not large enough to produce spatial separation of a cloud along \hat{y} as in previous cases). Results for $\Omega = 10 E_L$, $\beta = 12 \hbar\omega/a_0$ are shown in Fig. 2.8 and can be explained by the associated effective gauge field shown in Fig. 2.9. The total density (Fig. 2.8(a)) and $|\psi_\uparrow|^2$, $|\psi_\downarrow|^2$ (Fig. 2.8(b)) show the existence of a vortex

in the centre of the cloud. The vortex appears only for strong enough effective magnetic field which is tuned by changing β . We define the effective magnetic field $\mathbf{B}_{\text{eff}} = \nabla \times \mathbf{A}(y)$ and in our case, ($\mathbf{A} = (A(y), 0, 0)$), $\mathbf{B}_{\text{eff}} = -\frac{\partial A(y)}{\partial y} \hat{z}$. The magnetic field points in the \hat{z} direction, depends on y , and is constant along x . We also note that since $m_{\text{eff}}(y) \neq 1$ (Fig. 2.9(d)), the effective equations will differ from those for an ordinary charged particle in a magnetic field $B_{\text{eff}}(y)\hat{z}$. The vector potential $A(y)$ and the effective magnetic field $\mathbf{B}_{\text{eff}}(y)$ are shown in Fig. 2.9(b,c).

It is useful to know the critical field needed for vortex creation and we can get a crude estimate by using the equation for critical magnetic field of a single-component 2D gas in the Thomas-Fermi limit: $B_c = 4(a_0/R)^2 \ln(0.888(R/a_0)^2)$, where R is the Thomas-Fermi radius of the cloud [42]. We choose $R = 6.5 a_0$ (the size of our cloud), which gives $B_c \approx 0.35$. It is important to notice that larger number of particles or stronger interactions increase R , which lowers the critical field (B_c decreases with increasing R). To find B_c , we did simulations for $\Omega = 10 E_L$, $\gamma = 1$ and for different values of β (which controls the strength of the effective magnetic field). We found that the vortices start to appear for a critical effective magnetic field $B_c \approx 0.34$, which is very close to our estimate presented above.

If the effective field is strong enough, a vortex “lattice” is formed, as shown in Fig. 2.10, which corresponds to $\Omega = 10 E_L$, $\beta = 40 \hbar\omega/a_0$ and $\gamma = 1.85$. From the figure, we see that vortices are concentrated along the x -axis and around $y = 0$. This is because $B_{\text{eff}}(y)$ is not homogeneous, i.e. the field is strongest at $y = 0$ and it weakens with increasing $|y|$. We had to increase trapping strength in the \hat{y} direction ($\gamma = 1.85$) because scalar potential $\Phi(y)$ separates the clouds (e.g. see Fig. 2.7(a))

and for a weaker trapping strength, the effective potential would have two minima (it would look like effective potential in Fig. 2.7(b)).

The most interesting regime is the one in which left and right moving phases $(\psi_{\uparrow L}(\mathbf{r}), \psi_{\downarrow L}(\mathbf{r}))$ and $(\psi_{\uparrow R}(\mathbf{r}), \psi_{\downarrow R}(\mathbf{r}))$ are spatially separated along \hat{y} direction and there is a vortex (or vortices) in each phase in addition to a vortex line. This requires double minimum structure of the effective potential in \hat{y} direction $V_{\text{eff}}(y)$, which separates the phases and strong enough effective magnetic field in each phase to create additional vortices, which tend to appear in pairs (i.e. the number of vortices is equal in both phases which is a consequence of the fact that in our simulations the effective gauge field is symmetric with respect to reflection about $y = 0$ line and interactions are almost spin-independent).

In Fig. 2.11(a), we show results for $\omega = 2\pi \times 10$ Hz, $\Omega = 4 E_L$, $\beta = 20 \hbar\omega/a_0$ ($a_0 = \sqrt{\hbar/(m\omega)}$). By choosing $\omega = 2\pi \times 10$ Hz, parameter k'_L in dimensionless GP equations (2.22) becomes $k'_L = 18.83$, while interaction coefficients stay the same ($g_1 = 1600$, $g_2 = 1593$ and $g_{12} = 1593$). Having larger k'_L means we can create stronger effective magnetic field. We increased the trapping frequency in the \hat{y} direction ($\gamma = 1.3$) to bring two phases closer to $y = 0$, where the effective magnetic field is stronger (to counter the effective scalar potential $\Phi(y)$, which separates the phases). In Fig. 2.11(b) we show results for $\omega = 2\pi \times 10$ Hz, $\Omega = 10 E_L$, $\beta = 150 \hbar\omega/a_0$ and $\gamma = 2.75$. Here the left and right phases are completely separated in space and the effective magnetic field is strong enough to produce multiple vortices in each phase. Also, it is clear that the vortices are not located in centers of two phases, but are positioned closer to $y = 0$ which is expected because the field is

stronger near $y = 0$.

2.4.4 Experimental signatures

It is important to discuss the means of experimentally observing results we presented. We concentrate on the time-of-flight imaging, which is widely used to probe cold-atoms systems. The time-of-flight picture here will be determined by the underlying momentum distribution of particles. If the momentum distribution consists of two separated peaks, the initial cloud will strongly separate during expansion (see for example [7, 14]). We note that due to the transformation $\psi'_\uparrow(\mathbf{r}) = \psi_\uparrow(\mathbf{r})e^{-ik_Lx}$, $\psi'_\downarrow(\mathbf{r}) = \psi_\downarrow(\mathbf{r})e^{ik_Lx}$ used when deriving Hamiltonian (2.21), the real momentum distribution of $|\uparrow\rangle$ particles will in fact be shifted by k_L with respect to the momentum distribution shown in figures and the momentum distribution of $|\downarrow\rangle$ particles is shifted by $-k_L$ (see [7]). In the case of $\Omega = 0$, both $|\uparrow\rangle$ and $|\downarrow\rangle$ particles will have zero average momentum, which means both components of the condensate will expand, while the position of centre of mass will be stationary during time-of-flight. For $\Omega = 3 E_L$ and $\beta = 8 \hbar\omega/a_0$, we expect four separated clouds to be seen in the time-of-flight: since the real momentum distributions of $|\uparrow\rangle$ and $|\downarrow\rangle$ particles are shifted by k_L and $-k_L$, there will be two clouds of $|\uparrow\rangle$ particles with average momenta of $0.2 k_L$ (larger cloud) and $1.8 k_L$ (smaller cloud) and two clouds of $|\downarrow\rangle$ particles with average momenta of $-0.2 k_L$ (larger cloud) and $-1.8 k_L$ (smaller cloud). It is important to notice that the vortex line will not be easily visible in those images, because it exists only due to the the overlap of the wave-packets with

different average momenta. During the time-of-flight, two wave-packets $(\psi_{\uparrow L}, \psi_{\uparrow R})$ or $(\psi_{\downarrow L}, \psi_{\downarrow R})$ separate, which means that they do not overlap any more and there is no clear vortex line present. For the case in Fig. 2.11, the vortices in each phase will be visible since they are not a result of overlapping the left- and right-moving condensates.

2.5 Conclusion

In this work, we have investigated realistic experimental methods that can be used to create vortex excitations in spin-orbit-coupled Bose-Einstein condensates. The main conclusion of the work is that due to a complicated interplay between effects associated with the applied laser fields and rotation, the resulting state of the spin-orbit BEC under additional perturbations is highly non-universal and depends strongly on the system parameters and specific laser schemes. In particular, we argued that a spin-orbit BEC under rotation of the trap alone does not achieve a thermodynamically stable state at all, but acquires a complicated non-equilibrium dynamics that eventually leads to heating and the destruction of the condensate.

We have also suggested two alternative experimental methods to mimic an Abelian “orbital” magnetic field that involve either rotation of the entire experimental setup, or a spatially-dependent detuning. We performed numerical simulations of the resulting thermodynamically stable density distributions, focusing mostly on the M-scheme that has already been realized experimentally. This scheme gives rise to an “Abelian” spin-orbit-coupling with a well-understood ground state that we used

as a basis of our numerical simulations that showed topological excitations above the ground state. We expect that the predicted vortex configurations, in particular vortices appearing in pairs in the spatially-separated left- and right-moving regions, would be straightforward to observe experimentally, as all necessary ingredients are already experimentally available.

2.6 Other works on vortices in spin-orbit-coupled BECs

After this work was completed, we became aware of two papers which also study spin-orbit-coupled BECs under rotation [43,44]. The approach in these papers is qualitatively different from our work, i.e. they simply postulate the Hamiltonian of the system under rotation without derivation and discussion about experimental implications. Also, both papers study the system with Rashba spin-orbit coupling, whereas we concentrated on the type of coupling that had already been realized in experiment.

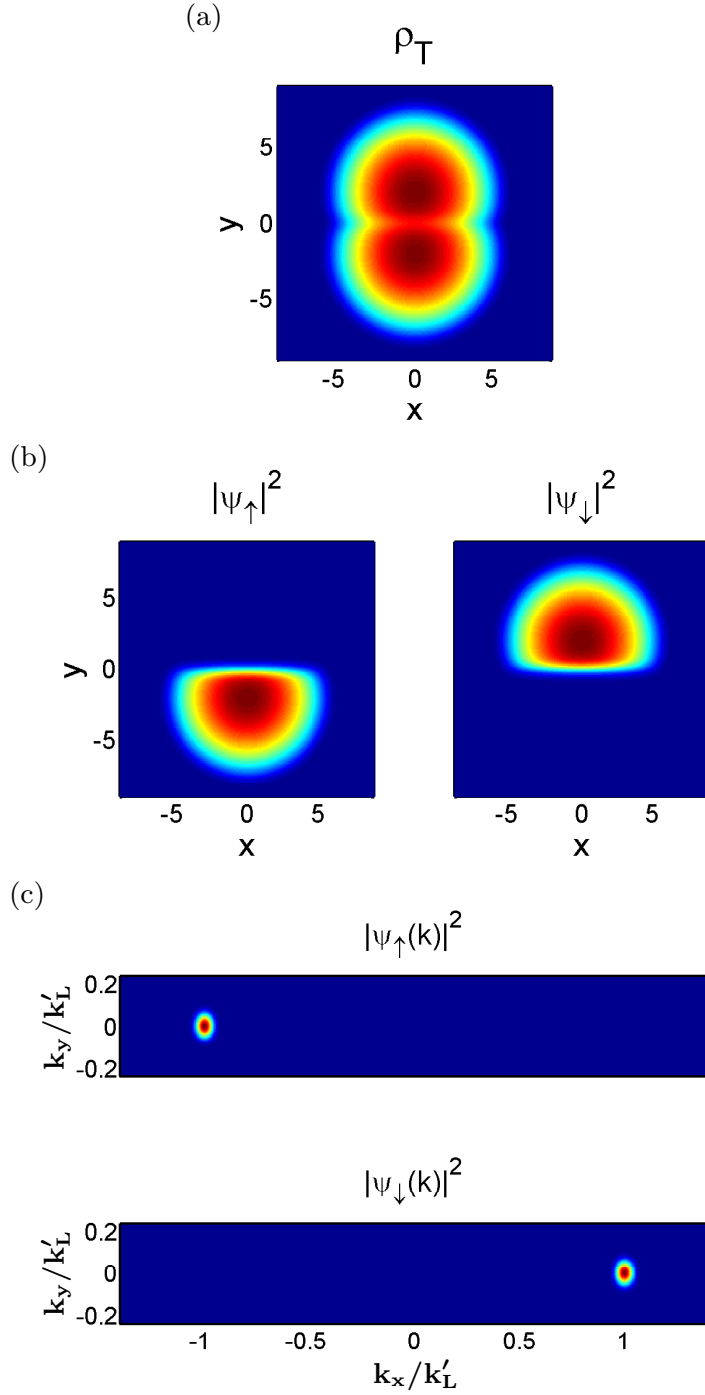


Figure 2.2: The figure shows results for $\Omega = 0$, $\beta = 4 \hbar\omega/a_0$ and $\gamma = 1$. In (a) the total density is shown. The shape of the density is determined by spatially-dependent detuning, which shifts the densities of $|\uparrow\rangle$ and $|\downarrow\rangle$ particles (b). Momentum distribution of $|\uparrow\rangle$ and $|\downarrow\rangle$ components is shown in (c).

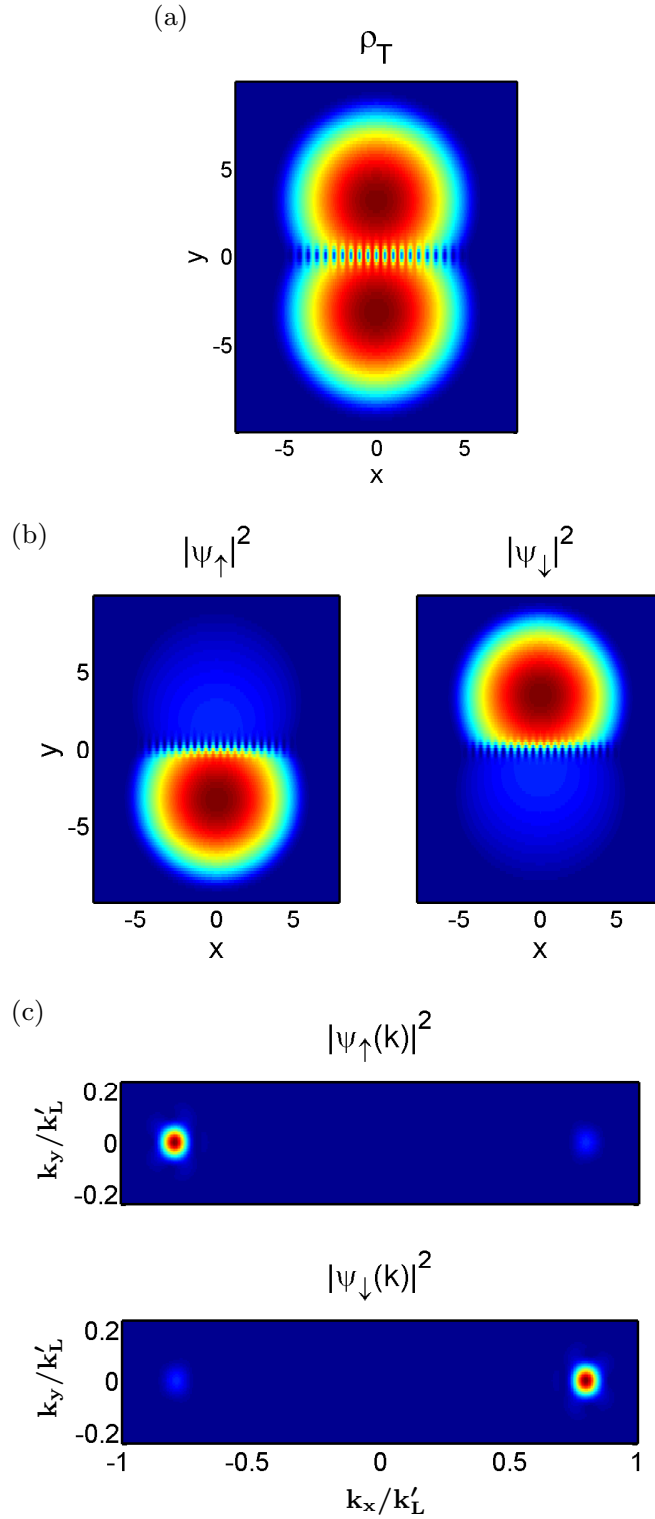


Figure 2.3: The figure shows results for $\Omega = 3 E_L$, $\beta = 8 \hbar\omega/a_0$ and $\gamma = 1$. In (a) the total density is shown. The series of minima at $y = 0$ comes from vortices in $|\uparrow\rangle$ and $|\downarrow\rangle$ wavefunctions (b). Momentum distribution of $|\uparrow\rangle$ and $|\downarrow\rangle$ components is shown in (c).

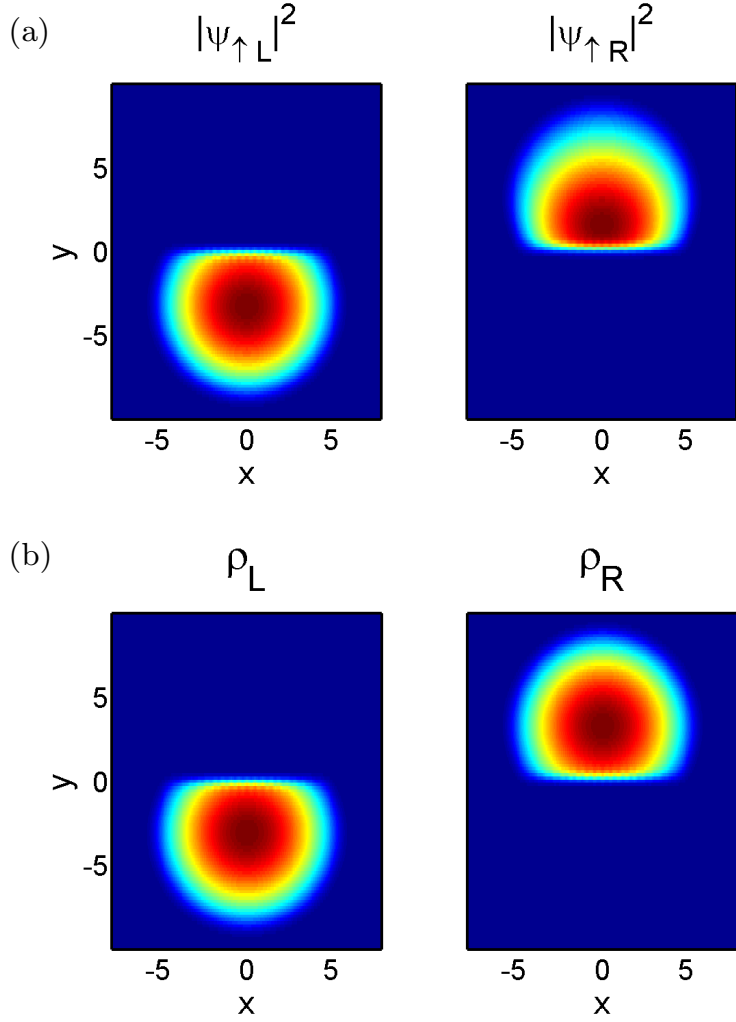


Figure 2.4: The figure (a) shows $|\psi_{\uparrow L}|^2$ and $|\psi_{\uparrow R}|^2$ the relative amplitude of which is given by $\int d^2r |\psi_{\uparrow L}|^2 = 0.45$ and $\int d^2r |\psi_{\uparrow R}|^2 = 0.05$ for the parameters $\Omega = 3 E_L$, $\beta = 8 \hbar\omega/a_0$ and $\gamma = 1$. The superposition of $\psi_{\uparrow L}$ and $\psi_{\uparrow R}$, $\psi_{\uparrow} = \psi_{\uparrow L} + \psi_{\uparrow R}$, produces vortices in ψ_{\uparrow} . The density of left- and right-moving particles ($\rho_L = |\psi_{\uparrow L}|^2 + |\psi_{\downarrow L}|^2$, $\rho_R = |\psi_{\uparrow R}|^2 + |\psi_{\downarrow R}|^2$) particles is shown in (b).

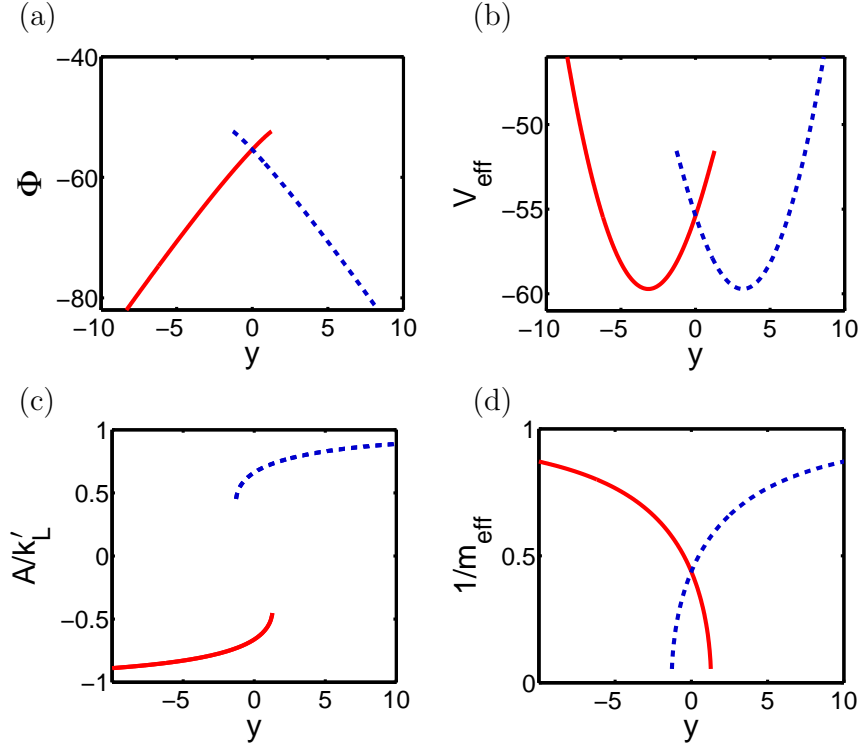


Figure 2.5: The figure shows the scalar potential $\Phi(y)$ (a), the effective trapping potential in \hat{y} direction $V_{\text{eff}}(y)$ (b), vector potential $A(y)$ (c) and inverse of the effective mass (d) for $\Omega = 3 E_L$, $\beta = 8 \hbar\omega/a_0$ and $\gamma = 1$. Values corresponding to the left minimum of the spectrum are represented by a solid red line while the values corresponding to the right minimum of the spectrum are represented by a dashed blue line (see the text for details).

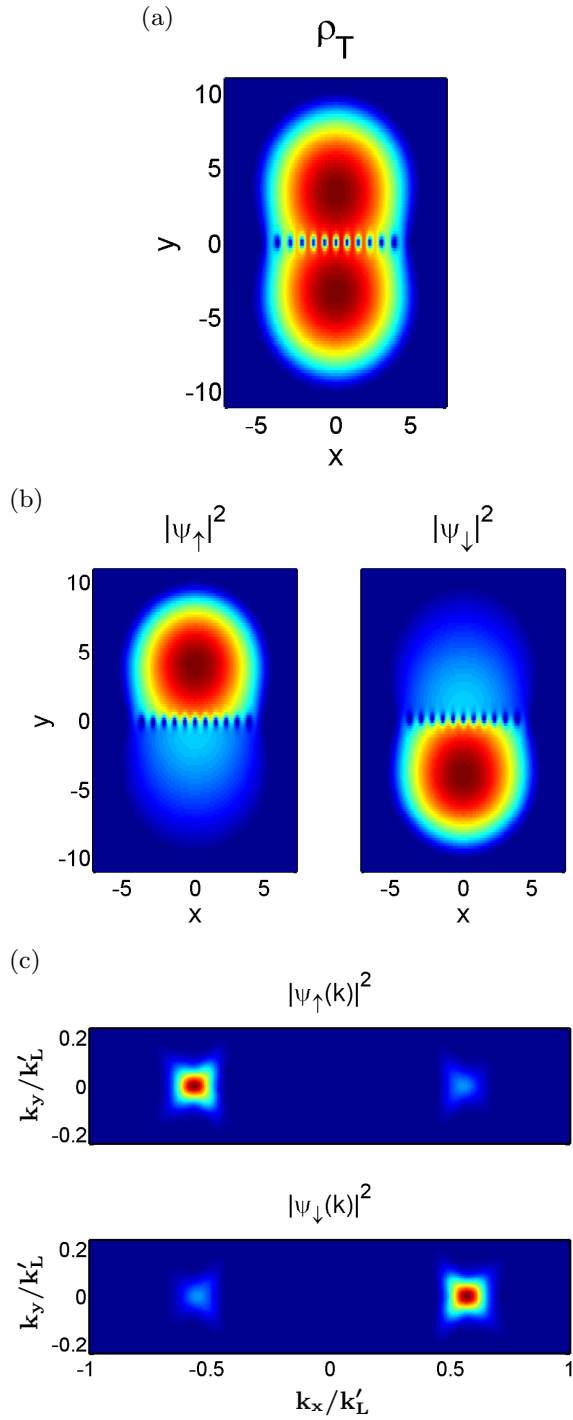


Figure 2.6: The figure shows results for $\Omega = 5 E_L$, $\beta = 12 \hbar\omega/a_0$ and $\gamma = 1$. In (a) the total density is shown. The series of minima at $y = 0$ comes from vortices in $|\uparrow\rangle$ and $|\downarrow\rangle$ wavefunctions (b). Momentum distribution of $|\uparrow\rangle$ and $|\downarrow\rangle$ components is shown in (c).

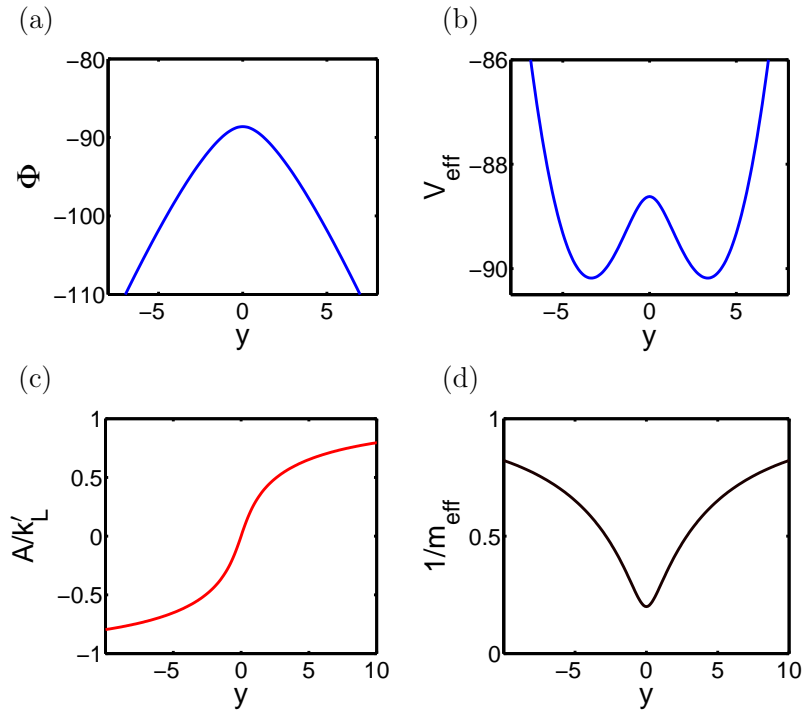


Figure 2.7: The figure shows the scalar potential $\Phi(y)$ (a), the effective trapping potential in \hat{y} direction $V_{\text{eff}}(y)$ (b), vector potential $A(y)$ (c) and inverse of the effective mass (d) for $\Omega = 5 E_L$, $\beta = 12 \hbar\omega/a_0$ and $\gamma = 1$.

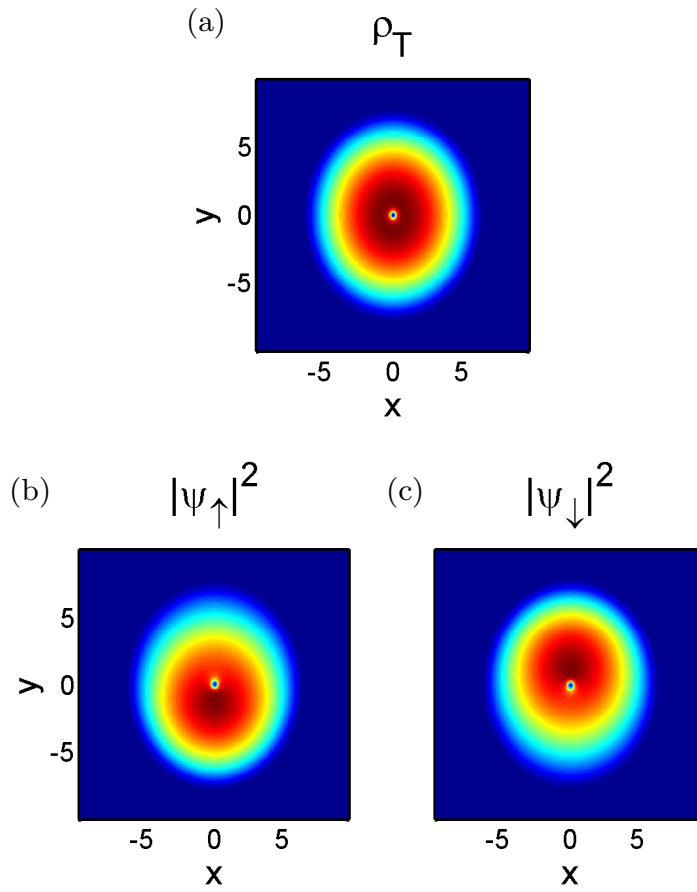


Figure 2.8: The figure shows results for $\Omega = 10 E_L$, $\beta = 12 \hbar\omega/a_0$ and $\gamma = 1$. In (a) the total density is shown, while (b) and (c) show densities of $|\uparrow\rangle$ and $|\downarrow\rangle$ components. The vortex in the center appears for strong enough effective magnetic field.

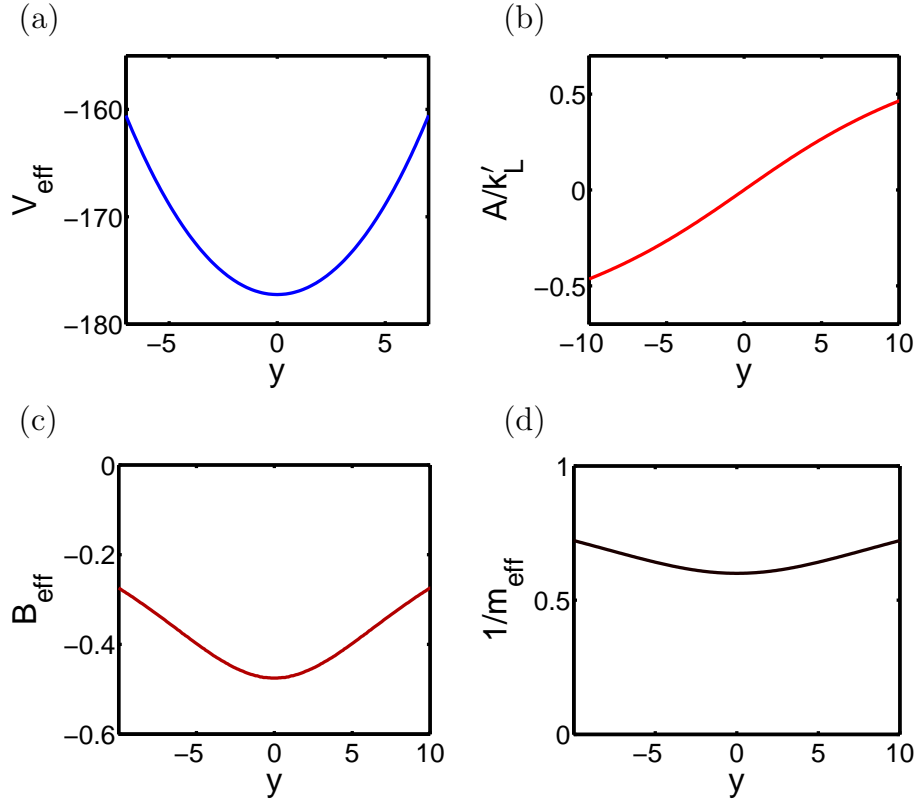


Figure 2.9: The figure shows the effective trapping potential in \hat{y} direction $V_{\text{eff}}(y)$ (a), vector potential $A(y)$ (b), the effective magnetic field B_{eff} (c) and inverse of the effective mass (d) for $\Omega = 10 E_L$, $\beta = 12 \hbar\omega/a_0$ and $\gamma = 1$.

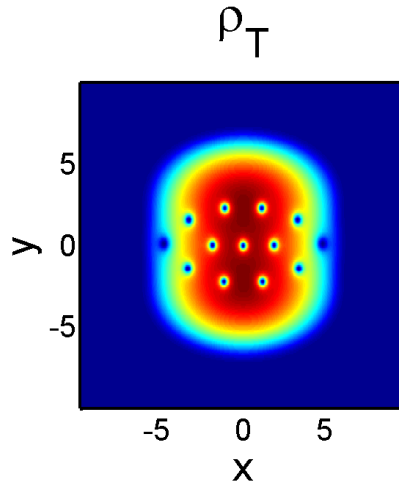


Figure 2.10: The figure shows the total density for $\Omega = 10 E_L$, $\beta = 40 \hbar\omega/a_0$ and $\gamma = 1.85$.

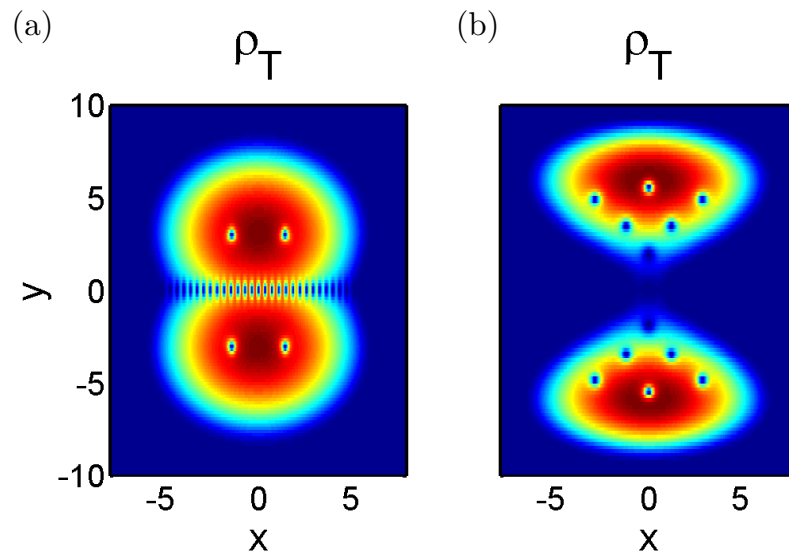


Figure 2.11: Figures show separated left and right phases with vortices in each phase. Trapping frequency is $\omega = 2\pi \times 10$ Hz. Figure (a) shows total density for $\Omega = 4 E_L$, $\beta = 20 \hbar\omega/a_0$ and $\gamma = 1.3$. Figure (b) shows total density for $\Omega = 10 E_L$, $\beta = 150 \hbar\omega/a_0$ and $\gamma = 2.75$.

Chapter 3: Exotic Quantum Spin Models in Spin-Orbit-Coupled Mott Insulators

3.1 Introduction

In the last 20 years, cold atoms have proven to be an excellent playground for studying many-body physics [13,45] and this is especially true for studying strongly correlated systems such as atoms in optical lattices. The prominent example is the observation of superfluid to Mott insulator transition [46] which was followed by experimental and theoretical work on both Bose and Fermi gases in lattices of different dimensionality and in various parameter regimes [13,45]. The key features of cold atoms in optical lattices are an excellent tunability of parameters and the fact that the system is almost perfectly described by the Hubbard model in the deep lattice regime [47]. Since it is well known that the Hubbard model is mapped to an effective spin Hamiltonian for Mott-insulator phases with integer filling, it is clear that cold atoms can be used to “engineer” various quantum spin systems [48,49] from those described by the Heisenberg model to more exotic ones, like the Kitaev model [50]. In designing effective spin systems different tools like polar molecules [51] and tilted optical lattices [52] can also be used.

In this work we combine optical lattice and SOC which, in the deep lattice regime, leads to tight-binding description with non-zero “spin-flip” hopping between neighboring sites [53]. We show that in the Mott-insulator phase with one atom per site the system is described by an interesting effective spin Hamiltonian which is a combination of Heisenberg model, quantum compass model and Dzyaloshinskii-Moriya terms. We note that combination of an optical lattice and SOC has already been considered with a purpose of studying superfluid-insulator transition [54], topological phase transitions [55] and BEC dynamics [56]. In the context of solid-state physics spin models resulting from Mott-insulators with strong SOC were studied in Ref. [57–60].

3.2 The model

We study a two-dimensional system of pseudospin-1/2 atoms on a square optical lattice with synthetic SOC. The single-particle physics is described by the Hamiltonian:

$$H_0 = \left[\frac{\mathbf{p}^2}{2m} + V_x \sin^2(Kx) + V_y \sin^2(Ky) \right] \check{\mathbf{1}} + \alpha \check{\sigma}_x p_x + \beta \check{\sigma}_y p_y, \quad (3.1)$$

where $\mathbf{p} = -i\hbar\nabla$, m is the atomic mass, V_x, V_y the lattice depth in x and y direction, $K = \pi/a$ (a is lattice spacing), $\check{\mathbf{1}}$ the 2×2 unit matrix, $\check{\sigma}_i$ Pauli matrices; α and β characterize the SOC. We are interested in the deep lattice regime of (3.1) where we can restrict the Hilbert space of the system to the states corresponding to the pair of bands with the lowest energy (the two bands touch at $\mathbf{k} = (0, 0)$, $(0, K)$, $(K, 0)$ and (K, K) in the energy spectrum). The system is then well described by

the tight-binding model in which the Hilbert space is spanned by states localized on individual lattice sites (Wannier states [13]) and particles can tunnel to neighboring sites. There are two localized states per site ($|W_{\mathbf{R}}^1\rangle, |W_{\mathbf{R}}^2\rangle$), hence we have two effective particle species. The most general tight-binding description of (3.1) is:

$$H_{\text{T}} = - \sum_{\mathbf{r}ij} \sum_{\gamma=x,y} [a_{\mathbf{r},i}^\dagger T_\gamma^{(i,j)} a_{\mathbf{r}+\boldsymbol{\eta}_\gamma,j} + \text{H.c.}], \quad (3.2)$$

where $a_{\mathbf{r},i}^\dagger$ ($a_{\mathbf{r},i}$) creates (annihilates) a particle in the state $|W_{\mathbf{r}}^i\rangle$, and $T_\gamma^{(i,j)} = -\langle W_{\mathbf{r}}^i | H_0 | W_{\mathbf{r}+\boldsymbol{\eta}_\gamma}^j \rangle$ are the tunneling matrices ($\boldsymbol{\eta}_\gamma = a\hat{\gamma}$). To find the elements of T_γ corresponding to H_0 , we use Peierls substitution and “localized Wannier states (LWS) method”. We write SOC in a gauge-field form: $\mathbf{p}^2/(2m) + \alpha\check{\sigma}_x p_x + \beta\check{\sigma}_y p_y = (\mathbf{p}-\mathbf{A})^2/(2m) + \text{const.}$ with $\mathbf{A} = (-m\alpha\check{\sigma}_x, -m\beta\check{\sigma}_y)$ and may use Peierls substitution to find tunneling matrices

$$T_\gamma = t_\gamma e^{-iaA_\gamma} = t_\gamma e^{i\theta_\gamma \check{\sigma}_\gamma}, \quad \gamma = x, y \quad (3.3)$$

where t_γ are tunneling coefficients in the γ -direction in the absence of SOC, $\theta_x = \pi\alpha'/2$, $\theta_y = \pi\beta'/2$; α' and β' are dimensionless SOC strengths: $\alpha' = 2m\alpha/(\hbar K)$, $\beta' = 2m\beta/(\hbar K)$. However, Peierls substitution is only an approximation, valid for SOC weak with respect to the energy gap between the lowest-energy pair and first excited pair of bands, i.e. for $\alpha', \beta' \ll (\sqrt{V_x/E_R} + \sqrt{V_y/E_R})$, where $E_R = \hbar^2 K^2/(2m)$ is the lattice recoil energy. While SOC is quite weak in solid-state systems, in cold-atom systems it is typically very strong and in that case Peierls substitution is not completely valid. For example, if we combine optical lattice with spacing $a = 410$ nm and Rashba SOC generated by a scheme described in Ref. [28], we obtain $\alpha' \approx 1$ (typical experimental values of lattice depth are $\sqrt{V_{x,y}/E_R} \sim 2-5$).

Since the validity condition for Peierls substitution is not completely satisfied, we find tunneling matrices using LWS method, i.e. by explicitly calculating localized Wannier states corresponding to the lowest-energy pair of bands of H_0 and by projecting H_0 to the Wannier-state basis. Here Wannier states are a linear superposition of both bands and to calculate them we follow the numerical method described in Ref. [61]. The method we used is described in the appendix B. LWS results show that the tunneling matrices still have the form given in (3.3) but now the parameters t_x , t_y , θ_x and θ_y are some more general functions of V_x , V_y , α , β , K and m . It can be shown that the structure of tunneling matrices (3.3) follows from symmetries of H_0 .

Peierls substitution has the advantage to give an analytical form for tunneling matrices, however it does not give any information about the Wannier states, whereas the LWS method explicitly gives states $|W_{\mathbf{r}}^1\rangle$, $|W_{\mathbf{r}}^2\rangle$ which can be important in interpreting the experimental data. In Fig. 3.1 we compare tunneling amplitudes in the Rashba-coupling case obtained by Peierls substitution and LWS method for $V_x = V_y = 10 E_R$. The figure shows excellent accord for small α' and sizable differences for larger ones.

Cold atoms in optical lattices are described by the tunneling Hamiltonian (3.2) plus interactions [13]:

$$V = \frac{1}{2} \sum_{rij} U_{ij} : n_{\mathbf{r},i} n_{\mathbf{r},j} : , \quad (3.4)$$

where $n_{\mathbf{r},i}$ is a number of particles in state $|W_{\mathbf{r}}^i\rangle$, U_{ij} are interaction coefficients and $:(...):$ denotes normal ordering of creation and annihilation operators. Since H_0 is

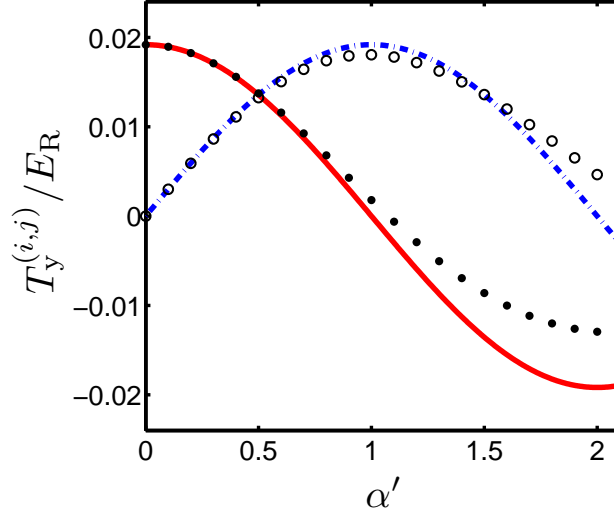


Figure 3.1: Tunneling amplitudes $T_y^{(1,1)}$ and $T_y^{(1,2)}$ obtained by Peierls substitution (full red and dash-dotted blue line) and localized Wannier states method (full dots and empty circles) for different strengths of Rashba SOC and $V_x = V_y = 10 E_R$.

already written in a dressed-state basis [18, 28] and $\{|W_{\mathbf{R}}^i\rangle\}$ are some linear combinations of these dressed states, interaction coefficients U_{ij} are generally some complicated functions of s-wave scattering lengths between atoms in different hyperfine states. While the exact dependence of U_{ij} on the parameters V_x , V_y , α and β differs for various SOC schemes, the overall amplitude of U_{ij} is proportional to $\int d\mathbf{r} |\phi(\mathbf{r})|^4$, $\phi(\mathbf{r})$ being the ground state solution of $H = \mathbf{p}^2/(2m) + V_x K^2 x^2 + V_y K^2 y^2$ [13].

3.3 Low-energy Hamiltonian (spin model)

We are interested in the Mott-insulator regime with $t_x/U_{ij} \ll 1$, $t_y/U_{ij} \ll 1$ and one atom per site. In this case interactions (3.4) are the dominant part of the full Hamiltonian ($H = H_T + V$) and we may treat the problem perturbatively by taking V as a starting Hamiltonian and H_T as a perturbation. The ground state of V is a state with uniform distribution of atoms and the ground state degeneracy is very

large since there are two states per site that atoms can occupy. The perturbation H_T couples the ground-state manifold and excited states of V and the resulting low-energy effective Hamiltonian can be calculated in the second order of perturbation theory [48, 49]:

$$(H_{\text{eff}})_{\alpha\beta} = - \sum_{\gamma} \frac{(H_T)_{\alpha\gamma}(H_T)_{\gamma\beta}}{E_{\gamma} - (E_{\alpha} + E_{\beta})/2}, \quad (3.5)$$

where α and β label states in the ground-state manifold, while γ labels the excited states of V .

We first calculate the effective low-energy Hamiltonian for bosons:

$$H_B = - \sum_{i=x,y} \sum_{\mathbf{r}'-\mathbf{r}=\boldsymbol{\eta}_i} \left[J_{\text{h}}^i \mathbf{S}_{\mathbf{r}} \cdot \mathbf{S}_{\mathbf{r}'} + J_{\text{cm}}^i S_{\mathbf{r}}^i S_{\mathbf{r}'}^i + J_z^i S_{\mathbf{r}}^z S_{\mathbf{r}'}^z + \mathbf{D}_i \cdot (\mathbf{S}_{\mathbf{r}} \times \mathbf{S}_{\mathbf{r}'}) \right] - h \sum_{\mathbf{r}} S_{\mathbf{r}}^z, \quad (3.6)$$

where we introduced isospin operators: $S_{\mathbf{r}}^x = (a_{\mathbf{r},1}^{\dagger} a_{\mathbf{r},2} + a_{\mathbf{r},2}^{\dagger} a_{\mathbf{r},1})/2$, $S_{\mathbf{r}}^y = -i(a_{\mathbf{r},1}^{\dagger} a_{\mathbf{r},2} - a_{\mathbf{r},2}^{\dagger} a_{\mathbf{r},1})/2$ and $S_{\mathbf{r}}^z = (n_{\mathbf{r},1} - n_{\mathbf{r},2})/2$. The parameters are: $J_{\text{h}}^i = J_i \cos(2\theta_i)$, $J_{\text{cm}}^i = 2J_i \sin^2 \theta_i$, $J_z^i = (u_1 + u_2 - 2)J_{\text{h}}^i$, $\mathbf{D}_x = \hat{x}(u_1 + u_2) \sin(2\theta_x)J_x/2$, $\mathbf{D}_y = \hat{y}(u_1 + u_2) \sin(2\theta_y)J_y/2$, $h = (u_1 - u_2)(J_x \cos^2 \theta_x + J_y \cos^2 \theta_y)$. $J_i = 4t_i^2/U$, θ_i were introduced in (3.3) and $u_1 = U_{12}/U_{11}$, $u_2 = U_{12}/U_{22}$. Since the atoms usually used in experiments have almost spin-independent interactions we may assume $U_{ij} = U$ ($u_1 = u_2 = 1$). In that case $J_z^i = h = 0$ and the Hamiltonian is a combination of Heisenberg model, compass model and Dzyaloshinskii-Moriya-type terms; for $\theta_x = \theta_y = 0$ (no SOC) and $J_x = J_y$ we recover the Heisenberg model [48, 49, 62].

Next we find the effective low-energy Hamiltonian for fermions. The only relevant interaction coefficient is U_{12} since the excited states of V are those with two fermions of different species at the same site. The Hamiltonian has the same

form as in (3.6) with the following coefficients: $J_{\mathbf{h}}^i = -J_i \cos(2\theta_i)$, $J_{\text{cm}}^i = -2J_i \sin^2 \theta_i$, $J_z^i = 0$, $\mathbf{D}_x = -J_x \sin(2\theta_x)\hat{x}$, $\mathbf{D}_y = -J_y \sin(2\theta_y)\hat{y}$ and $h = 0$.

3.4 Classical phase diagram at zero temperature

We intend to find the classical zero-temperature phase diagram for bosonic case (3.6) with $u_1 = u_2 = 1$ ($J_z^i = h = 0$) and $J_x = J_y$ for a wide range of SOC parameters θ_x, θ_y ($\theta_x \sim \alpha, \theta_y \sim \beta$). Some previous papers presented models combining Heisenberg, Dzyaloshinskii-Moriya and compass-model interactions [57–59] but they did not provide a complete phase diagram, neither at a classical level, usually considering only small SOC. An extensive study dedicated to the pure compass model can be found in Ref. [63]. In our approach we treat the spins \mathbf{S}_i as classical vectors and we aim to find the configurations $\{\mathbf{S}_i\}$ which minimize the energy H_{B} . These ground state configurations are found using the steepest descent minimization method, starting from arbitrary spin configurations on 60×60 -site lattices. In Fig. 3.2 we show the phases and in Fig. 3.3 the corresponding phase diagram. We obtain two Ising-type phases [ferromagnet (Fig. 3.2a) and stripes (Fig. 3.2e)], coplanar spirals (Fig. 3.2b) and three-dimensional ordered phases with vortices (Fig. 3.2c) or antivortices (Fig. 3.2d). In describing our results, it is helpful to focus on a so called “basic region” given by the triangle $\theta_y \leq \theta_x \leq \pi/2$: the solutions for other parameters can be obtained by simple mappings, e.g. ground-state configurations in $\theta_x \leq \theta_y \leq \pi/2$ region are obtained by simultaneous $\pi/2$ -rotation of spins and sites of ground states in the “basic region”. Upon activating SOC, the ferromag-

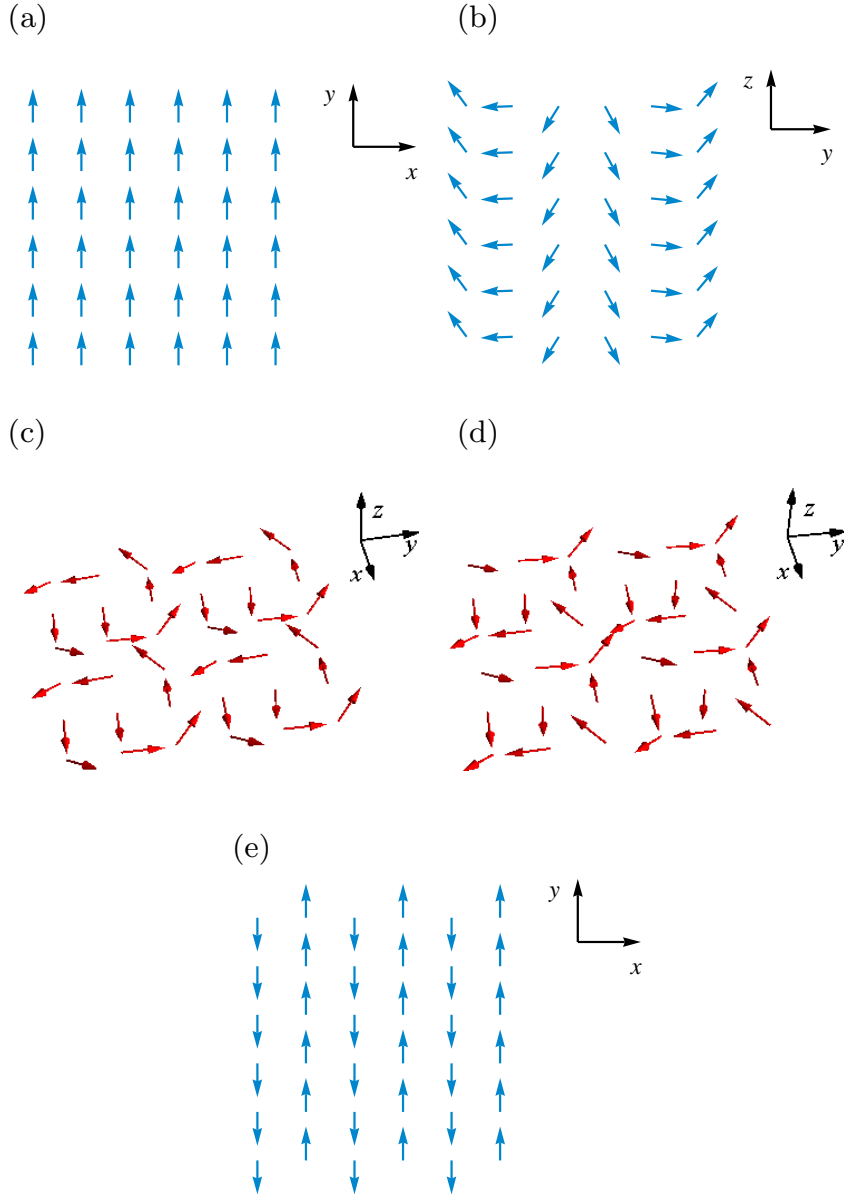


Figure 3.2: Spin textures: (a) ferromagnet ($\theta_x = \theta_y = 0$); (b) spiral wave ($\theta_x = 0.5$, $\theta_y = 0.2$); (c) vortex phase ($\theta_x = \theta_y = 1$); (d) antivortex phase ($\theta_x = \pi - 1$, $\theta_y = 1$); (e) stripes ($\theta_x = 1.6$, $\theta_y = 0.7$). Phases (a), (b) and (e) are coplanar and shown in a two-dimensional representation.

net is immediately replaced by spiral waves, whose spatial periodicity reduces from several to three sites upon increasing θ_x and θ_y ; we found both commensurate and incommensurate waves. When the compass-model term becomes dominant over the Dzyaloshinskii-Moriya one, another coplanar phase appears, the ferromagnetic stripe order, either directly or via the three-dimensional ordered phases. We always find non degenerate classical ground states, except along the dashed lines (Fig. 3.3) which indicate points in the parameter space with a continuous degeneracy of classical ground states. However, we expect this degeneracy to be removed by slight deviations of the realistic engineered SOC with respect to the Rashba-Dresselhaus form of the coupling [28]. The dashed lines also represent the boundaries between phases with stripes of different orientation, *i.e.* between the phase shown in Fig. 3.2e and the one obtained by rotating the sites and spins of the latter by $\pi/2$ around the z -axis. The vortex phase (Fig. 3.2c) takes place along the diagonal $\theta_x = \theta_y$: vortices are left-handed in the region with smaller SOC and right-handed in the one with larger SOC. The antivortex phase (Fig. 3.2d) is found along the diagonal $\theta_y = \pi - \theta_x$ and the configuration (d) is obtained from the phase (c) by a transformation which reflects sites (but not spins) with respect to the x -axis. For a better identification of the phase properties, we consider their behavior with respect to the breaking of the translational symmetry of (3.6). While all the phases (except the ferromagnet) break this symmetry, they do it in a different way, *i.e.* the stripe phase in Fig. 3.2e is not invariant under one-lattice-site translation along x -direction, but it is invariant under two-lattice-sites translations in x -direction and under one-lattice-site translation in y -direction; the phases with vortices or antivortices are not invariant under

one- and two-lattice-sites translations in x and y -direction, but they are invariant under three-lattice-sites translations. Then we can understand the evolution from stripe to vortex phase as a transition in which two-lattice-sites translational symmetry becomes broken. The same reasoning applies for the rest of the phase diagram.

We note that in the fermionic case, the classical version of the effective Hamiltonian is related to the classical bosonic Hamiltonian with $u_1 = u_2 = 1$ by a simple “checkerboard” mapping: flipping spins on sites with $i + j$ being an even integer (i and j are lattice site indices in x and y direction). Therefore, the phase diagram in the fermionic case with $J_x = J_y$ has the same structure as the phase diagram in Fig. 3.3 and fermionic ground state configurations are related to configurations in Fig. 3.2 by the checkerboard mapping.

3.5 Experimental realization

Experimental realization of the system we consider is as follows: a 2D optical lattice in x-y plane and a very deep lattice along z-direction which confines atoms to the x-y plane are accompanied by a laser setup for creating SOC described in Ref. [28]. In this SOC setup parameters α and β are of limited variability ($\alpha \approx \beta \approx \hbar k_L / (2m)$, where k_L is “SOC-laser” wave vector), however we may choose different values of lattice wave vectors in x and y direction (K_x, K_y) and this enables us to access a wide parameter regime: $\theta_x, \theta_y \gtrsim \pi/2$ [$\theta_j \approx (k_L / K_j)(\pi/2)$ and $K_j \lesssim k_L$]. Since the Hamiltonian H_B with $u_1 = u_2 = 1$ is periodic with respect to θ_x, θ_y with

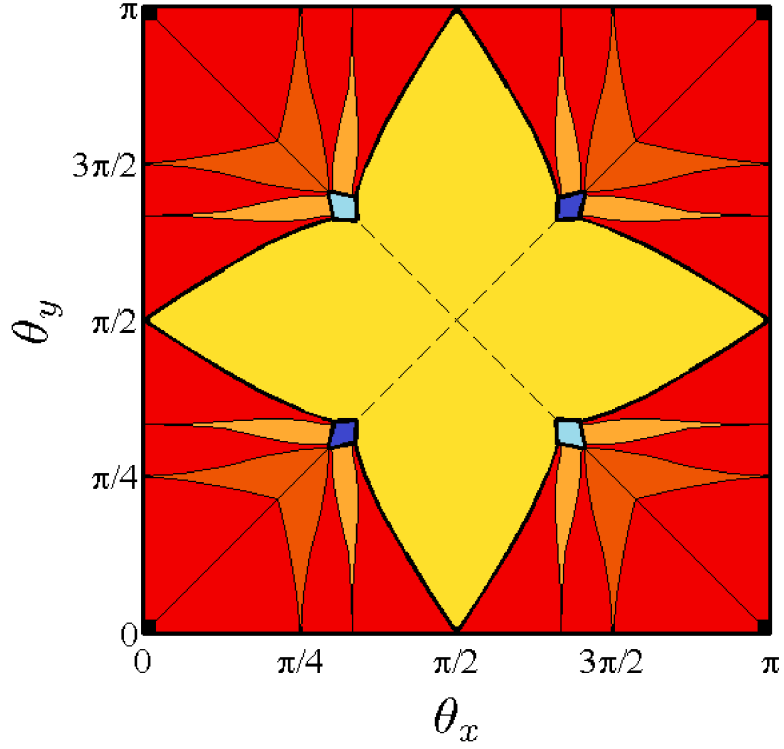


Figure 3.3: Classical phase diagram of the Hamiltonian H_B (see text for details): ferromagnet (black corner dots); spiral waves [dark orange (commensurate with four-sites periodicity), light orange (commensurate with three-sites periodicity), red (others)]; stripes (yellow); vortex phase (dark blue) and antivortex phase (light blue). Dashed lines denote the part of the stripe region with continuous ground-state degeneracy and also separate stripe phases of different orientation. Straight black lines separate phases of different orientation inside the spiral region.

period π , it is in principle possible to experimentally access the whole region of the phase diagram shown in Fig. 3.3.

Several methods for detecting spin textures in Mott-insulator phase have been proposed: for example, noise correlations in time-of flight (TOF) images [64] and optical Bragg scattering [65] provide spin-spin correlations $\langle \mathbf{S}_r \cdot \mathbf{S}_{r'} \rangle$ by measuring spin structure factors; signatures of magnetic order can also be observed by combining TOF imaging and Feshbach resonance during expansion [66]. We note that in the SOC case Wannier states are generally composed of both pseudospin $|\uparrow\rangle$ and $|\downarrow\rangle$ components while pseudospin states themselves are some linear combinations of atomic hyperfine states [28]. These features have to be taken into account when interpreting experimental data.

The energy scale of the effective Hamiltonian is of order t^2/U which is very small with respect to typical sample temperatures, having in mind the requirement $t \ll U$. Unfortunately, current state of art experiments are still not able to reach low-enough temperatures/entropies, in order to be able to observe spin textures, even in lattices without SOC (see for example [67]) and thus only paramagnetic Mott insulators are prepared in experiments. However, new methods of cooling and reducing the entropy per particle are being developed [68]. In particular, a recent experiment on ultracold fermions in a cubic optical lattice managed to measure anti-ferromagnetic correlations [69] gives us hope that our theoretical findings could be tested experimentally in the near future.

3.6 Conclusion

In summary, we studied the effects of spin-orbit coupling in cold atoms in an optical lattice in the Mott-insulating regime. We derived the tight-binding model using Peierls substitution and localized Wannier State method, and obtained the effective low-energy Hamiltonian for bosons and fermions: this takes the form of an exotic spin model with Heisenberg, compass-model and Dzyaloshinskii-Moriya interactions. We determined the classical phase diagram for this model and showed that the interplay between the different interactions is responsible for a large variety of phases: ferromagnet, spirals, stripes, three-dimensional vortex and antivortex phases. We expect that our classification of ground states could generally survive in a quantum approach; in fact, except for some particular cases we mentioned in the discussion, on the classical level there are no degeneracies which would be lifted by quantum fluctuations. Due to current experimental state of the art, our theoretical investigation is aimed more to provide predictions for future experiments than to explain present evidence.

We would like to note that, after submitting this work to a journal, several other papers appeared which studied magnetic phases [70, 71] and superfluid-insulator transition for bosons in optical lattices with synthetic SOC [70, 72].

Chapter 4: Interaction-Tuned Dynamical Transitions in a Rashba Spin-Orbit Coupled Fermi Gas

4.1 Introduction

One of the important contributions of cold atoms has been the ability to study non-equilibrium phenomena of closed many-body quantum systems [73]. Cold-atom systems are very well isolated from the environment and they are highly controllable which, among other things, enables studying dynamics after a quench, or of a periodically driven system. Finally there are numerous ways to probe the system, e.g. time-of-flight imaging, “quantum gas microscope” imaging [74], Bragg spectroscopy [75], etc. Therefore, there have been many experiments which provided access not only to thermodynamic quantities, but have also yielded insights into how correlations develop and spread across a system following a parameter quench, how long-range order is established, and the mechanisms underlying thermalization in isolated interacting systems [13, 73, 76–78].

In this chapter we study spin dynamics occurring in a weakly interacting, uniform spin-orbit coupled Fermi gas, which is initially spin polarized. We assume that the momentum distribution in the initial state is the classical Maxwell distribu-

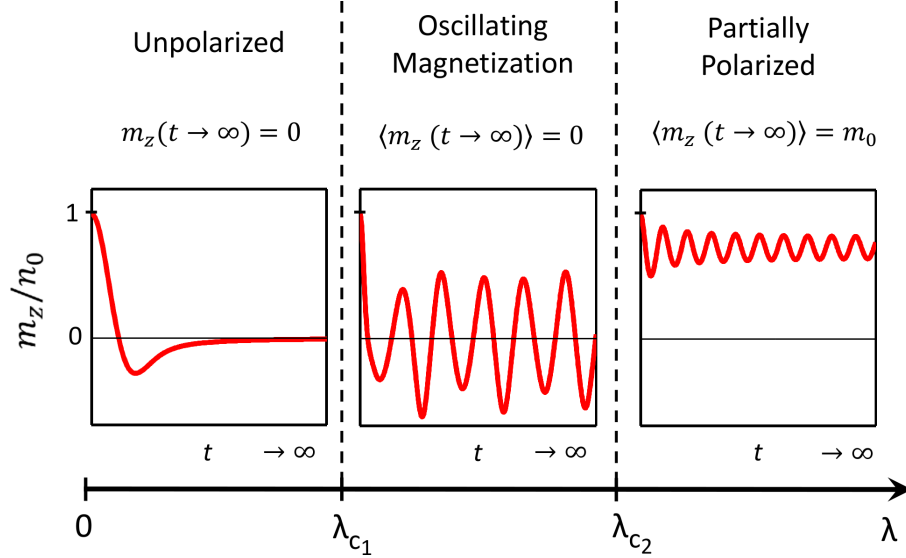


Figure 4.1: Schematic plot showing non-equilibrium steady states of an initially spin-polarized Fermi gas in the presence of SOC. Here $\lambda = gn_0/\alpha p_{\text{th}}$, where gn_0 parametrizes the interactions (Eq. 4.2) and αp_{th} parametrizes the SOC (Eq. 4.3). Different types of steady states are separated by transition points λ_{c1} and λ_{c2} . For small interactions ($\lambda < \lambda_{c1}$), magnetization decays to zero. For $\lambda_{c1} < \lambda < \lambda_{c2}$ magnetization oscillates forever around zero, while for large interactions ($\lambda > \lambda_{c2}$) the system becomes partially polarized.

tion. Interplay between classical motion in the thermal gas, quantum spin degrees of freedom subject to spin-orbit coupling and interactions gives rise to interesting dynamical regimes, which are the focus of this work. Our main results are summarized in Fig. 1: we find that there are three possible distinct steady states which can be labelled as: unpolarized state, oscillating magnetization state, and partially polarized state. Different steady states correspond to different values of the ratio of the interaction strength to the SOC strength (denoted as λ), and we find clear transitions between different regimes as we change λ .

For weak interactions, the system can be treated within the Hartree-Fock (“collisionless”) approximation (see [79]), which as shown below, leads to the Boltzmann

equation:

$$\frac{\partial \hat{f}}{\partial t} = \frac{i}{\hbar} \left[\hat{f}, \alpha (p_x \hat{\sigma}_x + p_y \hat{\sigma}_y) - \frac{1}{2} g \mathbf{M} \cdot \hat{\boldsymbol{\sigma}} \right], \quad (4.1)$$

where $\hat{f}(\mathbf{p}, t)$ is the Wigner distribution, $\hat{\sigma}_i$ are Pauli matrices, $\mathbf{M} = \{m_x, m_y, m_z\}$ is the density-dependent magnetization, \mathbf{p} is momentum, and α and g denote the SOC and interaction strength respectively (details and the derivation are discussed later in the text). This equation describes spin-precession for a particle with momentum \mathbf{p} in an effective magnetic field, $\mathbf{B}_{\text{eff}} = (\alpha p_x - gm_x/2, \alpha p_y - gm_y/2, -gm_z/2)$, which involves a combination of SOC and interactions. The fully polarized initial state points along the z (longitudinal) direction.

If $g = 0$, \mathbf{B}_{eff} points in the x-y (transverse) plane; spins of particles with different momenta precess at different frequencies causing dephasing, and the total magnetization decays to zero at long times. For very large g , for a fully polarized initial state, the effective field points close to the z -axis (Fig. 2). As a result the total magnetization does not decay to zero, but approaches a finite value at long times. When SOC and interactions are of comparable strength, the dynamics leads to a steady state where the magnetization shows undamped oscillations about a zero mean-value. This unusual state is a result of the strongly non-linear character of Eq. (4.1).

In a solid-state material, spin dynamics is primarily influenced by spin-orbit coupling and scattering from impurities and phonons [80–82]. Collisions lead to random changes in the electron’s momentum, which in turn causes the spin to precess in random directions, leading to Dyakonov-Perel spin relaxation [80] and

diffusive dynamics of magnetization [83].

In an ultra-cold gas, the situation is different: there is no disorder, and the inter-particle interactions are typically important. In most of the experiments so far, these interactions take the form of a density-density, s-wave contact interaction between two different hyperfine states of a fermionic atom (typically ${}^6\text{Li}$ or ${}^{40}\text{K}$):

$$\check{V}_{\text{int}} = g \int d\mathbf{r} \check{n}_{\uparrow}(\mathbf{r}) \check{n}_{\downarrow}(\mathbf{r}), \quad (4.2)$$

where the two hyperfine states are denoted using pseudo-spin variables $\{\uparrow, \downarrow\}$, the interaction parameter g is proportional to the s-wave scattering length a (it can be tuned using Feshbach resonances [84]), and $\check{n}_{\uparrow(\downarrow)}(\mathbf{r})$ is the spin-density operator. S-wave interactions between like fermions are forbidden by the Pauli exclusion principle.

Depending on the strength of the inter-particle interactions, the gas can be described as either *collisionless* (Knudsen) or *collision dominated* [79]. The former limit, which is the focus of this work, is achieved when the interactions are so weak, that the timescale for mean-field spin exchange, given by $t_{\text{mf}} \sim m/\hbar a n_0$, is much shorter than the typical collision time $t_{\text{coll}} \sim 1/(n_0 \bar{v} \sigma)$. Here n_0 is the density, m is the mass, \bar{v} is the average velocity of the particles, and $\sigma = 4\pi a^2$ is the scattering cross-section. For typical experimental densities, and temperatures $T \sim T_F$, the collisionless regime corresponds to scattering lengths $a \sim 10a_B$, which yields a $t_{\text{coll}} \sim 1\text{s}$ and a mean-field time $t_{\text{mf}} \sim 50\text{ms}$. Hence the collisionless limit can be readily explored in experiments [85].

4.2 The model

In this chapter we consider a spin-1/2 Fermi gas with Rashba spin-orbit coupling:

$$\hat{H}_0 = \frac{\mathbf{p}^2}{2m} + U(\mathbf{r}) + \alpha (p_x \hat{\sigma}_x + p_y \hat{\sigma}_y), \quad (4.3)$$

where $\mathbf{p} = -i\hbar\nabla$ and $U(\mathbf{r})$ is the external potential. This single-particle Hamiltonian can lead to novel spin textures and spin dynamics, even in the absence of interactions [18, 31, 32, 86, 87]. To study the dynamics of the system, we derive the collisionless Boltzmann equation which describes the evolution of the Wigner distribution:

$$f_{ij}(\mathbf{r}, \mathbf{p}, t) = \int d\mathbf{R} e^{i\mathbf{p}\cdot\mathbf{R}/\hbar} \left\langle \check{\psi}_i^\dagger \left(\mathbf{r} - \frac{\mathbf{R}}{2}, t \right) \check{\psi}_j \left(\mathbf{r} + \frac{\mathbf{R}}{2}, t \right) \right\rangle, \quad (4.4)$$

which contains all the information about single-particle observables ($i, j \in (\uparrow, \downarrow)$). For example, total density is $n(\mathbf{r}) = n_\uparrow(\mathbf{r}) + n_\downarrow(\mathbf{r}) = \int d\mathbf{p}/(2\pi\hbar)^d (f_{\uparrow\uparrow} + f_{\downarrow\downarrow})$, where d is dimensionality of the system.

For spin-orbit-coupled fermions with contact interactions the collisionless Boltzmann equation reads [79, 87, 88]:

$$\begin{aligned} \frac{\partial \hat{f}}{\partial t} + \frac{\mathbf{p}}{m} \cdot \nabla_{\mathbf{r}} \hat{f} - \frac{i}{\hbar} \left[\hat{f}, \alpha (p_x \hat{\sigma}_x + p_y \hat{\sigma}_y) + \hat{V} \right] \\ - \frac{1}{2} \{ \nabla_{\mathbf{p}} \hat{f}, \nabla_{\mathbf{r}} \hat{V} \} + \frac{1}{2} \alpha \{ \partial_x \hat{f}, \hat{\sigma}_x \} + \frac{1}{2} \alpha \{ \partial_y \hat{f}, \hat{\sigma}_y \} = 0, \end{aligned} \quad (4.5)$$

where:

$$\hat{f}(\mathbf{r}, \mathbf{p}, t) = \begin{pmatrix} f_{\uparrow\uparrow}(\mathbf{r}, \mathbf{p}, t) & f_{\downarrow\uparrow}(\mathbf{r}, \mathbf{p}, t) \\ f_{\uparrow\downarrow}(\mathbf{r}, \mathbf{p}, t) & f_{\downarrow\downarrow}(\mathbf{r}, \mathbf{p}, t) \end{pmatrix}, \quad (4.6)$$

and \hat{V} contains effects of an external potential $U(\mathbf{r}, t)$ and interactions:

$$\hat{V}(\mathbf{r}, t) = \begin{pmatrix} U(\mathbf{r}, t) + gn_{\downarrow}(\mathbf{r}, t) & -gn_{-}(\mathbf{r}, t) \\ -gn_{+}(\mathbf{r}, t) & U(\mathbf{r}, t) + gn_{\uparrow}(\mathbf{r}, t) \end{pmatrix}, \quad (4.7)$$

where $n_{\uparrow} = \int d\mathbf{p}/(2\pi\hbar)^d f_{\uparrow\uparrow}$, $n_{\downarrow} = \int d\mathbf{p}/(2\pi\hbar)^d f_{\downarrow\downarrow}$, $n_{+} = \int d\mathbf{p}/(2\pi\hbar)^d f_{\uparrow\downarrow}$ and $n_{-} = n_{+}^*$. The diagonal terms in Eq. 4.7 represent the direct (Hartree) contribution to the interactions, while the off-diagonal terms represent spin exchange. Derivation of Eq.(4.5) is given in Appendix C. We define a magnetization vector $\mathbf{M} = \{m_x, m_y, m_z\} = \{n_{+} + n_{-}, -i(n_{+} - n_{-}), n_{\uparrow} - n_{\downarrow}\}$, which can be readily probed in ultra-cold atom experiments via spin-sensitive phase contrast imaging [89]. We refer to m_z and $\{m_x, m_y\}$ as the longitudinal and transverse magnetization respectively.

In this work we consider a uniform system ($U(\mathbf{r}, t) = 0$), where all the relevant quantities become independent of space (the spatial derivative terms in Eq. (4.5) vanish) and the Boltzmann equation reduces to (4.1), where we have conveniently expressed $\hat{V}(t)$ as: $\hat{V}(t) = -g\mathbf{M}(t) \cdot \hat{\boldsymbol{\sigma}}/2$. The effects of a spatially varying potential $U(\mathbf{r})$ will be discussed later. Spin-orbit coupling can be viewed as a *momentum-dependent* transverse magnetic field \mathbf{B}_{SOC} , as shown in Fig. 4.2. Similarly, the interactions \hat{V} , can be viewed as a *time-dependent* magnetic field $\mathbf{B}_{\text{MF}}(t) = -g\mathbf{M}(t)/2$ where the time dependence of \mathbf{M} arises from the density. Introducing dimensionless units of momentum $\mathbf{p}' = \mathbf{p}/p_{\text{th}}$ ($p_{\text{th}} = \sqrt{2mk_B T}$) and time $\tau = t/t_{\text{soc}}$ ($t_{\text{soc}} = \hbar/\alpha p_{\text{th}}$) in Eq. (4.1), the only parameter in the equation is the ratio of the interaction and SOC strength $\lambda = gn_0/\alpha p_{\text{th}}$. Throughout we refer to weak, intermediate and strong interactions as $\lambda \ll 1$, $\lambda \sim 1$ and $\lambda \gg 1$ respectively. All these regimes can be readily accessed within the collisionless limit by decreasing the SOC strength, which can

be tuned experimentally.

4.3 Results and discussion

Our initial state is a non-degenerate, fully polarized gas of spin- \uparrow fermions in thermal equilibrium, at a temperature T . We require the temperature to be small enough so that the system can be regarded as a two-level system. In the experiment of Wang *et al.* [21], the hyperfine splitting between the states is of order $10 T_F$, so this requirement is readily met. The Wigner function reads $f_{\uparrow\uparrow}(\mathbf{p}, t = 0) = \mathcal{N} \exp[-\beta \mathbf{p}^2 / (2m)]$, $f_{\uparrow\downarrow}(t = 0) = f_{\downarrow\uparrow}(t = 0) = f_{\downarrow\downarrow}(t = 0) = 0$, where \mathcal{N} is an overall normalization factor proportional to the total number of particles and $\beta = 1/k_B T$.

As identical spins do not interact, this initial state is stationary in the absence of spin-orbit coupling. We then suddenly switch on the spin-orbit coupling, and numerically integrate Eq. (4.1) on a two-dimensional 200×200 grid in momentum space using the fourth-order Runge-Kutta method. The interaction matrix \hat{V} is sequentially updated at each timestep, and the step size is small enough so that particle number is conserved to very high accuracy. All our calculations are done for a two-dimensional system, however the results readily generalize to 3D, as the Maxwell-Boltzmann distribution is separable in phase space.

In the absence of interactions ($\lambda = 0$), the Boltzmann equation (4.1) reduces to a linear equation, which can be solved *analytically*. The longitudinal magnetization is then $m_z(\tau) = n_0[1 - \sqrt{\pi}\tau e^{-\tau^2} \text{Erfi}(\tau)]$, where Erfi is the imaginary error function, while $m_x(\tau) = m_y(\tau) = 0$. At short times ($\tau \ll 1$), $m_z \sim n_0(1 - 2\tau^2 + \mathcal{O}(\tau^4))$, while

at long times, m_z vanishes to zero as $m_z(\tau \rightarrow \infty) \rightarrow -n_0/(2\tau^2)$.

The Rashba term in Eq. (4.1) couples the spin- \uparrow and \downarrow states by acting as a transverse magnetic field. An atom initially aligned along \uparrow will therefore perform Rabi oscillations about the Bloch sphere. Atoms with different momenta Rabi oscillate at different frequencies, and over time, the total longitudinal magnetization decays to zero.

The rapid decay of the total magnetization is a property of the thermal gas. At $T = 0$, the dominant momenta participating in the dynamics are centered around the Fermi momentum p_F , which produces magnetization oscillations, in addition to a decay. In the 2D case: $m_z(\tau') = n_0 \left[\sin(2\tau')/\tau' - \sin^2(\tau')/\tau'^2 \right]$, where $\tau' = t\hbar/\alpha p_F$. The slower decay of the magnetization ($\sim 1/\tau'$) at zero temperature, compared to the non-degenerate gas is due to the larger spread of momenta participating in the dynamics in the thermal case.

The amount by which the magnetization decays depends on the choice of initial state. For example, for a initial Wigner distribution of the form $\hat{f}(\mathbf{p}, t = 0) = \mathcal{N}/2 \exp[-\beta \mathbf{p}^2/(2m)] \hat{\sigma}_x$, the average magnetization m_x decays to *half* its original value, rather than to zero.

The situation becomes much more interesting in the presence of interactions, as the Boltzmann equation now becomes a non-linear equation, which has to be solved self-consistently. In Fig. 4.2, we plot the effect of interactions on the evolution of the total magnetization (we consider only $g > 0$). To understand this dynamics, first note that since $n_+ = n_- = 0$ in the initial state, the dynamics does not generate any transverse components of \mathbf{M} at subsequent times. Exchange interactions therefore

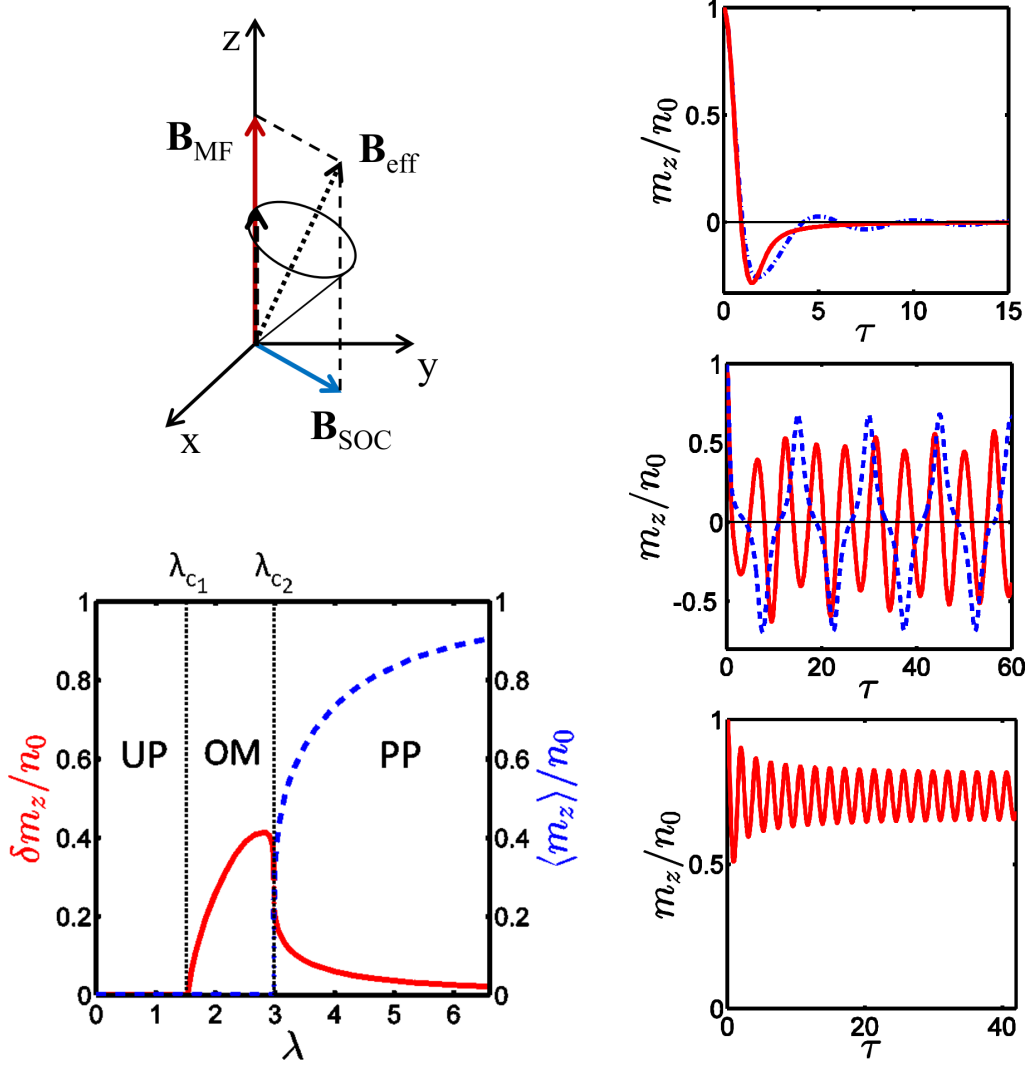


Figure 4.2: Top-Left: SOC and interactions can be viewed as magnetic fields in the longitudinal (red solid arrow) and transverse direction (blue solid arrow) respectively. The spin precesses around $\mathbf{B}_{\text{eff}} = \mathbf{B}_{\text{SOC}} + \mathbf{B}_{\text{MF}}$. Right Panels: Snapshots of the magnetization for various interaction strengths showing the three different final states: unpolarized, oscillating magnetization and partially polarized state. (Top) Solid red curve is the non-interacting result (see text for analytic formula), and the blue dashed-dotted blue curve has $\lambda = 1.5$. (Center) $\lambda = 2.3$ and the strongly anharmonic curve is $\lambda = 2.977$. (Bottom) $\lambda = 4$. Bottom-Left: The long time-averaged magnetization (dashed blue) and the amplitude of fluctuations about the average $\delta m_z = \sqrt{\langle (m_z - \langle m_z \rangle)^2 \rangle}$ (solid red), for different values of λ . At a first critical value, $\lambda_{c1} = 1.533(3)$, the magnetization develops undamped oscillations about zero, and at a second critical value $\lambda_{c2} = 2.9825(2)$, the net magnetization jumps to a non-zero at long times (vertical blue dotted line).

do not play an important role in the dynamics described here. The interaction term can simply be expressed as a time-dependent Zeeman field: $\hat{V} = \mathbf{B}_{\text{MF}}(t) \cdot \hat{\boldsymbol{\sigma}} = -gm_z(t) \hat{\sigma}_z/2$.

For small λ , the dynamics is analogous to the non-interacting case. Spin-orbit coupling leads to spin dephasing on a timescale $t_{\text{soc}} \ll t_{\text{mf}}$, and the longitudinal magnetization m_z (and \mathbf{B}_{MF}) decays to zero. As a result the system becomes effectively non-interacting at long times.

The steady-state magnetization remains zero until the ratio reaches a critical value $\lambda_{c1} = 1.533(3)$. For larger λ , the magnetization is still zero on average, but displays large undamped oscillations. As the interactions are increased (equivalently, as the SOC is decreased), the oscillations become strongly anharmonic, and the amplitude and period of the oscillations grows. Beyond a second critical value $\lambda_{c2} = 2.9825(2)$, the average magnetization approaches a finite value at long times (indicated by the blue dotted line). In the vicinity of λ_{c2} , the oscillation period becomes so long that we are not able to resolve whether the observed jump in the magnetization is merely an artifact of a finite time simulation. As $\lambda \rightarrow \infty$, the average magnetization approaches unity, and the amplitude of the oscillations about the average value, monotonically decreases to zero.

The non-trivial spin dynamics we find is analogous to self-trapping in a double well Bose condensate, which has been well studied experimentally and theoretically [90–92]. If the difference between the on-site interaction energy in each well is small compared to the tunnel splitting, atoms initially prepared in one well undergo sinusoidal Rabi oscillations between the two wells. For stronger interactions there

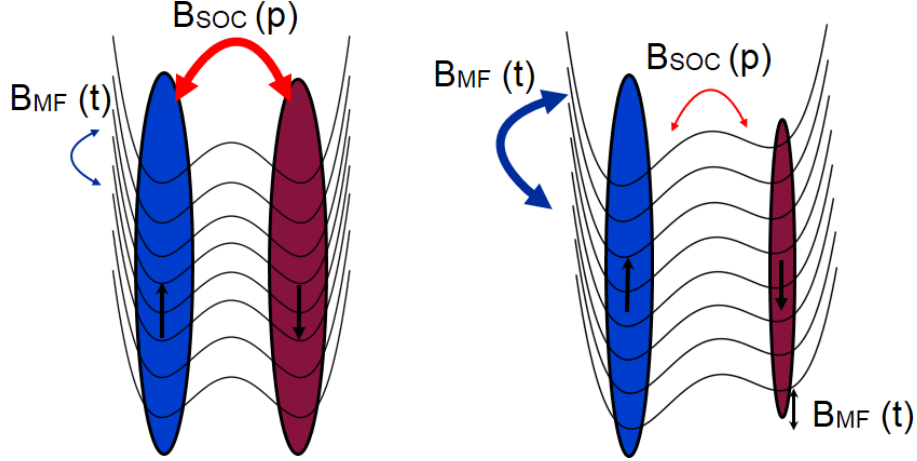


Figure 4.3: Our spin system as a collection of double wells, corresponding to spin- \uparrow (blue oval, left well) and spin- \downarrow (red oval, right well) at each momentum. The intra-well tunnelling is provided by the spin-orbit magnetic field $B_{\text{SOC}}(\mathbf{p})$ (red arrow), which is momentum dependent, while the different wells are coupled to one another via the interaction term $B_{\text{MF}}(t)$ (blue arrow). Arrow thickness denotes the relative strength of interactions and SOC. (Left): Weak interactions ($B_{\text{MF}} \ll B_{\text{SOC}}$), (Right) Strong interactions ($B_{\text{MF}} \gg B_{\text{SOC}}$). See the text for details.

is a transition to a “self-trapped” configuration, where the atoms prefer to remain in one of the two wells.

As shown in Fig. 4.3, our system can be viewed as a collection of “double wells” (corresponding to the spin- \uparrow and spin- \downarrow states) indexed by their momentum \mathbf{p} . Spin-orbit coupling plays the role of the intra-well tunneling, while the role of the on-site interaction energy difference is played by the mean-field term $B_{\text{MF}} = -gm_z(t)/2$. Furthermore, as the mean-field term depends on the spin density, it provides the coupling between the double wells, and can thus lead to collective dynamics.

For weak interactions ($\lambda \ll 1$), (left panel in Fig. 4.3) the double wells are more or less independent of one another, and spins perform Rabi oscillations between \uparrow and \downarrow states with a frequency proportional to their momentum. This leads to a net cancellation of the total magnetization. For stronger interactions, the inter-

well interaction dominates, and spins behave collectively. This leads to coherent, undamped magnetization oscillations. As the interaction strength is increased, the oscillations become anharmonic, as in the double well case [92]. For even stronger interactions ($\lambda \gg 1$) (right panel), the initial on-site energy difference between the left and right wells becomes so much larger than the spin-orbit energy, that atoms prefer to remain in one spin state. This results in a non-zero net magnetization on long times, analogous to the self-trapped configuration in the double-well Bose condensate. We remark that the similarity between our system and the double-well BEC is purely qualitative and the precise equations obeyed by the two systems are different.

We now discuss the additional physics introduced by harmonic confinement. The trap introduces a new time-scale $t_{\text{trap}} \sim 2\pi/\omega \sim 100$ ms, where ω is the trapping frequency. The dynamics is different depending on whether t_{soc} and t_{mf} are fast or slow compared to the trap period. If $t_{\text{soc}} \sim t_{\text{mf}} \ll t_{\text{trap}}$, we locally recover the physics of the homogeneous case, *i.e.* the magnetization dynamics at each point in the trap will be the same as in the uniform case, however the parameter λ will vary in space as $\lambda(r) = gn(r)/(\alpha p_{\text{th}})$, where $n(\mathbf{r})$ is the local density. If the timescale for spin-orbit coupling and the trap are comparable, the total magnetization displays collapse and revival dynamics [18, 87]. Recent proposals of using pulsed magnetic fields to generate tunable spin-orbit couplings [29, 30] and the demonstration of nearly uniform, “box” potentials [93], will enable experimentalists to explore this wide regime of parameters.

4.4 Conclusion

In summary, we have shown that out-of-equilibrium dynamics of quantum spins in an otherwise classical gas leads to non-trivial steady states and associated dynamical transitions. The steady states we describe are far from thermal equilibrium, and their stability relies on the absence of collisions. In cold atom experiments, the strength of interactions can be made weak enough such that the number of collisions throughout the duration experiment are negligible. However, on long enough times, collisions will eventually lead to thermalization and a disappearance of the steady states we describe. Our numerical simulations indicate that the steady states and dynamical transitions we find also occur for more general forms of SOC.

Experiments on spin-orbit coupled Fermi gases are already beginning to explore spin dynamics driven by SOC [21]. A systematic investigation of how spin dynamics is influenced by temperature and interactions is an active area of study [94,95], and is of considerable relevance to future experiments on strongly correlated spin-orbit coupled quantum gases.

Chapter 5: Stoner Ferromagnetism in a Thermal Pseudospin-1/2 Bose Gas

5.1 Introduction

The interplay between superfluidity/superconductivity and competing orders such as magnetism or density-wave ordering is one of the main challenges in the physics of strongly correlated systems, ranging from high- T_c superconductors to neutron stars. A paradigmatic system where this physics can be explored is a two-component Bose gas [78, 96, 97]. While the zero temperature physics of binary Bose condensates (BEC) is well understood [98, 99], attention is turning to understanding the properties of strongly interacting binary systems which can be realized either by using Feshbach resonances [84], optical lattices [46, 100] or band engineering [78]. Such systems exhibit a variety of novel phenomena such as a paramagnetic-ferromagnetic transition [78], stripe orders [20, 32], and Mott states with residual phase coherence [48, 101]. Here we discuss the normal state properties of an interacting, pseudospin-1/2 Bose gas, finding a rich phase diagram, where magnetic order occurs even without superfluidity.

Our main result is summarized in Fig. 5.1, which shows the phase diagram of a

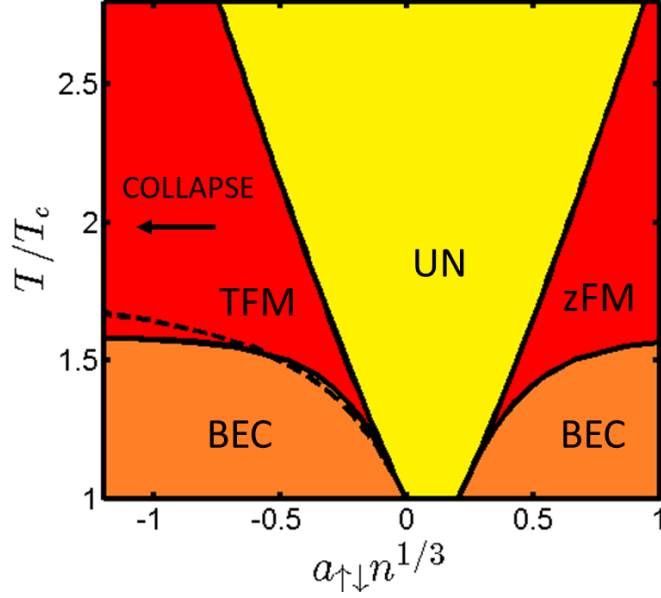


Figure 5.1: **3D Finite-temperature phase diagram of a pseudospin-1/2 Bose gas**— Intra-species interactions are repulsive ($g_{\uparrow\uparrow} = g_{\downarrow\downarrow} = g = 4\pi\hbar^2 a/m > 0$; we set $an^{1/3} = 0.1$), while the inter-species interaction $g_{\uparrow\downarrow}$ varies. T_c is the ideal gas Bose condensation temperature (only $T > T_c$ is shown), $a_{\uparrow\downarrow}$ is the inter-species scattering length, and n is the total density. For $|g_{\uparrow\downarrow}|$ greater than a critical value, system develops ferromagnetic order in z -direction (ZFM)/ $x-y$ plane (TFM) above the superfluid transition. Collapse occurs for sufficiently large negative $g_{\uparrow\downarrow}$ (see Fig. 5.2). Dashed line shows the transition between the normal unpolarized state (UN) and the paired state. TFM is always favored over pairing in 3D.

uniform pseudospin-1/2 Bose gas with contact interactions in three dimensions (3D) as a function of temperature (T) and the inter-spin interaction parameter ($g_{\uparrow\downarrow}$). This phase diagram was calculated within a self-consistent Hartree-Fock (HF) approximation, described below. Due to the synthetic nature of the spin, contact interactions generally do not preserve spin-rotational symmetry, and break it down to $U(1) \times Z_2$ in the underlying Hamiltonian. This leads to the appearance of intermediate *normal* magnetic phases at finite temperature, in addition to the unpolarized normal phase (UN). For repulsive inter-component interactions, we find an easy-axis ferromagnet in the z -direction (zFM), which breaks Z_2 symmetry; for attractive interactions, we

predict an easy-plane transverse ferromagnet, which breaks $U(1)$ symmetry in the $x - y$ plane.

The transition from a fully disordered phase to the zFM for strong repulsive $g_{\uparrow\downarrow}$ is reminiscent of the Stoner transition in an itinerant electronic system (such as ultra-cold Fermi gases or a screened Coulomb gas). There, the large repulsive interaction energy cost can be offset by the formation of ferromagnetic domains. Recently, itinerant ferromagnetism was investigated in strongly interacting ultra-cold Fermi gases [102–104], which concluded that the Stoner transition is preceded by the rapid formation of bound pairs, that lead to atom loss, preventing the observation of ferromagnetism [104]. Here we show that for the analogous bosonic system, the critical interaction strength for the onset of ferromagnetism is lower ($k_{\text{T}}a_{\uparrow\downarrow} \sim 0.6$, $k_{\text{T}} = \sqrt{2m/\beta}/\hbar$, whereas in a Fermi system $k_{\text{F}}a_{\uparrow\downarrow} \sim 1$, where k_{F} is a Fermi momentum), which opens up the intriguing possibility of observing itinerant ferromagnetism in a *Bose* gas. Importantly, in the normal state, three-body losses are strongly suppressed, and lifetimes of $\tau \sim 1\text{s}$ have been observed [93, 105].

We also investigate the possibility of BCS-like pairing with attractive inter-species interactions. The study of boson pairing was originally motivated by exciton condensation in semi-conductors. Nozières and Saint James [106] argued that such a phase is the ground state of a spin-1 Bose gas under appropriate conditions. Recently, a paired phase of spin-1 bosons was predicted above the condensation temperature, which competes with Bose condensation [107]. Here we find that ferromagnetism wins over pairing in 3D, but pairing becomes energetically competitive in quasi-2D, suggesting that a stable paired phase may indeed occur.

5.2 The model

We study a uniform system of pseudospin-1/2 bosons with contact interactions

$$\hat{H} = \hat{H}_{\text{kin}} + \hat{H}_{\text{int}}:$$

$$\hat{H}_{\text{kin}} = \int d\mathbf{r} \sum_{\sigma=\uparrow,\downarrow} \hat{\psi}_{\sigma}^{\dagger}(\mathbf{r}) \left(-\frac{\hbar^2}{2m} \nabla^2 - \mu_{\sigma} \right) \hat{\psi}_{\sigma}(\mathbf{r}), \quad (5.1)$$

$$\hat{H}_{\text{int}} = \int d\mathbf{r} \sum_{\sigma,\sigma'=\uparrow,\downarrow} \frac{g_{\sigma,\sigma'}}{2} \hat{\psi}_{\sigma}^{\dagger}(\mathbf{r}) \hat{\psi}_{\sigma'}^{\dagger}(\mathbf{r}) \hat{\psi}_{\sigma'}(\mathbf{r}) \hat{\psi}_{\sigma}(\mathbf{r}), \quad (5.2)$$

where m is atomic mass, μ_{σ} is the chemical potential and $g_{\sigma,\sigma'} = 4\pi\hbar^2 a_{\sigma,\sigma'}/m$ are interaction coefficients ($a_{\sigma,\sigma'}$ are the corresponding s-wave scattering lengths). Throughout, we assume, $g_{\uparrow\uparrow} = g_{\downarrow\downarrow} = g > 0$. In addition to the $U(1)$ symmetry associated with $\psi_{\sigma} \rightarrow \psi_{\sigma} e^{i\theta}$, the Hamiltonian has $U(1) \times Z_2$ symmetry in spin space. The Z_2 symmetry can be explicitly broken by making $g_{\uparrow\uparrow} \neq g_{\downarrow\downarrow}$ or $\mu_{\uparrow} \neq \mu_{\downarrow}$. We assume a spin balanced gas, and set $\mu_{\uparrow} = \mu_{\downarrow}$.

5.3 Random phase approximation

We obtain the instabilities of the normal state by computing the spin susceptibility within a Random Phase approximation (RPA) which includes exchange [79, 107, 108]. An instability towards ferromagnetism is signaled by a divergence in the spin susceptibility at zero frequency and wave-vector. The susceptibility tensor reads:

$$\chi_{\alpha\beta,\gamma\eta}(\mathbf{k}, t) = \frac{\theta(t)}{iV} \sum_{\mathbf{p}, \mathbf{q}} \langle [\hat{a}_{\mathbf{p}\alpha}^{\dagger}(t) \hat{a}_{\mathbf{k}+\mathbf{p}\beta}(t), \hat{a}_{\mathbf{q}\gamma}^{\dagger}(0) \hat{a}_{\mathbf{q}-\mathbf{k}\eta}(0)] \rangle, \quad (5.3)$$

where $\alpha, \beta, \gamma, \eta = (\uparrow, \downarrow)$ and V is the volume. The non-interacting susceptibility is: $\chi_{\alpha\beta,\gamma\eta}^0 = \chi^0$ for $\alpha = \eta$ and $\beta = \gamma$, $\chi_{\alpha\beta,\gamma\eta}^0 = 0$ otherwise. In 3D, $\chi^0(\mathbf{k} =$

$0, \omega = 0) = -[(m/2\pi\hbar^2)^{3/2}/\sqrt{\beta}] \text{Li}_{1/2}(e^{\beta\mu})$ [107], where $\beta = 1/k_B T$ and $\text{Li}_s(z)$ is the polylogarithm function of order s .

The interacting susceptibility (χ^{RPA}) in terms of χ^0 , and the interaction matrix $V_{\alpha\beta,\gamma\eta}$ is:

$$\chi_{ij,mn}^{\text{RPA}} = \chi_{ij,mn}^0 + \sum_{\alpha\beta\gamma\eta} \chi_{ij,\alpha\beta}^0 V_{\alpha\beta,\gamma\eta} \chi_{\gamma\eta,mn}^{\text{RPA}}, \quad (5.4)$$

where $V_{\alpha\beta,\gamma\eta} = g_{\uparrow\downarrow} \delta_{\alpha,\bar{\gamma}} \delta_{\beta,\bar{\eta}} + 2g(\delta_{\alpha,1} \delta_{\beta,1} \delta_{\gamma,1} \delta_{\eta,1} + \delta_{\alpha,2} \delta_{\beta,2} \delta_{\gamma,2} \delta_{\eta,2})$ ($\bar{\uparrow} = \downarrow, \bar{\downarrow} = \uparrow$). We are interested in the static density and magnetization susceptibilities: $\chi_n = \delta n / \delta U$, $\chi_i = \delta m_i / \delta B_i$, (n is the density, U is an external potential, and m_i and B_i are components of the magnetization and magnetic field). The RPA susceptibilities read:

$$\begin{aligned} \chi_n^{\text{RPA}} &= \frac{2\chi^0}{1 - (2g + g_{\uparrow\downarrow})\chi^0}, \\ \chi_x^{\text{RPA}} &= \chi_y^{\text{RPA}} = \frac{2\chi^0}{1 - g_{\uparrow\downarrow}\chi^0}, \\ \chi_z^{\text{RPA}} &= \frac{2\chi^0}{1 - (2g - g_{\uparrow\downarrow})\chi^0}. \end{aligned} \quad (5.5)$$

The density susceptibility diverges for strong-enough attractive interactions, $2g + g_{\uparrow\downarrow} = 1/\chi^0$ ($\chi^0 < 0$), which marks collapse [107]. Absent long-range interactions, the dominant instability in the density and spin channel occurs at $\mathbf{k} = 0$.

The divergence in χ_x , χ_y or χ_z signals a transition to a ferromagnetic phase along the transverse or longitudinal direction respectively. The transition to an Ising ferromagnet (zFM) occurs only for sufficiently repulsive $g_{\uparrow\downarrow}$ ($g_{\uparrow\downarrow} = 2g - 1/\chi^0$), whereas the transition to a $x - y$ ferromagnet occurs for arbitrarily weak attractive $g_{\uparrow\downarrow}$ ($g_{\uparrow\downarrow} < 1/\chi^0$) (Fig. 5.1) [109]. This is because the zFM has to overcome the extra repulsion from the intra-component interaction term. The TFM has recently been

predicted in Rashba spin-orbit coupled bosons [110], but spin-orbit coupling is in fact not necessary for this phase.

5.4 Hartree-Fock theory

The RPA analysis only yields the location of the instability lines and to obtain the complete finite temperature phase diagram, we use a self-consistent Hartree-Fock mean-field theory. We define mean-fields $n_{\sigma,\sigma'} = \frac{1}{V} \sum_{\mathbf{k}} \langle \hat{a}_{\mathbf{k},\sigma}^\dagger \hat{a}_{\mathbf{k},\sigma'} \rangle \neq 0$. The Hartree-Fock Hamiltonian then reads: $\hat{H}_{\text{HF}} = \sum_{\mathbf{k},\sigma,\sigma'} \hat{a}_{\mathbf{k},\sigma}^\dagger \mathcal{H}_{\sigma,\sigma'}(\mathbf{k}) \hat{a}_{\mathbf{k},\sigma'} - E_0$,

$$\mathcal{H}(\mathbf{k}) = \begin{pmatrix} \epsilon_k + 2gn_\uparrow + g_{\uparrow\downarrow}n_\downarrow & g_{\uparrow\downarrow}n_{\uparrow\downarrow}^* \\ g_{\uparrow\downarrow}n_{\uparrow\downarrow} & \epsilon_k + 2gn_\downarrow + g_{\uparrow\downarrow}n_\uparrow \end{pmatrix}. \quad (5.6)$$

where $E_0 = V [g(n_\uparrow^2 + n_\downarrow^2) + g_{\uparrow\downarrow}(n_\uparrow n_\downarrow + |n_{\uparrow\downarrow}|^2)]$, $\epsilon_k = \hbar^2 k^2 / (2m) - \mu$. \hat{H}_{HF} can be easily diagonalized: $\hat{H}_{\text{HF}} = \sum_{\mathbf{k},j} E_j(\mathbf{k}) \hat{b}_j^\dagger(\mathbf{k}) \hat{b}_j(\mathbf{k}) - E_0$, and in thermal equilibrium the occupation number is given by the Bose distribution $\langle \hat{b}_j^\dagger(k) \hat{b}_j(k) \rangle = [e^{\beta E_j(k)} - 1]^{-1}$. The state of the system at temperature T can be obtained by finding the self-consistent mean-field Hamiltonian, or by minimizing the free energy of the system by varying \bar{n}_\uparrow , \bar{n}_\downarrow and $\bar{n}_{\uparrow\downarrow}$.

The HF analysis predicts a second order transition to two normal ferromagnetic phases: zFM for repulsive and TFM for attractive $g_{\uparrow\downarrow}$, at exactly the same temperatures as predicted by the RPA theory. This is not surprising because the RPA susceptibilities can be obtained by linearizing the Hartree-Fock equations of motion [79].

When the chemical potential reaches the bottom of the lower band in Eq. (5.6),

a BEC transition occurs. While the critical temperature for the transition between the unpolarized normal and BEC does not change with the interaction strength (interactions merely yield a constant shift to the chemical potential), the transition between the normal ferromagnetic and BEC phases (T'_c) is interaction-dependent (see Fig. 5.1). This is because ferromagnetism splits the degeneracy between \uparrow and \downarrow in Eq. (5.6). In the extreme limit $g_{\uparrow\downarrow} \rightarrow \infty$, there is only one band, and T'_c approaches $2^{2/3}T_c$ (Fig. 5.1), the critical temperature for Bose condensation of non-interacting spinless bosons. We also note that when the HF approximation is extended to the BEC phase, it predicts the condensation transition to be first-order, which is an artifact of the approximation [109].

Although we do not expect our theory to be quantitatively accurate near the phase boundary, we believe that it correctly captures qualitative aspects of the phase diagram. Higher-order terms are expected to modify the absolute value of the BEC transition temperature, it is found to increase in a uniform system [111,112], and decrease it in harmonic trap [113]. Analogous to the case of the usual Stoner transition in itinerant fermions, fluctuations may also raise the ferromagnetic transition temperature, and make the transition first order [102]. A careful analysis of these beyond mean-field effects will be the subject of future work.

5.5 Pairing and collapse for attractive interactions

In analogy with spin-1/2 fermions, it is natural to ask whether attractive interactions between \uparrow and \downarrow bosonic particles could also lead to Cooper pairing.

Such exotic paired states of bosons have been discussed in the context of exciton condensation in semiconductors [106,114], however to date, there is no experimental evidence for such a phase. Here we look for a transition between the unpolarized normal, and paired state using a bosonic analog of Bardeen-Cooper-Schrieffer (BCS) theory [115]. We assume a non-zero pairing field $\Pi_{\uparrow\downarrow} = \frac{1}{V} \sum_{\mathbf{k}} \langle \hat{a}_{\mathbf{k}\uparrow} \hat{a}_{\mathbf{k}\downarrow} \rangle$ [115] which yields a BCS-like Hamiltonian:

$$\hat{H}_p = \sum_{\mathbf{k}\sigma} \epsilon_k \hat{a}_{\mathbf{k}\sigma}^\dagger \hat{a}_{\mathbf{k}\sigma} + g_{\uparrow\downarrow} (\Pi_{\uparrow\downarrow}^* \hat{a}_{\mathbf{k}\uparrow} \hat{a}_{\mathbf{k}\downarrow} + \text{h.c.}) - V g_{\uparrow\downarrow} |\Pi_{\uparrow\downarrow}|^2. \quad (5.7)$$

We do not explicitly include HF terms since, in the absence of ferromagnetism (or long range interactions), these terms only produce a constant shift in energy. By self-consistently solving for the ground-state of the pairing Hamiltonian \hat{H}_p , we obtain the implicit equation for the pairing order parameter (bosonic BCS ‘‘gap equation’’):

$$\frac{1}{g_{\uparrow\downarrow}} = -\frac{1}{V} \sum_{\mathbf{k}} \left[\frac{1}{E_k} \left(\frac{1}{e^{\beta E_k} - 1} + \frac{1}{2} \right) - \frac{1}{2\epsilon_k^0} \right], \quad (5.8)$$

where $E_k = \sqrt{\epsilon_k^2 - g_{\uparrow\downarrow}^2 |\Pi_{\uparrow\downarrow}|^2}$ and $\epsilon_k^0 = \hbar^2 k^2 / 2m$. Here we regularized the interaction strength $g_{\uparrow\downarrow} \rightarrow g_{\uparrow\downarrow} + (g_{\uparrow\downarrow}^2 / V) \sum_{k < k_c} 1 / (2\epsilon_k^0)$ to avoid the unphysical ultra-violet divergence.

Solving Eq. 5.8, we indeed find a transition to a paired phase, but the transition temperature for pairing is lower than that for the TFM phase (Fig. 5.1). For $g_{\uparrow\downarrow} \rightarrow 0^-$, both transition lines converge to $T/T_c = 1 - C a_{\uparrow\downarrow} n^{1/3}$, $C \approx 1.848$. To study the potential coexistence between paired and ferromagnetic phases, we perform an unrestricted Hartree-Fock Bogoliubov analysis, in which we assume both $\bar{n}_{\uparrow\downarrow} \neq 0$, $\Pi_{ij} \neq 0$, where $i, j = (\uparrow, \downarrow)$. However, we do not find a state which minimizes the free energy, where both ferromagnetic and pairing order parameters are simultaneously

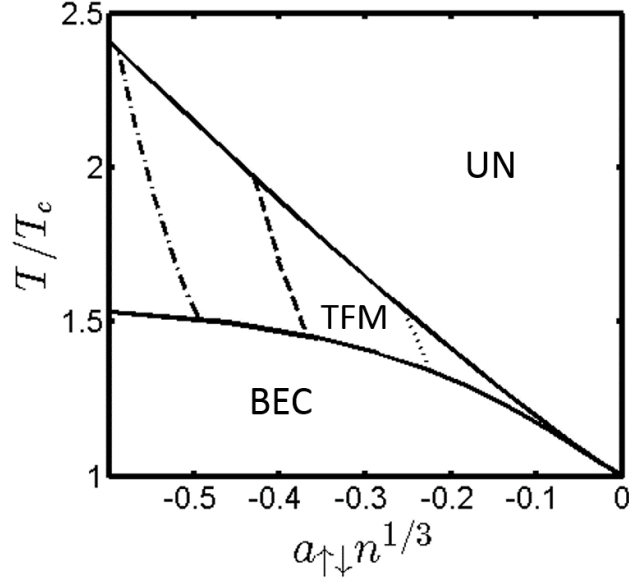


Figure 5.2: Thermodynamic instability in $g_{\uparrow\downarrow} < 0$ region in 3D. UN is thermodynamically stable for $g > 0$, while the TFM is stable in the region on the right side of the instability lines: dotted line ($an^{1/3} = 0.4$), dashed line ($an^{1/3} = 0.5$) and dashed-dotted line ($an^{1/3} = 0.6$).

nonzero. Below we show that the possibility of pairing is strongly enhanced in lower dimensions, owing to the presence of a bound state.

As the transition to TFM occurs for attractive interactions, it is important to ask if the gas is thermodynamically stable [116]. We compute the pressure and isothermal compressibility to find the stable part of the phase diagram in the region with $g_{\uparrow\downarrow} < 0$. Fig. 5.2 shows the mechanical instability lines for different values of $a_{\uparrow\downarrow}n^{1/3}$. While the UN phase is stable in the entire region plotted, the TFM phase is stable only to the right of the instability lines. Increasing repulsive g increases the window of stability of the TFM phase.

5.6 Magnetism and pairing in 2D

We now turn to the finite temperature phase diagram in quasi-2D, which can be realized experimentally by confinement in the z -direction. In quasi-2D, one has a new length scale, $a_z = \sqrt{\hbar/m\omega_z}$, where ω_z is the confinement frequency. This leads to a momentum-dependent 2D interaction [117, 118]:

$$g_{2D} = \frac{2\sqrt{2\pi}\hbar^2}{m} \frac{1}{a_z/a + (1/\sqrt{2\pi}) \ln(B/\pi q^2 a_z^2)}, \quad (5.9)$$

where q is the relative momentum of two particles and $B = 0.915\dots$

We repeat the RPA and Hartree-Fock analysis using g_{2D} , and set $q = k_T$ [118]. We again find zFM and TFM phases with transition lines given by same expressions as in 3D, however χ^0 becomes: $\chi_{2D}^0 = -(m/2\pi\hbar^2) Li_0(e^{\beta\mu})$. In 2D there is no Bose-Einstein condensation at finite temperature, however there is a superfluid phase below the Berezinskii-Kosterlitz-Thouless temperature (T_{BKT}). The approximate T_{BKT} for a 2D spinless Bose gas is $T_{BKT}/T_0 = 4\pi/\log(75.8a_z/a)$ [119], where $T_0 = \hbar^2 n/2mk_B$.

We look for pairing using the same BCS mean-field approach, however with the renormalization of interaction appropriate for a quasi-2D system [120]: $-1/g_{2D} = \sum_{\mathbf{k}} (\hbar^2 k^2/m + \epsilon_B)^{-1}$, where ϵ_B is the energy of a two-atom bound state which is related to $a_{\uparrow\downarrow}$ and a_z as $\epsilon_B = 4\hbar^2/(ma_{2D}^2 e^{2\gamma})$, where $a_{2D} = a_z(2\sqrt{\pi/B}/e^\gamma)e^{-\sqrt{\pi/2} a_z/a_{\uparrow\downarrow}}$ and $\gamma = 0.577\dots$ [118, 121].

There are four independent characteristic lengths in the system: $a_{\uparrow\downarrow}$, a_z , $1/\sqrt{n}$, $1/k_T$. At fixed a , there are three dimensionless parameters: $a_{\uparrow\downarrow}/a_z$, $k_T^2/n =$

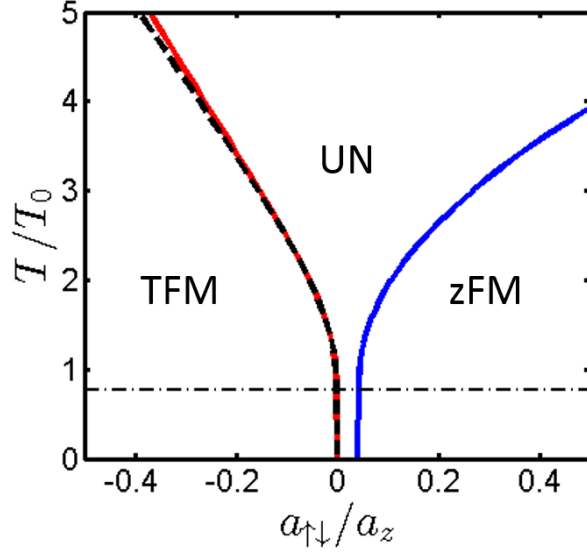


Figure 5.3: Phase diagram in quasi-2D as a function of temperature and interactions for $\eta = 0.1$. We set $a/a_z = 0.02$ and define $T_0 = \hbar^2 n / 2mk_B$. Blue line shows transition between UN and zFM phase, red line shows transition between UN and TFM phase, dashed-dotted black line corresponds to BKT transition temperature calculated for $a_{\uparrow\downarrow} = 0$. The dashed black line represents the transition between UN and the paired phase.

T/T_0 and $\eta = \sqrt{n}a_z$. In Fig. 5.3, we show the phase diagram as a function of $a_{\uparrow\downarrow}/a_z$ and T/T_0 for $\eta = 0.1$. Surprisingly, unlike in 3D, the critical temperature for transverse-ferromagnetic and paired order nearly coincide over a wide range of $a_{\uparrow\downarrow}/a_z$, suggesting that a stable paired phase may indeed occur in a more sophisticated treatment which includes fluctuations beyond mean-field. In particular, as the TFM and paired states are associated with $U(1)$ symmetry breaking, in 2D, we expect vortices, which are absent in the present treatment, to play an important role. In quasi-1D, pairing should become even more favorable as the tendency to form bound states is much stronger in 1D.

5.7 Experimental detection

In a system where the pseudospin particle number is conserved, the zFM will appear in the form of spin domains, which can either be measured *in situ* [78], or using speckle imaging [104]. The transverse components of the magnetization can be similarly obtained by using spin-echo techniques in conjunction with *in situ* imaging [122].

The experimental realization of zFM or TFM phases in the 3D bosonic system requires moderate interactions. As Fig. 5.1 shows, the FM phases should be observable for $a_{\uparrow\downarrow}n^{1/3} \sim -0.3$ ($k_T a_{\uparrow\downarrow} \sim -0.75$) for TFM, and $a_{\uparrow\downarrow}n^{1/3} \sim (2an^{1/3} + 0.3)$ for zFM. In comparison, ^{87}Rb has $an^{1/3} \sim 0.02$, which means Feshbach resonances are essential for the realization of normal FM phases. However strongly interacting two-component gases can be realized using ^{85}Rb - ^{87}Rb mixtures [84, 123], or in ^{133}Cs , where lattice shaking techniques can be used to create synthetic spin-1/2 systems [78]. The situation is better in quasi-2D, where the region occupied by magnetic/paired phases is larger even for weak $g_{\uparrow\downarrow}$. Despite the need for moderate interactions, we stress that this physics occurs in the normal state, where three-body loss rates are significantly lower than in a degenerate gas [93, 105].

5.8 Stripe order in the presence of SOC?

We have generalized the RPA and Hartree-Fock theories presented above, to include the 1D spin-orbit coupling (SOC), realized at NIST [7]. SOC splits the

degenerate spin- \uparrow and \downarrow bands, and introduces a gap (proportional to the Raman coupling strength), and shifts the minimum of the lower band to finite wave-vectors $\pm k_0$, where k_0 is the wave-vector of the Raman lasers. At $T = 0$, for weak Raman coupling and interactions, condensation occurs at $\pm k_0$, and the quantum interference of these two matter waves produces a density-wave, which spontaneously breaks translational symmetry in real space.

It is extremely interesting to ask whether stripe order survives thermal fluctuations, and whether a normal stripe phase could occur in this system. Repeating the RPA (see Appendix D) and Hartree-Fock analyses presented above for the NIST SOC scheme, we do not find any finite wave-vector instabilities. Our negative result indicates that the stripe order melts below the transition temperature for Bose condensation, which is consistent with the experimental observations of Ji *et al.* [23] and theoretical investigation by Hickey and Paramakanti [124]. Raman coupling also shifts the zFM transition to stronger interactions. This is not surprising as in the limit of large Raman coupling, the system reduces to a spinless Bose gas.

5.9 Conclusion

Observing a bosonic analog of the Stoner transition would constitute an important advance in our understanding of interacting Bose systems. Here we have established the finite temperature phase diagram of a two-component Bose gas, finding two normal, stable itinerant ferromagnetic phases, where magnetic order occurs without superfluidity. Understanding how superfluidity arises in the presence

of magnetism has interesting parallels with ongoing studies of strongly correlated electronic systems. Strikingly, in 2D, we have discussed the exciting possibility of an exotic Cooper paired state of bosons. More sophisticated calculations will be required to fully settle the question of whether pairing occurs in 2D, and this is the subject of future work. We also concluded that in the case of spin-orbit coupling there is no translational symmetry breaking in the normal phase in the continuum, consistent with recent experiments [\[23\]](#).

Chapter 6: Strong Correlation Effects in a Two-Dimensional Bose Gas with Quartic Dispersion

6.1 Introduction

One of the most remarkable advances in ultra-cold atomic gases in the recent years has been the ability to engineer at will, dispersions with single-particle degeneracies or almost completely flat bands. For example, optical superlattices have been used to generate honeycomb, Kagomé and Lieb lattice geometries [125, 126]. Lattice shaking [8, 127] and Raman assisted tunneling in real and spin space has been used to realize spin-orbit coupling (SOC) [6, 7], synthetic vector potentials, and subsequently topological bands [15, 16]. Attention has now turned to studying the interplay between these non-trivial single-particle band structures, spin and interactions, which paves the way to accessing a rich variety of phases such as skyrmion lattices [128], integer and fractional Chern insulators [129, 130], Wigner crystals [131], and other exotic states [132]. In this chapter we present a variational study of a low-density, 2D Bose gas at zero temperature in a dispersion which is quartic in one direction, and which can be realized experimentally [7, 8].

An interesting example of non-trivial interplay between single-particle degen-

eracies and interactions is a 2D Rashba SOC gas. Here the low-energy dispersion has an infinite ring degeneracy in momentum space, and the density of states has the form $dn/dE \sim E^{-1/2}$, typical for 1D systems. At low densities, atoms sample the ring degeneracy and interesting physics emerges. The consequences of this were first explored by Berg, Rudner and Kivelson [131] in the context of Fermi gases. They observed that while the kinetic energy delocalizes the particles over the Rashba ring, atoms can minimize the short range interaction energy by localizing in momentum space. This competition produces a plethora of possible symmetry broken ground-state phases ranging from Wigner crystals to ferromagnetic nematic states.

Even more interesting and perhaps less understood is the fate of *bosons* in single-particle degeneracies. On the one hand, by developing fermionic correlations, bosons can completely avoid (spinless case) or suppress (spinful case) short-range repulsive interactions, but such a state is spread out in momentum space. The kinetic energy cost associated with this spreading is parametrically lower in flat bands, and one can expect a regime of densities where *fermionized* wave functions have lower energy than a mean-field condensate. The key theoretical challenge in addressing this question is that single particle degeneracies enhance fluctuation effects, rendering mean-field theory invalid, and Quantum Monte Carlo usually suffers from a sign problem, and can only study small system sizes. Progress has to be made either by guessing trial wave-functions or using field theoretical methods which capture the low energy dynamics. For Rashba SOC [19] and moat bands, Sedrakyan *et al.* [26, 133] have proposed a composite-fermion description, which spontaneously

breaks time reversal and parity symmetry and has lower energy than the weak-coupling BEC. Spinless bosons in quartic bands of the form $\varepsilon_{\mathbf{k}} \sim \mathbf{k}^4$, were studied recently using field theoretic techniques by the authors of Refs. [134, 135], who proposed that condensation is strongly suppressed in favor of a liquid with algebraically decaying spatial correlations.

Motivated by experiments, we address the question of fermionization versus Bose condensation in a 2D Bose gas in the NIST SOC [7] or Chicago shaken lattice scheme [8], where the dispersion can be tuned to take the form $\varepsilon_{\mathbf{k}} \sim k_x^4/4 + k_y^2 + \dots$. We compare the energy of the mean-field Bose condensate to several trial many-body states, summarized in Table 6.1: (i) a Wigner crystal (ii) the absolute value and the square of the Fermi-sea wave-function (iii) the absolute value and the absolute value squared of the $\nu = 1$ Laughlin state (proposed by the authors of Refs. [26, 133]) and (iv) the Jastrow ansatz [136]. While all the wave-functions (i)-(iv) have an energy per particle which scales as $\epsilon \sim n^{4/3}$ in the low-density limit (to be precisely defined below), and are thus energetically favorable over the mean-field condensate ($\epsilon \sim n$), we find that the trial wave-function with the lowest energy is of Jastrow type, and has finite condensate fraction and true long-range order.

6.2 The model

We study a two-dimensional (pseudo)spin-1/2 Bose system with spin-orbit coupling, which was experimentally realized at NIST [7]:

$$H_{\text{soc}}(\mathbf{k}) = \frac{\hbar^2 \mathbf{k}^2}{2m} + \frac{\hbar^2 k_L}{m} k_x \sigma_z + \frac{\Omega_R}{2} \sigma_x, \quad (6.1)$$

where k_L is the Raman laser wave-vector, Ω_R is the Raman coupling strength, and $\sigma_{x,y,z}$ are Pauli matrices. The spectrum of the Hamiltonian has two bands, for $\Omega_R < 4E_R$, where $E_R = \hbar^2 k_L^2 / 2m$ is the laser recoil energy, the lower band has two degenerate minima, while for $\Omega_R \geq 4E_R$ it has a single minimum at $\mathbf{k} = 0$ [7]. While the dispersion around each minimum is parabolic, at $\Omega_R = 4E_R$, the dispersion in the x -direction develops a quartic structure. In the case of a Bose gas, this gives rise to interesting behavior at low densities, which is the main topic of this work. From now on, we will be interested only in the $\Omega_R = 4E_R$ case. We remark that while the Rabi coupling term explicitly breaks physical time-reversal symmetry, this Hamiltonian has an additional Z_2 symmetry associated with the transformation $|k_x, \uparrow\rangle \rightarrow \langle -k_x, \downarrow|$.

Expressing energy in units of E_R and momentum (length) in units of $\hbar k_L$ ($1/k_L$), the dimensionless single-particle Hamiltonian reads:

$$H_{\mathbf{k}} = \mathbf{k}^2 + 2k_x \sigma_z + 2(\sigma_x + \mathbb{1}). \quad (6.2)$$

We choose the energy offset such that the minimum of the lower band is at zero energy.

We assume the inter-particle interactions are described by a spin-independent contact potential (in units of E_R and $1/k_L$)

$$V_{\text{int}}(\mathbf{r}_1 - \mathbf{r}_2) = g \delta(\mathbf{r}_1 - \mathbf{r}_2) \mathbb{1}_{\sigma_1 \otimes \sigma_2}, \quad (6.3)$$

where $g = 2mU_0/\hbar^2$ ($U_0 > 0$ is the contact interaction strength and in a quasi-2D regime $U_0 = 2\sqrt{2\pi}\hbar^2 a/(ma_z)$, where a is a 3D scattering length and a_z is the confinement length in z direction [117]), $\mathbb{1}_{\sigma_1 \otimes \sigma_2}$ is a unit operator in the space of two

spins, $\mathbb{1}_{\sigma_1 \otimes \sigma_2} = \sum_{s_1, s_2} |s_1 s_2\rangle \langle s_1 s_2|$, where $s_j \in (\uparrow, \downarrow)$. In reality, the interactions are typically spin-dependent, however our results are insensitive to spin dependence. We emphasize that throughout, we focus on the regime of weak interactions, but nonetheless find interesting ground states by engineering the single-particle dispersion.

The spectrum of H_k is $\varepsilon_{\pm} = \mathbf{k}^2 \pm 2\sqrt{k_x^2 + 1} + 2$ and the lower-band energy can be expanded around $\mathbf{k} = 0$ as $\varepsilon_-(\mathbf{k}) = k_x^4/4 + k_y^2 + \dots$. The lower-band eigenstates of H_k are

$$\begin{bmatrix} s_{\uparrow}(\mathbf{k}) \\ s_{\downarrow}(\mathbf{k}) \end{bmatrix} = \mathcal{N}_k \begin{bmatrix} k_x - \sqrt{1 + k_x^2} \\ 1 \end{bmatrix}, \quad (6.4)$$

where $\mathcal{N}_k = \left[1 + (k_x - \sqrt{1 + k_x^2})^2\right]^{-1/2}$ is the normalization factor. Notice that at low densities ($n \ll k_L^2$, in original units), particles occupy only the states close to the minimum of the band, i.e. the width of the momentum distribution $\Delta k_x \rightarrow 0$ as $n \rightarrow 0$. In that case, Eq. (6.4) reduces to $[s_{\uparrow}(\mathbf{k}) \ s_{\downarrow}(\mathbf{k})] = [-1 \ 1]/\sqrt{2}$, and spin eigenstates become (approximately) momentum independent. The gas then becomes effectively spinless, and is described by the Hamiltonian:

$$\mathcal{H}_{\mathbf{k}} = \frac{1}{4}k_x^4 + k_y^2, \quad (6.5)$$

with $\mathcal{V}_{\text{int}}(\mathbf{r}_1 - \mathbf{r}_2) = g \delta(\mathbf{r}_1 - \mathbf{r}_2)$. Such a Hamiltonian can be directly realized using the shaking lattice scheme of Parker *et al.* [8].

In the first part of this chapter, we focus on the physics of the effective Hamiltonian Eq. (6.5) above, and then show that our conclusions remain unchanged even after the inclusion of spin (corresponding to the NIST scheme [7]).

6.3 Bogoliubov mean-field theory

We start by considering the most conventional description of a 2D Bose gas at zero temperature, namely the Bogoliubov mean-field description. The main assumption in Bogoliubov's approach is that the majority of particles are condensed in $\mathbf{k} = 0$ state, and others occupy $\mathbf{k} \neq 0$ states in the vicinity. Repulsive interactions deplete the condensate [35], and at the mean-field level, the energy per particle is given by $\epsilon = gn/2$, where n is the density. The condensate depletion is readily found to be [116]:

$$n_{\text{ex}} = \frac{1}{V} \sum_{\mathbf{k} \neq 0} \frac{1}{2} \left(\frac{\epsilon_{\mathbf{k}} + gn_0}{\sqrt{\epsilon_{\mathbf{k}}^2 + 2\epsilon_{\mathbf{k}}gn_0}} - 1 \right), \quad (6.6)$$

where $\epsilon_{\mathbf{k}}$ is a single-particle dispersion, n_{ex} is the density of depleted particles, n_0 is the condensate density, and g is the interaction strength. The behavior of the integral in (6.6) is usually a good indication of the fate of a BEC: for zero temperature, 2D and 3D systems with a parabolic dispersion, the integral is convergent, fluctuations do not destroy long-range order. In 1D, it diverges, signaling the absence of true long-range order.

In our case, $\epsilon_{\mathbf{k}} = k_x^4/4 + k_y^2$, the integral is convergent: $n_{\text{ex}} = 3.854(gn_0)^{3/4}$ (dimensionless variables). However, the ratio of the number of excited and condensed particles $n_{\text{ex}}/n_0 \sim n_0^{-1/4}$ (in a usual 2D parabolic case $n_{\text{ex}} \sim n_0$) shows that the Bogoliubov approach breaks down at low densities. This suggests that in the low-density limit, the ground state is *qualitatively* different from a mean-field condensate.

In the 3D case, $\varepsilon_{\mathbf{k}} = k_x^4/4 + k_y^2 + k_z^2$, the ratio of the number of excited and condensed particles is $n_{\text{ex}}/n_0 \sim n_0^{1/4}$. Therefore, in the low-density limit, the Bogoliubov description is valid, and we expect a mean-field BEC to provide a good description of the ground state.

6.4 Wigner crystal state

The first example of a strongly-correlated bosonic state we consider is the Wigner crystal (WC), proposed by Berg *et al.* [131], for the Rashba SOC case. The state is constructed by dividing the volume (area) in an array of identical rectangular boxes of size L_x, L_y , and putting each particle in a different box (see Fig.6.1). In contrast to a mean-field BEC state, the interaction energy of WC is zero, as particles completely avoid one another. This comes at the cost of higher kinetic energy, as single-particle states are localized in boxes, compared to a BEC, where occupied states extend throughout the entire volume.

To calculate the energy per particle of the WC state, it suffices to solve for the ground state of a single particle in a box. The calculation for the case of quartic dispersion is shown in Appendix A, and for Hamiltonian (6.5), it gives $E_g(L_x, L_y) = 1.285(\pi/L_x)^4 + (\pi/L_y)^2$, where L_x and L_y are the length and the width of the box. It is clear that at low densities (small \mathbf{k}), the kinetic energy is “cheaper” in the x than in the y direction. This means that we can lower the energy by deforming the box such that it is shorter in x and longer in y direction, while keeping the total volume of the box ($V = L_x L_y$), and the density ($n = 1/V$) fixed.

We find the ratio L_y/L_x which minimizes $E_g(L_x, L_y)$ is $L_y/L_x = 0.340 n^{-1/3}$ and the ground-state energy per particle is $E_g = 43.5 n^{4/3}$. Indeed, for the spinless case, the WC has lower energy than a mean-field BEC at low densities. By numerically solving the corresponding spinful problem [Eq.(6.2)], we have checked that the energy per particle is identical to the spinless case in the large L_x limit.

The WC state obviously has lower energy than a mean-field BEC at low densities, however it is a crystalline state which breaks translational symmetry. While this is expected to happen in low-density systems with long-range interactions, contact interactions typically do not favor formation of a crystal [137]. Therefore we expect a strongly-correlated state which is translationally invariant to have even lower energy than WC state.

We notice that here we considered only a particular type of a WC (rectangular lattice) and that different types of WC, e.g. triangular-lattice crystal, could have lower energy. Still, we later show that the Jastrow-type state has energy $\epsilon = 6.6 n^{4/3}$, which is smaller than our WC state by a factor of 7, and we do not believe different types of WC can achieve such low energies.

6.5 Strongly-correlated gas in the lower band

6.5.1 Non-interacting Fermi gas

The Wigner crystal example motivates us to look for other strongly correlated states, constructed out of lowest band wave-functions. One natural way to build correlations is to write down wave-functions where bosons avoid one another at

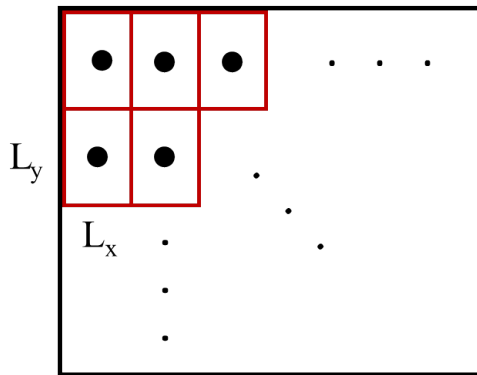


Figure 6.1: Schematic picture of the Wigner crystal state. Each particle occupies a different box. There is no overlap between particles and the interaction energy is zero.

short distances. To see how this lowers the energy, consider a non-interacting Fermi gas in the single-particle dispersion of Eq. (6.5). The density of states corresponding to (6.5) is $dn/dE = (3/2)/(2\pi)^{3/2} \times \Gamma(5/4)/\Gamma(7/4) E^{-1/4}$, where $\Gamma(x)$ is the gamma function. The energy per particle in the non-interacting Fermi gas is then $\epsilon = 6.84 n^{4/3}$, which is indeed lower than a mean-field BEC ($\epsilon = gn/2$), and the Wigner crystal at low densities.

It is well known that in a low-density 1D system with contact interactions, when the contact interactions dominate the kinetic energy, the Fermi gas has lower energy than the mean-field BEC at the same density. This leads to “fermionization” of bosons, and the formation of a Tonks-Girardeau gas [138].

We now compute the ground state energy of several appropriately symmetrized fermionic wave-functions. We first consider the spinless case, and then generalize our results to include spin.

6.5.2 Spinless system

6.5.2.1 “Fermionized” many-body states

The ground state of a non-interacting Fermi gas in the Hamiltonian (6.5) has the following momentum distribution widths: $\Delta k_x = (4E_F)^{1/4} \sim n^{1/3}$, $\Delta k_y = E_F^{1/2} \sim n^{2/3}$, where E_F is the Fermi energy. This means that, at low densities, the energy is minimized by broadening the distribution in the direction where kinetic energy is “cheap” (x direction) and squeezing it in the direction where energy is expensive (y direction). The WC state discussed above has the same property: $\Delta k_x \sim 1/L_x \sim n^{1/3}$ and $\Delta k_y \sim 1/L_y \sim n^{2/3}$.

To construct more general strongly-correlated bosonic wave-functions for the spinless gas, we take a fermionic state with the property $\Delta k_x \sim n^{1/3}$, $\Delta k_y \sim n^{2/3}$ and construct corresponding Bose wave-functions: for example $\psi_B = |\psi_F|$, $\psi_B = \psi_F^2$ or $\psi_B = |\psi_F|^2$. This way we obtain a symmetric bosonic wave-function which obeys $\Delta k_x \sim n^{1/3}$, $\Delta k_y \sim n^{2/3}$, and has kinetic energy $E_{\text{kin}}/N \sim (\Delta k_x)^4/4 + (\Delta k_y)^2 \sim n^{4/3}$, while the interaction energy is identically zero by construction. (In general, we can consider higher powers $\psi_B = |\psi_F|^n$ for $n > 2$ or ψ_F^{2n} , for $n > 1$, but these have higher energy, as discussed below.)

The total energy is then simply given by

$$E_{\text{kin}} = \int d\mathbf{k} n_{\mathbf{k}} \varepsilon_{\mathbf{k}}, \quad (6.7)$$

where $\varepsilon_{\mathbf{k}} = k_x^4/4 + k_y^2$ and $n_{\mathbf{k}}$ is the momentum distribution, normalized so that $\int d\mathbf{k} n_{\mathbf{k}} = N$. We compute the momentum distribution, and calculate the energy

using Monte Carlo integration (see Appendix B for details).

But which fermionic wave-functions should we choose? A natural choice is the ground state of a non-interacting Fermi gas ($\psi_{F,0}$). $\psi_{F,0}$ is a real function of spatial coordinates, and we construct two bosonic trial wave-functions: $\psi_{B,\text{abs}} = |\psi_{F,0}|$ and $\psi_{B,\text{sq}} = (\psi_{F,0})^2$.

In the case of the wave-function $\psi_{B,\text{abs}}$, the integral (6.7) diverges. The reason is that the first derivative of the wave-function is not continuous at points where $\psi_{B,\text{abs}} = 0$, which leads to a $\sim |\mathbf{k}|^{-5}$ decay of the momentum distribution for large $|\mathbf{k}|$. By contrast, $\psi_{B,\text{sq}}$ has a continuous first derivative, and its momentum distribution vanishes for $|k_x| > 2k_{F,x}$, $|k_y| > 2k_{F,y}$ ($k_{F,x}$ and $k_{F,y}$ are Fermi momenta of $\psi_{F,0}$ in x and y direction). The corresponding energy per particle is $\epsilon = 13.1 n^{4/3}$, which is considerably lower than the WC energy.

A more exotic choice is the composite-fermion wave-function considered in Ref. [26] in the context of a 2D Bose gas with Rashba SOC:

$$\psi_{B,\text{cf}} = \mathcal{N} \prod_{i < j} |z_i - z_j| \exp\left(-\sum_j |z_j|^2/4\right), \quad (6.8)$$

where $z_j = x_j/a_x + iy_j/a_y$, x_j and y_j are particle coordinates, a_x and a_y are length-scales in x and y direction, and \mathcal{N} is the normalization factor. This state has been shown to be a quasi-condensate with algebraically decaying correlations [139, 140], but it does not break time-reversal symmetry. In order to make wave-function have $\Delta k_x \sim n^{1/3}$, $\Delta k_y \sim n^{2/3}$, the lengths have to scale with density as $a_x \sim n^{-1/3}$, $a_y \sim n^{-2/3}$. Once again, the first derivative of $\psi_{B,\text{cf}}$ is not continuous at points where $\psi_{B,\text{cf}} = 0$, and this leads to $\sim |\mathbf{k}|^{-6}$ algebraic decay of the momentum distribution

for large $|\mathbf{k}|$ rendering the integral (6.7) divergent.

However, the square of $\psi_{B,\text{cf}}$ wave-function:

$$\psi_{B,\text{cf}}^{\text{sq}} = (\psi_{B,\text{cf}})^2 = \mathcal{N}' \prod_{i < j} |z_i - z_j|^2 e^{-\sum_j |z_j|^2/2} \quad (6.9)$$

is free from these problems. It is analytic and has an exponentially decaying momentum distribution for large $|\mathbf{k}|$. Subsequently, the integral (6.7) is convergent. We find that the choice of length scales which minimizes the total energy per particle is $a_x = 0.55 n^{-1/3}$, $a_y = 0.29 n^{-2/3}$, and the energy is $\epsilon = 9.2 n^{4/3}$, which is the lowest energy of all the wave-functions considered so far. This state has zero condensate fraction, and is therefore *not* a true Bose condensate. However it has algebraically decaying correlations $\rho(\mathbf{r}, \mathbf{r}') = \rho(|\mathbf{r} - \mathbf{r}'|) = \langle \hat{\psi}^\dagger(\mathbf{r}) \hat{\psi}(\mathbf{r}') \rangle \sim 1/|\mathbf{r} - \mathbf{r}'|$ as $|\mathbf{r} - \mathbf{r}'| \rightarrow \infty$, and is thus a quasi-condensate [139, 140]. We reproduced this result using our Monte Carlo approach (see Fig. 1). While it is certainly possible to consider even higher powers of $\psi_{B,\text{cf}}$, these wave-functions have higher energy as the increasing exponents broaden the momentum distribution of the state.

Note that even though we casually refer to the states $\psi_{B,\text{abs}}$, $\psi_{B,\text{sq}}$, $\psi_{B,\text{cf}}$, $\psi_{B,\text{cf}}^{\text{sq}}$, etc. as “fermionized,” the issue of fermionization is a subtle one. Strictly speaking, our ability to express a bosonic ground state wave-function in terms of properly symmetrized fermionic wave-functions does not necessarily imply that low-energy excitations of this state have fermionic statistics. To elucidate the nature of a bosonic state in two dimensions written in terms of fermionic fields (which can always be done even for trivial ground states), one has to consider a gauge theory, e.g., either arising from a parton construction or Chern-Simons flux attachment

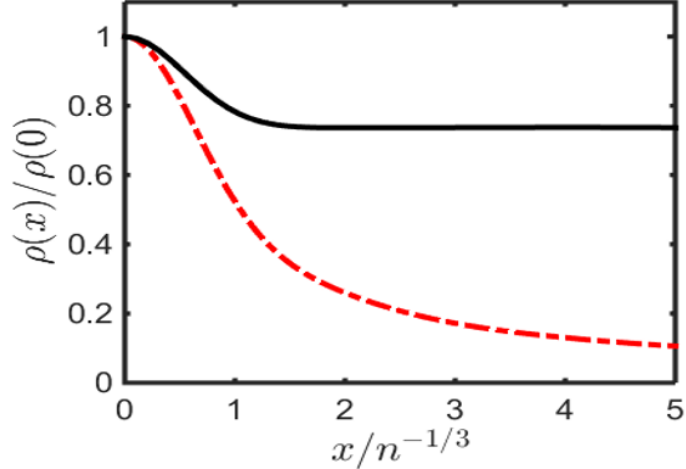


Figure 6.2: We show the correlation function $\rho(\mathbf{r})$ for two different states: (a) composite-fermion state $\psi_{B,cf}^{sq}$ (red dash-dotted line) and (b) Jastrow wave-function ψ_J (black line). Here we set $y = 0$ and concentrate at the dependence on x . $\psi_{B,cf}^{sq}$ wave-function has algebraically decaying correlations, i.e. it has a quasi-long range order, while ψ_J has a true long range order (see text for details).

(such as implemented by Sedrakyan et al. [26] for the bosonic Rashba model). On the other hand, there usually exists no simple way to write the corresponding many-body wave-function, which would faithfully describe gauge fluctuations, and those may have important and qualitative effects on conclusions of a naïve mean-field theory. For example, the many-body wave-function $\psi_{B,cf}$ is a natural mean-field description of a “fermionized” state, where fermions, obtained from original bosons via Chern-Simons flux attachment, form the integer $\nu = 1$ quantum Hall state. As discussed above, the symmetrized bosonic wave-function, $\psi_{B,cf}$, does not have a long-range order and hence appears to describe a strongly-correlated liquid state with algebraic correlations or equivalently a quasi-condensate. However, the (more general) Chern-Simons gauge-theory of the “fermionized” state yields a different

conclusion [141]: integrating out fermions produces another Chern-Simons term, which exactly cancels the term associated with statistical transmutation, and what is left is a gapless (Maxwell) theory. It corresponds to a Goldstone mode and indicates broken symmetry, or in other words a true condensate with long-range order. In fact, the state proposed by Sedrakyan et al. [26] belongs to this category and is a strongly-correlated BEC, rather than an exotic Bose liquid.

All in all, the field-theoretical approach based on true fermionization of bosonic fields and the variational approach involving “fermionized” wave-functions are not equivalent. The former provides more insight into the nature of excitations, but does not easily allow for a quantitative analysis. On the contrary, the latter can be used for explicit calculations of energy and other observables, but it does not easily elucidate the nature of low-energy excitations. One strategy here is to start with the variational approach and explore field-theoretical description, if any, of a “fermionized” mean-field state, if such indeed comes out as the lowest-energy trial state for a given Hamiltonian. This however does not seem to happen in our case, as discussed below.

6.5.2.2 Jastrow Ansatz for a strongly-correlated BEC – the winner

One advantage of using “fermionized” wave-functions to approximately describe a ground state of interacting bosons is that they immediately minimize the interaction energy for any contact interaction (for spinless bosons), by the virtue of the simple fact that two fermions can not occur in the same point. However, there

exist infinitely many wave-functions that accomplish the same, without relying on any fermionic analogy. Related constructions have been discussed in the literature, notably in the context of strongly-correlated BEC in Helium-4. Inspired by these previous studies, we now consider a Jastrow *ansatz* [136] of the following form:

$$\psi_J = \mathcal{N}'' \prod_{i<j}^N \phi(\mathbf{r}_i - \mathbf{r}_j), \quad (6.10)$$

$$\phi(\mathbf{r}) = 1 - e^{-(x^2/b_x^2 + y^2/b_y^2)},$$

where \mathcal{N}'' is the normalization, and b_x, b_y are parameters describing correlation length-scale in x and y direction. The density, $n = N/V$ is another important parameter of wave-function (6.10). Jastrow-type wave-functions are generally very good at capturing the behavior of Bose gases ranging from small to large scattering lengths, i.e. from a weakly interacting to unitary regime [142]. A key difference here is that while usually, the Jastrow form is used to capture the short distance structure of the two-body wave-function on length scales comparable to the true atomic potential, here we work in a regime where b_x and b_y are on the order of the inter particle spacing, thus much larger than the scattering length. Our ansatz is therefore phenomenological in nature, and does not stem from a microscopic calculation of the two-body problem.

As with the previously considered trial states, the Jastrow wave-function has the property that its interaction energy is zero. By choosing $b_x \sim n^{-1/3}$, $b_y \sim n^{-2/3}$ we can “squeeze” the system in the x and “stretch” it in the y direction, so that $\epsilon \sim n^{4/3}$. We find the optimal parameter values are $b_x = 0.66 n^{-1/3}$, $b_y = 0.29 n^{-2/3}$, and the energy is $\epsilon = 6.6 n^{4/3}$. The Jastrow wave-function therefore has even lower

energy than the composite-fermion wave-function $\psi_{B,cf}^{sq}$. In Fig. 6.2, we plot the single-particle density matrix $\rho(\mathbf{r}, \mathbf{r}')$ as a function of $|\mathbf{r} - \mathbf{r}'|$ corresponding to $\psi_{B,cf}^{sq}$ and the Jastrow wave-function found above. Indeed the Jastrow form has true long range order, and describes a Bose-condensate with condensate fraction $n_0/n = 0.74$.

We therefore conclude that for the spinless Hamiltonian [Eq.(6.5)], although bosons can lower their energy by developing short range correlations, the correlations are not strong enough to completely destroy BEC at zero temperature.

The *ansatz* wave-functions that we considered all have the property that $\psi = 0$ when $\mathbf{r}_i = \mathbf{r}_j$ which means $E_{\text{int}} = 0$. While this should be true in the $n \rightarrow 0$ limit, at finite densities we expect the interaction energy not to be strictly zero. In Appendix B, we estimate that for small densities $E_{\text{int}}/N \sim n^{5/3}/g$, which means that $E_{\text{int}}/E_{\text{kin}} \sim n^{1/3}$. Therefore, as in the Lieb-Liniger gas [143], at low densities $E_{\text{int}} \ll E_{\text{kin}}$.

6.5.3 Spinful system

We now turn our attention to the spinful Hamiltonian (6.1) which corresponds to the NIST SOC scheme, and ask whether our conclusions remain valid in this case.

We start by writing the spinful state $|\psi_{B,s}\rangle$ as:

$$|\psi_{B,s}\rangle = \sum_{\mathbf{k}_1 \dots \mathbf{k}_N} f_B(\mathbf{k}_1, \dots, \mathbf{k}_N) |\mathbf{k}_1 \dots \mathbf{k}_N\rangle_s, \quad (6.11)$$

where

$$f_B(\mathbf{k}_1, \dots, \mathbf{k}_N) = \frac{1}{V^N} \int d\mathbf{r}_1 \dots d\mathbf{r}_N \psi_B(\mathbf{r}_1, \dots, \mathbf{r}_N) \times e^{-i(\mathbf{k}_1 \cdot \mathbf{r}_1 + \dots + \mathbf{k}_N \cdot \mathbf{r}_N)}, \quad (6.12)$$

is the Fourier transform of the spinless wave-functions ψ_B considered above. Here $|\mathbf{k}_1 \dots \mathbf{k}_N\rangle_s = |\mathbf{k}_1\rangle_s \otimes \dots \otimes |\mathbf{k}_N\rangle_s$, where $|\mathbf{k}\rangle_s$ is a *lower-band* eigenstate of (6.1). We therefore *construct* a spinful state exclusively from lower-band eigenstates. A similar construction was applied in Ref. [26].

At low densities, the lower-band spectrum of the spinful Hamiltonian is the same as the spinless dispersion (6.5). Since, by construction, the spinful state [Eq.(6.11)] has the same momentum distribution as the corresponding spinless state, their kinetic energy is the same (see Appendix D).

However, the more complicated question is: what is the interaction energy of the spinful state? Since we explicitly construct the spinful many-body state only from the lower-band single-particle states, it is impossible to satisfy $\psi(\dots, \mathbf{r}_i = \mathbf{r}_j, \dots) = 0, \forall(i, j)$, for all the different spin components $\psi_{\sigma_1, \dots, \sigma_N}(\mathbf{r}_1, \dots, \mathbf{r}_N)$ [$\sigma_j \in (\uparrow, \downarrow)$]. Therefore, unlike in the spinless wave-functions considered previously, the interaction energy will be finite. Still, in the low-density limit, we expect the zero overlap condition ($\psi = 0$ when $\mathbf{r}_i = \mathbf{r}_j$) to be *almost* satisfied, since the system is almost completely polarized. We thus expect the spinful state to have a very low interaction energy.

The interaction Hamiltonian (6.3) is diagonal in real space, and to calculate the interaction energy it is useful to find a real-space representation of $|\psi_{B,s}\rangle$. Unfortunately, the real-space representation is quite cumbersome: there are 2^N spin components (although only $N + 1$ of them are independent due to the symmetric

nature of f_B), and expressions are difficult to obtain:

$$\begin{aligned} \psi_{\sigma_1, \dots, \sigma_N}(\mathbf{r}_1, \dots, \mathbf{r}_N) &= \sum_{\mathbf{k}_1, \dots, \mathbf{k}_N} f_B(\mathbf{k}_1, \dots, \mathbf{k}_N) \\ &\times s_{\sigma_1}(\mathbf{k}_1) \dots s_{\sigma_N}(\mathbf{k}_N) e^{i(\mathbf{k}_1 \cdot \mathbf{r}_1 + \dots + \mathbf{k}_N \cdot \mathbf{r}_N)}, \end{aligned} \quad (6.13)$$

where $s_{\sigma_j}(\mathbf{k})$ are given in (6.4).

In Appendix E we present the method to estimate the interaction energy, and we show that for wave-functions $\psi_{B,\text{sq}}$, $\psi_{B,\text{cf}}^{\text{sq}}$, and the Jastrow wave-function the energy is $E_{\text{int}}/N \sim n^{7/3}$ at low densities. Therefore, $E_{\text{int}}/E_{\text{kin}} \rightarrow 0$ when $n \rightarrow 0$ and $E_{\text{tot}}/N = (E_{\text{kin}} + E_{\text{int}})/N \rightarrow 6.6 n^{4/3}$ for the Jastrow state.

It is important to assess the validity of constructing the spinful state only from lower-band eigenstates: we have already shown that the ground state energy cannot be greater than $\epsilon \sim n^{4/3}$. If there was a finite fraction u of particles occupying the higher band as $n \rightarrow 0$, then the energy would be $E/N \sim u\Delta$, where Δ is the gap between the two bands. However, this clearly contradicts the fact that $E/N \lesssim n^{4/3}$. Therefore, $u \rightarrow 0$ as $n \rightarrow 0$ and the $n \rightarrow 0$ ground state will only contain states from the lower band.

6.6 Discussion and experimental relevance

In this chapter, we considered a system of interacting bosons with a quartic single-particle dispersion. It was shown that the low-density limit of the model hosts a strongly-correlated ground state, where the mean-field Bogoliubov state can be easily ruled out as being parametrically higher in energy than the strongly-correlated states, where bosons develop local correlations and avoid each other.

Wave-function	ϵ	Section
Mean-field BEC	$gn/2$	6.3
Wigner crystal	$43.5 n^{4/3}$	6.4
Absolute value of Fermi-sea w.f.	∞	6.5.2.1
Fermi-sea w.f. squared	$13.1 n^{4/3}$	6.5.2.1
Composite-fermion w.f.	∞	6.5.2.1
Composite-fermion w.f. squared	$9.2 n^{4/3}$	6.5.2.1
Jastrow state	$6.6 n^{4/3}$	6.5.2.2

Table 6.1: Energy per particle (ϵ) of different states in the low-density limit (n and g are dimensionless density and interaction strength, respectively). Of all the wave-functions (w.f.) we consider, the Jastrow state has the lowest energy. Two wave-functions (absolute value of Fermi-sea w.f. and composite-fermion w.f.) have diverging expectation value of k_x^4 (see text for details).

Among the many trial states we considered, a long-range-ordered condensate described by the Jastrow wave-function [Eq.(6.10)] was found to have the lowest energy per particle of $\epsilon = 6.6 n^{4/3}$ (compared to $\epsilon = gn/2$ for a mean-field BEC). This is in agreement with Ref. [134] where it was argued that the ground state of system (6.5) has long-range order. The condensate fraction was found to be $N_0/N = 0.74$. *i.e.*, it is a strongly-correlated BEC with significant depletion of the condensate due to the interplay between interactions and the unusual band structure.

Importantly, the mean-field BEC and the Jastrow BEC break the same symmetry, therefore, we expect that the system continuously evolves from a weakly to a strongly-correlated BEC state from high to low-densities, without any phase transitions in between (a similar weak-to-strong-coupling cross-over can be tuned by evolving the single-particle dispersion from the usual quadratic to quartic).

Note however that in the absence of a systematic procedure to explore many-

body ground states of strongly-correlated systems, our variational-approach results are strongly suggestive, but not conclusive. Eventually, it is experiment that would fully elucidate the nature of the ground state, and to realize our model is at the experimentalists' fingertips.

The strongly-correlated condensate we predict can be detected experimentally using a number of probes. For example, the suppressed condensate fraction is measurable in time-of-flight [13]. Another signature of strong correlations is the ratio of interaction and kinetic energy which is very small at low densities. This could be accessed via quantum quench experiments, i.e. the interaction parameter g could be suddenly changed and the effect on the total energy of the gas could be measured. Strong local correlations can also be measured *in situ* by observing the anti-bunching of bosonic atoms [144]. Finally, several groups [145, 146] have directly measured $\rho(\mathbf{r}, \mathbf{r}')$. This would give information about the condensate fraction, and the type of order present in the gas.

We can estimate the density below which strong correlations become energetically favourable by equating mean-field-BEC and Jastrow-state energies (see Table 6.1). In the case of ^{87}Rb with a z -direction confinement frequency $\omega_z = 2\pi \times 4000$ Hz, this gives $n \approx 10^{-6} k_L^2 \approx 6 \times 10^7 \text{ m}^{-2}$ ($k_L = 2\pi/\lambda$, where $\lambda \approx 800$ nm [147]), which is much lower than typical densities in cold-atom experiments studying 2D systems ($n \sim 10^{13} \text{ m}^{-2}$ [148]). However, using Feshbach resonances to increase g , it is possible to make strong correlations favourable at considerably higher densities, up to $n \approx 0.004 k_L^2 \approx 2 \times 10^{11} \text{ m}^{-2}$, which could be achieved experimentally. At densities higher than this the dispersion in x -direction cannot be approximated by a quartic

term anymore, and higher-order terms have to be included.

Chapter 7: Conclusion

In the last couple of years, significant progress has been made in creating synthetic gauge fields for ultracold atoms. As of today, there has been several experiments realizing synthetic magnetic field and spin-orbit coupling, in addition to the large number of theoretical proposals. The excitement about the subject is primarily due to prospects of realizing exotic strongly correlated and topological states, like fractional quantum Hall states, topological superfluidity, Majorana fermions, etc., therefore mirroring similar trends in condensed matter physics. There are however many other, possibly less exotic, but still very interesting phenomena that require better understanding, for example the effects of spin-orbit coupling on Bose-Einstein condensation, vortices, optical lattice physics, etc. Precisely with that purpose, in this dissertation we studied spin-orbit-coupled cold-atom systems in various different contexts. Our goal was both to provide experimentalists with guidance on what they can expect in experiments, and to study genuinely interesting theoretical questions. The projects included in the dissertation all study different topics, using different theoretical approaches and tools, however all with the underlying theme of *spin-orbit coupling*. In the following I summarize our findings.

In the first part of the dissertation we investigated realistic experimental meth-

ods for creation of vortex excitations in spin-orbit-coupled BECs. The main conclusions are: (a) rotation can be used to create static vortex structures only if both the trapping potential and SOC-generating lasers are rotated simultaneously; (b) introducing spatially-dependent detuning is an alternative to rotation, as it leads to an effective magnetic field which favours creation of vortices. By performing numerical simulations for different parameters of a realistic experimental setup [7], we predict a variety of vortex structures that could be straightforwardly observed in future experiments.

In our second work we studied the effective spin models in the Mott-insulating regime of spin-orbit-coupled gases in optical lattices. We derived the tight-binding model and we obtained the effective low-energy Hamiltonian which takes the form of an exotic spin model with Heisenberg, compass-model and Dzyaloshinskii-Moriya interaction. We determined the zero-temperature classical phase diagram for the model and showed that the interplay between the different interactions leads to a large variety of phases: ferromagnet, spirals, stripes, three-dimensional vortex and antivortex phases.

In the third part of the dissertation we considered time evolution of the magnetization in a Rashba spin-orbit-coupled Fermi gas, starting from a fully-polarized initial state. We modeled the dynamics using a collisionless Boltzmann equation, and we have shown that out-of-equilibrium dynamics of quantum spins in an otherwise classical gas leads to non-trivial steady states and associated dynamical transitions. We have found three distinctive regimes with transitions between them controlled by the ratio of the interaction and SOC strength. The steady states we describe

are far from thermal equilibrium, and their stability relies on the absence of collisions which can be controlled in cold-atom experiments by tuning the interaction strength.

In the work on the bosonic analog of Stoner transition we have established a finite-temperature phase diagram (temperatures above the superfluid transition temperature) of a pseudospin-1/2 Bose gas with contact interactions, using two complementary methods: the random phase approximation (RPA) and the self-consistent Hartree-Fock theory. We have found two normal, stable itinerant ferromagnetic phases, where magnetic order occurs without superfluidity, and concluded that a bosonic analogue of the Cooper paired phase (for attractive inter-species interactions) is not energetically favourable. Extending our calculations to a spin-orbit-coupled Bose gas, we investigated the possibility of stripe ordering in the normal phase. However, we have not found an instability towards stripe formation, suggesting that the stripe order melts below the condensation temperature, which is consistent with the experimental observations of Ji *et al.* [23].

In the final work, we considered a system of interacting bosons with a quartic single-particle dispersion. It was shown that the low-density limit of the model hosts a strongly-correlated ground state, while the mean-field Bogoliubov state can be easily ruled out as being parametrically higher in energy. Among the many trial states we considered, a long-range-ordered and strongly-correlated condensate described by the Jastrow wave-function [136] was found to have the lowest energy per particle, in agreement with Ref. [134]. We stress that due to the nature of our variational approach, our results are strongly suggestive, but not conclusive.

Appendix A: Rotation of a trap and/or spin-orbit lasers: derivations

A.1 M-scheme with rotating trap and spin-orbit lasers

The M-scheme Hamiltonian in the rotating frame is [see Eq.(2.6)]:

$$\hat{H}_{RF} = \left[\frac{\hbar^2 \hat{\mathbf{k}}^2}{2m} + V(\mathbf{r}) - \omega_r \hat{L}_z \right] \check{\mathbb{1}} + \begin{pmatrix} \hbar(-\omega_z + \omega_q) & 0 & 0 \\ 0 & 0 & 0 \\ 0 & 0 & \hbar\omega_z \end{pmatrix} \quad (\text{A.1})$$

$$+ \sqrt{2}\Omega \check{\sigma}_{3,x} \cos(2k_L x + \Delta\omega_L t) - \omega_r \check{\sigma}_{3,z}.$$

The remaining time dependence coming from Raman lasers can be removed if we transfer to the *rotating-wave* frame (different from the rotating frame) and if we do the rotating-wave approximation:

$$\hat{H}_{RF} = \left[\frac{\hbar^2 \hat{\mathbf{k}}^2}{2m} + V(\mathbf{r}) - \omega_r \hat{L}_z \right] \check{\mathbb{1}} + \begin{pmatrix} \delta + \hbar\omega_q & 0 & 0 \\ 0 & 0 & 0 \\ 0 & 0 & -\delta \end{pmatrix} \quad (\text{A.2})$$

$$+ \frac{\Omega}{\sqrt{2}} \check{\sigma}_{3,x} \cos(2k_L x) - \frac{\Omega}{\sqrt{2}} \check{\sigma}_{3,y} \sin(2k_L x) - \hbar\omega_r \check{\sigma}_{3,z},$$

where $\delta = \hbar(\Delta\omega_L - \omega_z)$. We set quadratic Zeeman shift $\hbar\omega_q$ to be much greater than Ω and δ so we may restrict to the subspace spanned by $\{|m_z = 0\rangle, |m_z = -1\rangle\}$:

$$\begin{aligned} \hat{H}_{RF,2} = & \left[\frac{\hbar^2 \hat{\mathbf{k}}^2}{2m} + V(\mathbf{r}) - \omega_r \hat{L}_z \right] \check{1} + \frac{\Omega}{2} \check{\sigma}_x \cos(2k_L x) \\ & - \frac{\Omega}{2} \check{\sigma}_y \sin(2k_L x) + \begin{pmatrix} 0 & 0 \\ 0 & \hbar\omega_r - \delta \end{pmatrix}, \end{aligned} \quad (\text{A.3})$$

where $\check{1}$ is 2×2 unit matrix and $\check{\sigma}_{x,y,z}$ are 2×2 Pauli matrices. Since there are effectively two internal degrees of freedom we introduce pseudospin-1/2 notation, i.e. we define $|\uparrow\rangle \equiv |m_z = 0\rangle$, $|\downarrow\rangle \equiv |m_z = -1\rangle$. We follow the steps in [7] and make transformation: $\psi'_\uparrow(\mathbf{r}) = \psi_\uparrow(\mathbf{r})e^{-ik_L x}$, $\psi'_\downarrow(\mathbf{r}) = \psi_\downarrow(\mathbf{r})e^{ik_L x}$, where $(\psi_\uparrow(\mathbf{r}), \psi_\downarrow(\mathbf{r}))$ is a spinor wavefunction on which Hamiltonian (A.3) acts. The Hamiltonian then becomes:

$$\begin{aligned} \hat{H}_{RF,2} = & \left[\frac{\hbar^2 \hat{\mathbf{k}}^2}{2m} + V(\mathbf{r}) - \omega_r \hat{L}_z + E_L \right] \check{1} \\ & + \frac{\hbar^2 k_L \hat{k}_x}{m} \check{\sigma}_z + \frac{\Omega}{2} \check{\sigma}_x + \hbar\omega_r k_L y \check{\sigma}_z + \begin{pmatrix} 0 & 0 \\ 0 & \hbar\omega_r - \delta \end{pmatrix}, \end{aligned} \quad (\text{A.4})$$

where $E_L = \hbar^2 k_L^2 / 2m$. We can drop $E_L \check{1}$ term by simply renormalizing the energy.

A.2 M-scheme with rotating trap

The Hamiltonian H'_{rot} describing M-scheme with rotating trap in the laboratory frame is:

$$\hat{H}' = \left[\frac{\hbar^2 \hat{\mathbf{k}}^2}{2m} + V(x(t), y(t), z) - \omega_r \hat{L}_z \right] \check{1} + \begin{pmatrix} \hbar(-\omega_z + \omega_q) & 0 & 0 \\ 0 & 0 & 0 \\ 0 & 0 & \hbar\omega_z \end{pmatrix} \quad (\text{A.5})$$

$$+ \sqrt{2}\Omega \check{\sigma}_{3,x} \cos(2k_L x + \Delta\omega_L t),$$

where $x(t)$ is defined in (2.3). After transferring to the rotating frame ($\hat{U}(t) = \exp[i\omega_r t(\hat{L}_z + \hat{S}_z)/\hbar]$) and making the rotating wave approximation the Hamiltonian is:

$$\hat{H}'_{RF} = \left[\frac{\hbar^2 \hat{\mathbf{k}}^2}{2m} + V(\mathbf{r}) - \omega_r \hat{L}_z \right] \check{1} - \hbar\omega_r \check{\sigma}_{3,z} + \begin{pmatrix} 3\delta/2 + \hbar\omega_q & 0 & 0 \\ 0 & \delta/2 & 0 \\ 0 & 0 & -\delta/2 \end{pmatrix} \quad (\text{A.6})$$

$$+ \frac{\Omega}{\sqrt{2}} \check{\sigma}_{3,x} \cos(2k_L x'(t) + \omega_r t) - \frac{\Omega}{\sqrt{2}} \check{\sigma}_{3,y} \sin(2k_L x'(t) + \omega_r t),$$

where $x'(t) = x \cos(\omega_r t) - y \sin(\omega_r t)$. We may again neglect state $|m_z = 1\rangle$ assuming $\omega_q \gg \delta$. To get the Hamiltonian in a more familiar spin-orbit-coupling form we make the following transformation: $\psi'_\uparrow(\mathbf{r}) = \psi_\uparrow(\mathbf{r})e^{-ik_L x'(t)}$, $\psi'_\downarrow(\mathbf{r}) = \psi_\downarrow(\mathbf{r})e^{ik_L x'(t) + i\omega_r t}$, which gives:

$$\hat{H}'_{RF,2} = \left[\frac{\hbar^2 \hat{\mathbf{k}}^2}{2m} + V(\mathbf{r}) - \omega_r \hat{L}_z + E_L \right] \check{1} + \frac{\hbar^2 k_L}{m} \hat{k}_x(t) \check{\sigma}_z + \frac{\Omega}{2} \check{\sigma}_x + \frac{\delta}{2} \check{\sigma}_z, \quad (\text{A.7})$$

where $\hat{k}_x(t) = \hat{k}_x \cos(\omega_r t) - \hat{k}_y \sin(\omega_r t)$. We can drop $E_L \check{1}$ term by renormalizing the energy.

A.3 Tripod scheme with rotating trap and spin-orbit lasers

The original Hamiltonian for the tripod scheme (stationary system) is (see [18]):

$$\hat{H}_0 = \frac{\hbar^2 \hat{\mathbf{k}}^2}{2m} \check{1} + \hat{V}(\mathbf{r}) + \hat{H}_{a-l}, \quad (\text{A.8})$$

where $\hat{V}(\mathbf{r}) = \sum_j V_j(\mathbf{r})|j\rangle\langle j|$ is spin dependent trapping potential, atom-laser interaction $\hat{H}_{a-l} = \Delta|0\rangle\langle 0| - (\Omega_1|0\rangle\langle 1| + \Omega_2|0\rangle\langle 2| + \Omega_3|0\rangle\langle 3| + \text{H.c.})$ and $\check{1}$ is 4×4 unit matrix. Δ is detuning from resonance and $\Omega_{1,2,3}$ are Rabi frequencies: $\Omega_1(\mathbf{r}) = \Omega \sin \theta \cos(mv_a x) e^{imv_b y}$, $\Omega_2(\mathbf{r}) = \Omega \sin \theta \sin(mv_a x) e^{imv_b y}$, $\Omega_3(\mathbf{r}) = \Omega \cos \theta$, where Ω , θ , v_a and v_b are constants (see [18] for details). If we start rotating spin-orbit lasers in the laboratory, atom-laser interaction part of the Hamiltonian becomes $e^{-i\omega_r t(\hat{L}_z + \hat{S}_z)/\hbar} \hat{H}_{a-l} e^{i\omega_r t(\hat{L}_z + \hat{S}_z)/\hbar}$. If the trap rotates, trapping potential becomes $e^{-i\omega_r t(\hat{L}_z + \hat{S}_z)/\hbar} \hat{V} e^{i\omega_r t(\hat{L}_z + \hat{S}_z)/\hbar}$. Therefore, we can write the Hamiltonian of the rotating system as:

$$\hat{H}_{\text{rot}} = e^{-i\omega_r t(\hat{L}_z + \hat{S}_z)/\hbar} \hat{H}_0 e^{i\omega_r t(\hat{L}_z + \hat{S}_z)/\hbar}. \quad (\text{A.9})$$

The Hamiltonian in the rotating frame is then: $\hat{H}_{RF} = \hat{H}_0 - \omega_r(\hat{L}_z + \hat{S}_z)$. Since \hat{H}_{RF} is time-independent, we can use exactly the same procedure for getting the effective spin-orbit coupling described in [17, 18], i.e. we project the Hamiltonian to the dark states subspace. Here we assume that three degenerate hyperfine groundstates are part of F=1 manifold (for example the ground state of ^{87}Rb) and that they are eigenstates of \hat{S}_z . This gives us the precise form of \hat{S}_z operator. As in [18] we choose

$V_1 = V_2 = w(\mathbf{r})$ and $V_3 = w(\mathbf{r}) + \delta$. After projecting to dark states we get:

$$\hat{H}_{RF,2} = \left[\frac{\hat{\mathbf{p}}^2}{2m} + w(\mathbf{r}) - \omega_r \hat{L}_z \right] \check{1} - v_0 \hat{p}_x \check{\sigma}_y - v_1 \hat{p}_y \check{\sigma}_z + \delta_0 \check{\sigma}_z + m\hbar\omega_r(v_1 x \check{\sigma}_z - v_0 y \check{\sigma}_y) - \hbar\omega_r \begin{pmatrix} \sin^2 \phi & \sin \phi \cos \phi \cos \theta \\ \sin \phi \cos \phi \cos \theta & \cos^2 \theta \cos^2 \phi - \sin^2 \theta \end{pmatrix}, \quad (\text{A.10})$$

where $\delta_0 = \sin^2 \theta \{ \delta - [(\frac{v_0}{\cos \theta})^2 + (\frac{v_1}{\sin^2(\theta/2)})^2] / 2 \} / 2$.

Appendix B: Finding maximally localized Wannier states

Let $|\psi_{\mathbf{k},m}\rangle$ be the eigenstates (Bloch states) of the periodic Hamiltonian defined in Eq.(3.1). Wannier states are then defined as

$$|\mathbf{R}, j\rangle = \frac{1}{N_t} \sum_{\mathbf{k},m} e^{-i\mathbf{k}\cdot\mathbf{R}} U_{j,m}(\mathbf{k}) |\psi_{\mathbf{k},m}\rangle, \quad (\text{B.1})$$

where $|\mathbf{R}, j\rangle$ is Wannier state corresponding to a lattice site \mathbf{R} , and $j \in \{1, 2\}$ is the Wannier state index. N_t is the number of lattice sites, and $U_{j,m}(\mathbf{k})$ is any 2×2 unitary matrix which has the role of mixing Bloch states from the two lowest-energy bands (the two bands are degenerate in the absence of SOC). This is necessary because it is not possible to construct *localized* Wannier states using Bloch states from each band separately [61].

Wannier states defined in Eq.(B.1) are not localized for an arbitrary choice of $U(\mathbf{k})$ and the goal is to find $U(\mathbf{k})$ for which Wannier states are *maximally localized* [61, 149] (implying exponentially decaying tails). Therefore, following Ref. [61] we define a spread-functional Ω which characterizes the degree of Wannier-state localization:

$$\Omega = \sum_{j=1}^2 \langle \mathbf{0}, j | \mathbf{r}^2 | \mathbf{0}, j \rangle, \quad (\text{B.2})$$

where, without loss of generality, we concentrate on the $\mathbf{R} = \mathbf{0}$ lattice site (this is possible since Wannier states at other sites can be obtained by simple translation

of the $\mathbf{R} = \mathbf{0}$ state). It can be shown that

$$\Omega = \sum_{\mathbf{k}, \mathbf{q}} \text{Tr} [U(\mathbf{q})M(\mathbf{q}, \mathbf{k})U^\dagger(\mathbf{k})],$$

$$M_{mn}(\mathbf{q}, \mathbf{k}) = \frac{1}{N_t} \langle \psi_{\mathbf{k}, n} | \mathbf{r}^2 | \psi_{\mathbf{q}, m} \rangle. \quad (\text{B.3})$$

Here $M(\mathbf{q}, \mathbf{k})$ can be evaluated numerically for a finite lattice with periodic boundary conditions (in our calculations we considered lattices with up to $N_t = 81$ sites).

However, we have to find matrices $U(\mathbf{k})$ which minimize Ω and we do it by using the steepest descent method. That is, if $f(\boldsymbol{\lambda})$ is a functional that has to be minimized, this can (often) be done by changing the parameters $\boldsymbol{\lambda}$ in the direction where the change of f the greatest:

$$d\boldsymbol{\lambda} = -(\nabla f) dt. \quad (\text{B.4})$$

In order to find $\nabla \Omega$, we first notice that unitary operator $U(\mathbf{k})$ can be written as $U = \exp(W)$, where W is an antihermitian operator ($W^\dagger = -W$):

$$W = \begin{pmatrix} i\alpha & -\beta + i\gamma \\ \beta + i\gamma & i\delta \end{pmatrix}, \quad \alpha, \beta, \gamma, \delta \in \mathbb{R}. \quad (\text{B.5})$$

Let us now define:

$$\tilde{M}(\mathbf{q}, \mathbf{k}) = U(\mathbf{q})M(\mathbf{q}, \mathbf{k})U^\dagger(\mathbf{k}). \quad (\text{B.6})$$

If we make an infinitesimal change of U :

$$U'(\mathbf{k}) = \exp[W(\mathbf{k})] U(\mathbf{k}) = [\mathbb{1} + W(\mathbf{k}) + \dots] U(\mathbf{k})$$

$$\approx \begin{pmatrix} 1 + i\alpha_{\mathbf{k}} & -\beta_{\mathbf{k}} + i\gamma_{\mathbf{k}} \\ \beta_{\mathbf{k}} + i\gamma_{\mathbf{k}} & 1 + i\delta_{\mathbf{k}} \end{pmatrix} U, \quad (\text{B.7})$$

where $\alpha_{\mathbf{k}}, \beta_{\mathbf{k}}, \gamma_{\mathbf{k}}, \delta_{\mathbf{k}} \ll 1$, Ω' becomes $\Omega' = \sum_{\mathbf{k}, \mathbf{q}} Tr\{\exp[W(\mathbf{q})]\tilde{M}(\mathbf{q}, \mathbf{k}) \exp[W(\mathbf{k})]^\dagger\}$.

By expanding Ω' to the first order in $\alpha_{\mathbf{k}}, \beta_{\mathbf{k}}, \gamma_{\mathbf{k}}, \delta_{\mathbf{k}}$, it is straightforward to calculate the gradient of Ω :

$$\begin{aligned}
\frac{\partial \Omega}{\partial \alpha_{\mathbf{k}}} &= i \sum_{\mathbf{q}} \left[\tilde{M}_{11}(\mathbf{k}, \mathbf{q}) - \tilde{M}_{11}(\mathbf{q}, \mathbf{k}) \right] \\
\frac{\partial \Omega}{\partial \beta_{\mathbf{k}}} &= \sum_{\mathbf{q}} \left[\tilde{M}_{21}(\mathbf{q}, \mathbf{k}) - \tilde{M}_{12}(\mathbf{q}, \mathbf{k}) + \tilde{M}_{12}(\mathbf{k}, \mathbf{q}) - \tilde{M}_{21}(\mathbf{k}, \mathbf{q}) \right] \\
\frac{\partial \Omega}{\partial \gamma_{\mathbf{k}}} &= i \sum_{\mathbf{q}} \left[-\tilde{M}_{21}(\mathbf{q}, \mathbf{k}) - \tilde{M}_{12}(\mathbf{q}, \mathbf{k}) + \tilde{M}_{12}(\mathbf{k}, \mathbf{q}) + \tilde{M}_{21}(\mathbf{k}, \mathbf{q}) \right] \\
\frac{\partial \Omega}{\partial \delta_{\mathbf{k}}} &= i \sum_{\mathbf{q}} \left[\tilde{M}_{22}(\mathbf{k}, \mathbf{q}) - \tilde{M}_{22}(\mathbf{q}, \mathbf{k}) \right].
\end{aligned} \tag{B.8}$$

The numerical procedure is implemented as follows: (a) we first calculate gradient of Ω using matrix $\tilde{M}(\mathbf{q}, \mathbf{k})$, (b) we modify U by a small amount, by choosing parameters $\alpha_{\mathbf{k}}, \beta_{\mathbf{k}}, \gamma_{\mathbf{k}}, \delta_{\mathbf{k}}$ in the direction opposite to the gradient of Ω :

$$\alpha_{\mathbf{k}} = -\frac{\partial \Omega}{\partial \alpha_{\mathbf{k}}} \Delta t, \quad \beta_{\mathbf{k}} = -\frac{\partial \Omega}{\partial \beta_{\mathbf{k}}} \Delta t, \quad \gamma_{\mathbf{k}} = -\frac{\partial \Omega}{\partial \gamma_{\mathbf{k}}} \Delta t, \quad \delta_{\mathbf{k}} = -\frac{\partial \Omega}{\partial \delta_{\mathbf{k}}} \Delta t, \tag{B.9}$$

where the step $\Delta t \ll 1$. (c) we update \tilde{M} :

$$\tilde{M}(\mathbf{q}, \mathbf{k}) \rightarrow \exp[W(\mathbf{q})] \tilde{M}(\mathbf{q}, \mathbf{k}) \exp[W(\mathbf{k})]^\dagger. \tag{B.10}$$

We continue repeating the procedure until Ω converges to a minimum, signifying the maximally-localized Wannier states have been obtained.

Appendix C: Derivation of the collisionless Boltzmann equation

Here we derive the collisionless Boltzmann equation for spin-1/2 Fermi gas with Rashba SOC. We start from the Hamiltonian of the system written in the field-theory language:

$$\hat{H} = \int d\mathbf{r} \left\{ \begin{pmatrix} \hat{\psi}_\uparrow^\dagger(\mathbf{r}) & \hat{\psi}_\downarrow^\dagger(\mathbf{r}) \end{pmatrix} \left[-\frac{\nabla^2}{2m} + U(\mathbf{r}) - i(\alpha_x \sigma_x \partial_x + \alpha_y \sigma_y \partial_y) \right] \begin{pmatrix} \hat{\psi}_\uparrow(\mathbf{r}) \\ \hat{\psi}_\downarrow(\mathbf{r}) \end{pmatrix} + g \hat{\psi}_\uparrow^\dagger(\mathbf{r}) \hat{\psi}_\downarrow^\dagger(\mathbf{r}) \hat{\psi}_\downarrow(\mathbf{r}) \hat{\psi}_\uparrow(\mathbf{r}) \right\}. \quad (\text{C.1})$$

Via Heisenberg equation, $d\hat{A}/dt = (i/\hbar) [\hat{H}, \hat{A}]$, we obtain time-evolution equations for the field operators:

$$\begin{aligned} \left[i \frac{\partial}{\partial t_1} + \frac{\nabla_1^2}{2m} - U(\mathbf{r}_1) + i(\alpha_x \sigma_x \partial_x + \alpha_y \sigma_y \partial_y) \right] \begin{pmatrix} \hat{\psi}_\uparrow(\mathbf{r}_1) \\ \hat{\psi}_\downarrow(\mathbf{r}_1) \end{pmatrix} \\ - g \begin{pmatrix} \hat{\psi}_\uparrow(\mathbf{r}_1) \hat{\psi}_\downarrow^\dagger(\mathbf{r}_1) \hat{\psi}_\downarrow(\mathbf{r}_1) \\ \hat{\psi}_\downarrow(\mathbf{r}_1) \hat{\psi}_\uparrow^\dagger(\mathbf{r}_1) \hat{\psi}_\uparrow(\mathbf{r}_1) \end{pmatrix} = 0. \quad (\text{C.2}) \end{aligned}$$

$$\left[i \frac{\partial}{\partial t_2} - \frac{\nabla_2^2}{2m} + U(\mathbf{r}_2) + i(\alpha_x \sigma_x \partial_x + \alpha_y \sigma_y \partial_y) \right] \begin{pmatrix} \hat{\psi}_\uparrow^\dagger(\mathbf{r}_2) \\ \hat{\psi}_\downarrow^\dagger(\mathbf{r}_2) \end{pmatrix} + g \begin{pmatrix} \hat{\psi}_\downarrow^\dagger(\mathbf{r}_2) \hat{\psi}_\downarrow(\mathbf{r}_2) \hat{\psi}_\uparrow^\dagger(\mathbf{r}_2) \\ \hat{\psi}_\uparrow^\dagger(\mathbf{r}_2) \hat{\psi}_\uparrow(\mathbf{r}_2) \hat{\psi}_\downarrow^\dagger(\mathbf{r}_2) \end{pmatrix} = 0. \quad (\text{C.3})$$

We now multiply Eq.(C.2) with $\hat{\psi}_\uparrow^\dagger(\mathbf{r}_2)$ and $\hat{\psi}_\downarrow^\dagger(\mathbf{r}_2)$ from the left and Eq.(C.3) with $\hat{\psi}_\uparrow(\mathbf{r}_1)$ and $\hat{\psi}_\downarrow(\mathbf{r}_1)$ from the right. After taking the expectation value, the equations are

$$\left[i \frac{\partial}{\partial t_1} + \frac{\nabla_1^2}{2m} - U(\mathbf{r}_1) + i(\alpha_x \sigma_x \partial_{x_1} + \alpha_y \sigma_y \partial_{y_1}) \right] \begin{pmatrix} \langle \hat{\psi}_\uparrow^\dagger(\mathbf{r}_2) \hat{\psi}_\uparrow(\mathbf{r}_1) \rangle & \langle \hat{\psi}_\downarrow^\dagger(\mathbf{r}_2) \hat{\psi}_\uparrow(\mathbf{r}_1) \rangle \\ \langle \hat{\psi}_\uparrow^\dagger(\mathbf{r}_2) \hat{\psi}_\downarrow(\mathbf{r}_1) \rangle & \langle \hat{\psi}_\downarrow^\dagger(\mathbf{r}_2) \hat{\psi}_\downarrow(\mathbf{r}_1) \rangle \end{pmatrix} - g \begin{pmatrix} \langle \hat{\psi}_\uparrow^\dagger(\mathbf{r}_2) \hat{\psi}_\uparrow(\mathbf{r}_1) \hat{\psi}_\downarrow^\dagger(\mathbf{r}_1) \hat{\psi}_\downarrow(\mathbf{r}_1) \rangle & \langle \hat{\psi}_\downarrow^\dagger(\mathbf{r}_2) \hat{\psi}_\uparrow(\mathbf{r}_1) \hat{\psi}_\downarrow^\dagger(\mathbf{r}_1) \hat{\psi}_\downarrow(\mathbf{r}_1) \rangle \\ \langle \hat{\psi}_\uparrow^\dagger(\mathbf{r}_2) \hat{\psi}_\downarrow(\mathbf{r}_1) \hat{\psi}_\uparrow^\dagger(\mathbf{r}_1) \hat{\psi}_\uparrow(\mathbf{r}_1) \rangle & \langle \hat{\psi}_\downarrow^\dagger(\mathbf{r}_2) \hat{\psi}_\downarrow(\mathbf{r}_1) \hat{\psi}_\uparrow^\dagger(\mathbf{r}_1) \hat{\psi}_\uparrow(\mathbf{r}_1) \rangle \end{pmatrix} = 0 \quad (\text{C.4})$$

$$\left[i \frac{\partial}{\partial t_2} - \frac{\nabla_2^2}{2m} + U(\mathbf{r}_2) + i(\alpha_x \sigma_x \partial_{x_2} + \alpha_y \sigma_y \partial_{y_2}) \right] \begin{pmatrix} \langle \hat{\psi}_\uparrow^\dagger(\mathbf{r}_2) \hat{\psi}_\uparrow(\mathbf{r}_1) \rangle & \langle \hat{\psi}_\uparrow^\dagger(\mathbf{r}_2) \hat{\psi}_\downarrow(\mathbf{r}_1) \rangle \\ \langle \hat{\psi}_\downarrow^\dagger(\mathbf{r}_2) \hat{\psi}_\uparrow(\mathbf{r}_1) \rangle & \langle \hat{\psi}_\downarrow^\dagger(\mathbf{r}_2) \hat{\psi}_\downarrow(\mathbf{r}_1) \rangle \end{pmatrix} + g \begin{pmatrix} \langle \hat{\psi}_\downarrow^\dagger(\mathbf{r}_2) \hat{\psi}_\downarrow(\mathbf{r}_2) \hat{\psi}_\uparrow^\dagger(\mathbf{r}_2) \hat{\psi}_\uparrow(\mathbf{r}_1) \rangle & \langle \hat{\psi}_\downarrow^\dagger(\mathbf{r}_2) \hat{\psi}_\downarrow(\mathbf{r}_2) \hat{\psi}_\uparrow^\dagger(\mathbf{r}_2) \hat{\psi}_\downarrow(\mathbf{r}_1) \rangle \\ \langle \hat{\psi}_\uparrow^\dagger(\mathbf{r}_2) \hat{\psi}_\uparrow(\mathbf{r}_2) \hat{\psi}_\downarrow^\dagger(\mathbf{r}_2) \hat{\psi}_\uparrow(\mathbf{r}_1) \rangle & \langle \hat{\psi}_\uparrow^\dagger(\mathbf{r}_2) \hat{\psi}_\uparrow(\mathbf{r}_2) \hat{\psi}_\downarrow^\dagger(\mathbf{r}_2) \hat{\psi}_\downarrow(\mathbf{r}_1) \rangle \end{pmatrix} = 0 \quad (\text{C.5})$$

Finally, we transpose Eq.(C.5) and add it to Eq.(C.4). We also define

$$\hat{f}(\mathbf{r}_1, \mathbf{r}_2) = \begin{pmatrix} f_{\uparrow\uparrow}(\mathbf{r}_1, \mathbf{r}_2) & f_{\downarrow\uparrow}(\mathbf{r}_1, \mathbf{r}_2) \\ f_{\uparrow\downarrow}(\mathbf{r}_1, \mathbf{r}_2) & f_{\downarrow\downarrow}(\mathbf{r}_1, \mathbf{r}_2) \end{pmatrix} = \begin{pmatrix} \langle \hat{\psi}_\uparrow^\dagger(\mathbf{r}_2) \hat{\psi}_\uparrow(\mathbf{r}_1) \rangle & \langle \hat{\psi}_\downarrow^\dagger(\mathbf{r}_2) \hat{\psi}_\uparrow(\mathbf{r}_1) \rangle \\ \langle \hat{\psi}_\uparrow^\dagger(\mathbf{r}_2) \hat{\psi}_\downarrow(\mathbf{r}_1) \rangle & \langle \hat{\psi}_\downarrow^\dagger(\mathbf{r}_2) \hat{\psi}_\downarrow(\mathbf{r}_1) \rangle \end{pmatrix}. \quad (\text{C.6})$$

C.1 Non-interacting part

We first concentrate on the non-interacting part. After adding Eqs. (C.4) and (C.5)-transposed, we define center-of-mass and relative position coordinates: $\mathbf{R} = (\mathbf{r}_1 + \mathbf{r}_2)/2$, $\mathbf{r} = \mathbf{r}_1 - \mathbf{r}_2$. This leads to

$$\left[i\frac{\partial}{\partial t} + \frac{\nabla_{\mathbf{r}} \cdot \nabla_{\mathbf{R}}}{m} - \nabla_{\mathbf{R}} U(\mathbf{R}) \cdot \mathbf{r} \right] \hat{f}(\mathbf{r}, \mathbf{R}, t) + i\alpha_x \left[\sigma_x, \partial_{x_r} \hat{f} \right] + i\alpha_y \left[\sigma_y, \partial_{y_r} \hat{f} \right] + \frac{i\alpha_x}{2} \{ \sigma_x, \partial_{x_R} \hat{f} \} + \frac{i\alpha_y}{2} \{ \sigma_y, \partial_{y_R} \hat{f} \} = 0, \quad (\text{C.7})$$

where we assumed slow variation of the potential: $U(\mathbf{R} + \mathbf{r}/2) - U(\mathbf{R} - \mathbf{r}/2) \approx \nabla_{\mathbf{R}} U(\mathbf{R}) \cdot \mathbf{r}$. We now transform $\hat{f}(\mathbf{r}, \mathbf{R})$ to a Wigner distribution: $\hat{f}(\mathbf{p}, \mathbf{R}) = \int d\mathbf{r} \exp(i\mathbf{p} \cdot \mathbf{r}/\hbar) \hat{f}(\mathbf{r}, \mathbf{R})$, which finally gives

$$\left[\frac{\partial}{\partial t} + \frac{\mathbf{p}}{m} \cdot \nabla_{\mathbf{R}} - \nabla_{\mathbf{R}} U(\mathbf{R}, t) \cdot \nabla_{\mathbf{p}} \right] \hat{f}(\mathbf{p}, \mathbf{R}, t) + ip_x \alpha_x \left[\sigma_x, \hat{f}(\mathbf{p}, \mathbf{R}, t) \right] + ip_y \alpha_y \left[\sigma_y, \hat{f}(\mathbf{p}, \mathbf{R}, t) \right] + \frac{1}{2} \alpha_x \{ \sigma_x, \partial_x \hat{f}(\mathbf{p}, \mathbf{R}, t) \} + \frac{1}{2} \alpha_y \{ \sigma_y, \partial_y \hat{f}(\mathbf{p}, \mathbf{R}, t) \} = 0, \quad (\text{C.8})$$

where $\partial_{x,y}$ represent derivatives with respect to the spatial coordinate \mathbf{R} .

C.2 Interacting part

After adding Eqs. (C.4) and (C.5)-transposed, the interacting part is:

$$g \left(\begin{aligned} & \langle \hat{\psi}_{\downarrow}^{\dagger}(\mathbf{r}_2) \hat{\psi}_{\downarrow}(\mathbf{r}_2) \rangle \langle \hat{\psi}_{\uparrow}^{\dagger}(\mathbf{r}_2) \hat{\psi}_{\uparrow}(\mathbf{r}_1) \rangle - \langle \hat{\psi}_{\uparrow}^{\dagger}(\mathbf{r}_2) \hat{\psi}_{\uparrow}(\mathbf{r}_1) \rangle \langle \hat{\psi}_{\downarrow}^{\dagger}(\mathbf{r}_1) \hat{\psi}_{\downarrow}(\mathbf{r}_1) \rangle \\ & \langle \hat{\psi}_{\downarrow}^{\dagger}(\mathbf{r}_2) \hat{\psi}_{\downarrow}(\mathbf{r}_2) \rangle \langle \hat{\psi}_{\uparrow}^{\dagger}(\mathbf{r}_2) \hat{\psi}_{\downarrow}(\mathbf{r}_1) \rangle - \langle \hat{\psi}_{\uparrow}^{\dagger}(\mathbf{r}_2) \hat{\psi}_{\downarrow}(\mathbf{r}_1) \rangle \langle \hat{\psi}_{\uparrow}^{\dagger}(\mathbf{r}_1) \hat{\psi}_{\uparrow}(\mathbf{r}_1) \rangle \\ & \langle \hat{\psi}_{\uparrow}^{\dagger}(\mathbf{r}_2) \hat{\psi}_{\uparrow}(\mathbf{r}_2) \rangle \langle \hat{\psi}_{\downarrow}^{\dagger}(\mathbf{r}_2) \hat{\psi}_{\uparrow}(\mathbf{r}_1) \rangle - \langle \hat{\psi}_{\downarrow}^{\dagger}(\mathbf{r}_2) \hat{\psi}_{\uparrow}(\mathbf{r}_1) \rangle \langle \hat{\psi}_{\downarrow}^{\dagger}(\mathbf{r}_1) \hat{\psi}_{\downarrow}(\mathbf{r}_1) \rangle \\ & \langle \hat{\psi}_{\uparrow}^{\dagger}(\mathbf{r}_2) \hat{\psi}_{\uparrow}(\mathbf{r}_2) \rangle \langle \hat{\psi}_{\downarrow}^{\dagger}(\mathbf{r}_2) \hat{\psi}_{\downarrow}(\mathbf{r}_1) \rangle - \langle \hat{\psi}_{\downarrow}^{\dagger}(\mathbf{r}_2) \hat{\psi}_{\downarrow}(\mathbf{r}_1) \rangle \langle \hat{\psi}_{\uparrow}^{\dagger}(\mathbf{r}_1) \hat{\psi}_{\uparrow}(\mathbf{r}_1) \rangle \end{aligned} \right). \quad (\text{C.9})$$

Hartree-Fock approximation decouples the expectation value of quartic field operator terms [79]:

$$\langle \hat{\psi}_1^\dagger \hat{\psi}_2 \hat{\psi}_3^\dagger \hat{\psi}_4 \rangle \rightarrow \langle \hat{\psi}_1^\dagger \hat{\psi}_2 \rangle \langle \hat{\psi}_3^\dagger \hat{\psi}_4 \rangle - \langle \hat{\psi}_1^\dagger \hat{\psi}_4 \rangle \langle \hat{\psi}_3^\dagger \hat{\psi}_2 \rangle, \quad (\text{C.10})$$

and the interacting part becomes:

$$g \left(\begin{aligned} & n_{\downarrow}(\mathbf{r}_2) f_{\uparrow\uparrow}(\mathbf{r}_1, \mathbf{r}_2) - n_{-}(\mathbf{r}_2) f_{\downarrow\uparrow}(\mathbf{r}_1, \mathbf{r}_2) - n_{\downarrow}(\mathbf{r}_1) f_{\uparrow\uparrow}(\mathbf{r}_1, \mathbf{r}_2) + n_{+}(\mathbf{r}_1) f_{\uparrow\downarrow}(\mathbf{r}_1, \mathbf{r}_2) \\ & n_{\uparrow}(\mathbf{r}_2) f_{\downarrow\uparrow}(\mathbf{r}_1, \mathbf{r}_2) - n_{+}(\mathbf{r}_2) f_{\uparrow\uparrow}(\mathbf{r}_1, \mathbf{r}_2) - n_{\downarrow}(\mathbf{r}_1) f_{\downarrow\uparrow}(\mathbf{r}_1, \mathbf{r}_2) + n_{+}(\mathbf{r}_1) f_{\downarrow\downarrow}(\mathbf{r}_1, \mathbf{r}_2) \\ & n_{\downarrow}(\mathbf{r}_2) f_{\uparrow\downarrow}(\mathbf{r}_1, \mathbf{r}_2) - n_{-}(\mathbf{r}_2) f_{\downarrow\downarrow}(\mathbf{r}_1, \mathbf{r}_2) - n_{\uparrow}(\mathbf{r}_1) f_{\uparrow\downarrow}(\mathbf{r}_1, \mathbf{r}_2) + n_{-}(\mathbf{r}_1) f_{\uparrow\uparrow}(\mathbf{r}_1, \mathbf{r}_2) \\ & n_{\uparrow}(\mathbf{r}_2) f_{\downarrow\downarrow}(\mathbf{r}_1, \mathbf{r}_2) - n_{+}(\mathbf{r}_2) f_{\uparrow\downarrow}(\mathbf{r}_1, \mathbf{r}_2) - n_{\uparrow}(\mathbf{r}_1) f_{\downarrow\downarrow}(\mathbf{r}_1, \mathbf{r}_2) + n_{-}(\mathbf{r}_1) f_{\downarrow\uparrow}(\mathbf{r}_1, \mathbf{r}_2) \end{aligned} \right), \quad (\text{C.11})$$

where $n_{\uparrow}(\mathbf{r}) = f_{\uparrow\uparrow}(\mathbf{r}, \mathbf{r})$, $n_{\downarrow}(\mathbf{r}) = f_{\downarrow\downarrow}(\mathbf{r}, \mathbf{r})$, $n_{+}(\mathbf{r}) = f_{\uparrow\downarrow}(\mathbf{r}, \mathbf{r})$, $n_{-}(\mathbf{r}) = f_{\downarrow\uparrow}(\mathbf{r}, \mathbf{r})$.

After assuming slow variation of $n_{\uparrow}(\mathbf{r})$, $n_{\downarrow}(\mathbf{r})$, $n_{+}(\mathbf{r})$, $n_{-}(\mathbf{r})$ (similarly as we did for $U(\mathbf{r})$) and after taking a Fourier transform with respect to the relative position coordinate, the full equation becomes (including the non-interacting part):

$$\begin{aligned} & \frac{\partial \hat{f}}{\partial t} + \frac{\mathbf{p}}{m} \cdot \nabla_{\mathbf{R}} \hat{f} - \frac{i}{\hbar} \left[\hat{f}, \alpha (p_x \hat{\sigma}_x + p_y \hat{\sigma}_y) + \hat{V} \right] \\ & - \frac{1}{2} \{ \nabla_{\mathbf{p}} \hat{f}, \nabla_{\mathbf{R}} \hat{V} \} + \frac{1}{2} \alpha \{ \partial_x \hat{f}, \hat{\sigma}_x \} + \frac{1}{2} \alpha \{ \partial_y \hat{f}, \hat{\sigma}_y \} = 0, \end{aligned} \quad (\text{C.12})$$

where

$$\hat{f}(\mathbf{R}, \mathbf{p}, t) = \begin{pmatrix} f_{\uparrow\uparrow}(\mathbf{R}, \mathbf{p}, t) & f_{\downarrow\uparrow}(\mathbf{R}, \mathbf{p}, t) \\ f_{\uparrow\downarrow}(\mathbf{R}, \mathbf{p}, t) & f_{\downarrow\downarrow}(\mathbf{R}, \mathbf{p}, t) \end{pmatrix},$$

$$\hat{V}(\mathbf{R}, t) = \begin{pmatrix} U(\mathbf{R}, t) + gn_{\downarrow}(\mathbf{R}, t) & -gn_{-}(\mathbf{R}, t) \\ -gn_{+}(\mathbf{R}, t) & U(\mathbf{R}, t) + gn_{\uparrow}(\mathbf{R}, t) \end{pmatrix}.$$

This collisionless Boltzmann equation is almost an equivalent of dynamical Hartree-Fock equations. The only difference is in the assumption that $U(\mathbf{r})$, density and magnetization have slow spatial variations.

Appendix D: RPA susceptibility in the presence of spin-orbit coupling

Here we show how to calculate (spinful) density-density response function $\chi_{ij,mn}(\mathbf{p}, \omega)$ of a Bose gas with spin-orbit coupling. By investigating the poles of $\chi_{ij,mn}(\mathbf{p}, \omega)$ we want to probe possible transitions to magnetically ordered states at finite wave-vector which may happen at temperatures greater than the BEC transition temperature. We first calculate the non-interacting susceptibility, and later we include interactions using the Random phase approximation.

D.1 Non-interacting susceptibility

The system under consideration is described by the following single-particle Hamiltonian:

$$H_0 = \frac{\mathbf{k}^2}{2m} + \alpha k_x \tilde{\sigma}_z + \frac{\Omega}{2} \tilde{\sigma}_x, \quad (\text{D.1})$$

where $\mathbf{k} = -i\nabla$, and we set $\hbar = 1$. The response function is defined as

$$\chi_{ij,mn}(\mathbf{r}, t) = -i\theta(t) \left\langle \left[\psi_i^\dagger(\mathbf{r}, t) \psi_j(\mathbf{r}, t), \psi_m^\dagger(0, 0) \psi_n(0, 0) \right] \right\rangle, \quad (\text{D.2})$$

where $\theta(t)$ is the Heaviside theta function. In the momentum and frequency space it has the following form:

$$\begin{aligned}\chi_{ij,mn}(\mathbf{p}, t) &= \int d^3\mathbf{r} \chi_{ij,mn}(\mathbf{r}, t) e^{-i\mathbf{p}\cdot\mathbf{r}} \\ &= \frac{-i}{V} \theta(t) \sum_{k,q} \left\langle \left[a_{k,i}^\dagger(t) a_{k+p,j}(t), a_{q,m}^\dagger(0) a_{q-p,n}(0) \right] \right\rangle,\end{aligned}\quad (\text{D.3})$$

$$\chi_{ij,mn}(\mathbf{p}, \omega) = \int_{-\infty}^{\infty} \chi_{ij,mn}(\mathbf{p}, t) e^{i\omega t - \eta t} dt, \quad \eta \rightarrow 0^+, \quad (\text{D.4})$$

where V is the volume of a system. To find the response function in the frequency space, it is convenient to define creation/annihilation operators corresponding to eigenstates of Hamiltonian (D.1):

$$b_-(k) = T_{11}(k) a_\uparrow(k) + T_{12}(k) a_\downarrow(k) \quad (\text{D.5})$$

$$b_+(k) = T_{21}(k) a_\uparrow(k) + T_{22}(k) a_\downarrow(k),$$

where

$$\begin{aligned}T_{11}(k) &= -\frac{1}{\sqrt{1 + \left(\frac{2\alpha k_x}{\Omega} + \sqrt{\frac{4\alpha^2 k_x^2}{\Omega^2} + 1} \right)^2}}, & T_{12}(k) &= \frac{\frac{2\alpha k_x}{\Omega} + \sqrt{\frac{4\alpha^2 k_x^2}{\Omega^2} + 1}}{\sqrt{1 + \left(\frac{2\alpha k_x}{\Omega} + \sqrt{\frac{4\alpha^2 k_x^2}{\Omega^2} + 1} \right)^2}} \\ T_{21}(k) &= -\frac{1}{\sqrt{1 + \left(\frac{2\alpha k_x}{\Omega} - \sqrt{\frac{4\alpha^2 k_x^2}{\Omega^2} + 1} \right)^2}}, & T_{22}(k) &= \frac{\frac{2\alpha k_x}{\Omega} - \sqrt{\frac{4\alpha^2 k_x^2}{\Omega^2} + 1}}{\sqrt{1 + \left(\frac{2\alpha k_x}{\Omega} - \sqrt{\frac{4\alpha^2 k_x^2}{\Omega^2} + 1} \right)^2}}\end{aligned}\quad (\text{D.6})$$

Time dependence is given by

$$b_\pm(k, t) = b_\pm(k) e^{-iE_\pm(k)t}, \quad E_\pm(k) = \frac{k^2}{2m} \pm \sqrt{\alpha^2 k_x^2 + \frac{\Omega^2}{4}}, \quad (\text{D.7})$$

and the response function in the frequency space is

$$\begin{aligned}
\chi_{ij,mn}(\mathbf{p}, \omega) &= \frac{1}{V} \sum_{k,q} \left\{ \begin{aligned} &\frac{T_{1i}(k)T_{1j}(k+p)T_{1m}(q)T_{1n}(q-p)}{\omega + E_-(k) - E_-(k+p) + i\eta} \left\langle \left[b_-^\dagger(k)b_-(k+p), b_-^\dagger(q)b_-(q-p) \right] \right\rangle \\ &+ \frac{T_{2i}(k)T_{2j}(k+p)T_{2m}(q)T_{2n}(q-p)}{\omega + E_+(k) - E_+(k+p) + i\eta} \left\langle \left[b_+^\dagger(k)b_+(k+p), b_+^\dagger(q)b_+(q-p) \right] \right\rangle \\ &+ \frac{T_{1i}(k)T_{2j}(k+p)T_{2m}(q)T_{1n}(q-p)}{\omega + E_-(k) - E_+(k+p) + i\eta} \left\langle \left[b_-^\dagger(k)b_+(k+p), b_+^\dagger(q)b_-(q-p) \right] \right\rangle \\ &+ \frac{T_{2i}(k)T_{1j}(k+p)T_{1m}(q)T_{2n}(q-p)}{\omega + E_+(k) - E_-(k+p) + i\eta} \left\langle \left[b_+^\dagger(k)b_-(k+p), b_-^\dagger(q)b_+(q-p) \right] \right\rangle \end{aligned} \right\} \\
&= \int \frac{dk^3}{(2\pi)^3} \left\{ \begin{aligned} &\frac{T_{1i}(k)T_{1n}(k)T_{1j}(k+p)T_{1m}(k+p)}{\omega + E_-(k) - E_-(k+p) + i\eta} [N_-(k) - N_-(k+p)] \\ &+ \frac{T_{2i}(k)T_{2n}(k)T_{2j}(k+p)T_{2m}(k+p)}{\omega + E_+(k) - E_+(k+p) + i\eta} [N_+(k) - N_+(k+p)] \\ &+ \frac{T_{1i}(k)T_{1n}(k)T_{2j}(k+p)T_{2m}(k+p)}{\omega + E_-(k) - E_+(k+p) + i\eta} [N_-(k) - N_+(k+p)] \\ &+ \frac{T_{2i}(k)T_{2n}(k)T_{1j}(k+p)T_{1m}(k+p)}{\omega + E_+(k) - E_-(k+p) + i\eta} [N_+(k) - N_-(k+p)] \end{aligned} \right\} \quad (\text{D.8})
\end{aligned}$$

The expression is not easy to evaluate and we use Kramers-Kronig relations to simplify the calculation. Kramers-Kronig relations relate real and imaginary part of a response function ($\chi(\omega) = \chi_1(\omega) + i\chi_2(\omega)$):

$$\begin{aligned}
\chi_1(\omega) &= \frac{1}{\pi} \mathcal{P} \int_{-\infty}^{\infty} \frac{\chi_2(\omega')}{\omega' - \omega} d\omega' \\
\chi_2(\omega) &= -\frac{1}{\pi} \mathcal{P} \int_{-\infty}^{\infty} \frac{\chi_1(\omega')}{\omega' - \omega} d\omega' \quad (\text{D.9})
\end{aligned}$$

This means that if we calculate only the imaginary part of Eq.(D.8), the real part can be found using Kramers-Kronig relations. The imaginary part of Eq.(D.8) is

$$\begin{aligned} \text{Im} [\chi_{ij,mn}(\mathbf{p}, \omega)] = -\pi \int \frac{dk^3}{(2\pi)^3} \left\{ \right. \\ & T_{1i}(k)T_{1n}(k)T_{1j}(k+p)T_{1m}(k+p) [N_-(k) - N_-(k+p)] \delta(\omega + E_-(k) - E_-(k+p)) \\ & + T_{2i}(k)T_{2n}(k)T_{2j}(k+p)T_{2m}(k+p) [N_+(k) - N_+(k+p)] \delta(\omega + E_+(k) - E_+(k+p)) \\ & + T_{1i}(k)T_{1n}(k)T_{2j}(k+p)T_{2m}(k+p) [N_-(k) - N_+(k+p)] \delta(\omega + E_-(k) - E_+(k+p)) \\ & \left. + T_{2i}(k)T_{2n}(k)T_{1j}(k+p)T_{1m}(k+p) [N_+(k) - N_-(k+p)] \delta(\omega + E_+(k) - E_-(k+p)) \right\}, \end{aligned} \quad (\text{D.10})$$

and it can be evaluated numerically.

D.2 Interaction susceptibility in RPA

Contact interparticle interactions of the type:

$$U_{\text{int}} = \int d^3\mathbf{r} \left[\frac{1}{2}g_{11}n_{\uparrow}^2(\mathbf{r}) + \frac{1}{2}g_{22}n_{\downarrow}^2(\mathbf{r}) + g_{12}n_{\uparrow}(\mathbf{r})n_{\downarrow}(\mathbf{r}) \right] \quad (\text{D.11})$$

lead to the following dynamical Hartree-Fock equation:

$$i\hbar \frac{\partial \vec{\psi}}{\partial t} = \hat{H}_0 \vec{\psi} + \hat{V}_{\text{HF}} \vec{\psi}, \quad (\text{D.12})$$

where

$$\hat{V}_{\text{HF}} = \begin{pmatrix} 2g_{11}n_{\uparrow\uparrow} + g_{12}n_{\downarrow\downarrow} & g_{12}n_{\downarrow\uparrow} \\ g_{12}n_{\uparrow\downarrow} & 2g_{22}n_{\downarrow\downarrow} + g_{12}n_{\uparrow\uparrow} \end{pmatrix}, \quad (\text{D.13})$$

and H_0 is a single-particle Hamiltonian.

We now derive RPA expression for the susceptibility by linearizing dynamical Hartree-Fock equation [79]. The variation in density is induced by the variation of

an external field U^0 and variation of a potential created by interparticle interactions (U^{int}):

$$\delta n_\alpha(\mathbf{k}, \omega) = \sum_\beta \chi_{\alpha\beta}^0(\mathbf{k}, \omega) [\delta U_\beta^0(\mathbf{k}, \omega) + \delta U_\beta^{\text{int}}(\mathbf{k}, \omega)], \quad (\text{D.14})$$

where χ^0 is the non-interacting susceptibility, and indices run from 1 to 4 [$1 = (\uparrow\uparrow) = (11)$, $2 = (\uparrow\downarrow) = (12)$, $3 = (\downarrow\uparrow) = (21)$, $4 = (\downarrow\downarrow) = (22)$]. The interacting susceptibility is defined as:

$$\chi_{\alpha\beta}^{\text{RPA}}(\mathbf{k}, \omega) = \frac{\delta n_\alpha(\mathbf{k}, \omega)}{\delta U_\beta^0(\mathbf{k}, \omega)}, \quad (\text{D.15})$$

and the interaction-induced potential is:

$$\delta U_\alpha^{\text{int}}(\mathbf{k}, \omega) = \sum_\beta V_{\alpha\beta} \delta n_\beta(\mathbf{k}, \omega), \quad \hat{V} = \begin{pmatrix} 2g_{11} & 0 & 0 & g_{12} \\ 0 & 0 & g_{12} & 0 \\ 0 & g_{12} & 0 & 0 \\ g_{12} & 0 & 0 & 2g_{22} \end{pmatrix}. \quad (\text{D.16})$$

Finally, the RPA susceptibility is

$$\chi_{\alpha\beta}^{\text{RPA}} = \chi_{\alpha\beta}^0 + \sum_{\gamma,\delta} \chi_{\alpha\gamma}^0 V_{\gamma\delta} \chi_{\delta\beta}^{\text{RPA}}, \quad (\text{D.17})$$

or in the matrix notation:

$$\hat{\chi}^{\text{RPA}} = \left(\hat{\mathbf{1}} - \hat{\chi}^0 \hat{V} \right)^{-1} \hat{\chi}^0, \quad (\text{D.18})$$

where

$$\hat{\chi}^0 = \begin{pmatrix} \chi_0 & 0 & 0 & 0 \\ 0 & 0 & \chi_0 & 0 \\ 0 & \chi_0 & 0 & 0 \\ 0 & 0 & 0 & \chi_0 \end{pmatrix}, \quad (\text{D.19})$$

and χ_0 is given in section 5.3.

Appendix E: Strongly correlated bosons with quartic dispersion:
various calculations

E.1 Box-potential ground state in a system with quartic dispersion

Here we show how to find a spectrum of a particle in box potential with Hamiltonian $H_4 = k_x^4 = \partial_x^4$. While H_4 is similar to the usual quadratic dispersion in a sense that both are diagonal in momentum space, there is one fundamental difference: in a system with H_4 , not only the wave-function, but also its first derivative has to be continuous for the wave-function to have finite energy expectation value.

If we choose a box of length L and $-L/2 < x < L/2$, then the boundary conditions are $\psi(-L/2) = \psi(L/2) = 0$ and $\partial_x\psi(-L/2) = \partial_x\psi(L/2) = 0$. Solutions of the equation $\partial_x^4\psi = E\psi$ are $\exp(kx)$, $\exp(-kx)$, $\exp(ikx)$ and $\exp(-ikx)$, where $k = E^{1/4}$. Since H_4 is symmetric under inversion ($x \rightarrow -x$), we expect a symmetric ground state:

$$\psi_0(x) = a_1 (e^{kx} + e^{-kx}) + a_2 \cos(kx), \quad (\text{E.1})$$

where a_1 , a_2 are coefficients that have to be determined. Boundary conditions then require $\tan(kL/2) = -\tanh(kL/2)$, which can be solved graphically: in the ground state $kL = 4.730$ and $E_0 = 5.140 (\pi/L)^4$. The ratio of coefficients is $a_2/a_1 = 15.06$.

E.2 Monte-Carlo calculations

Here we describe Monte-Carlo methods we used to calculate the kinetic energy of various trial wave-functions. We were primarily interested in finding the expectation value of Hamiltonian (6.5) and for analytic wave-functions this can be done in two ways. As in standard Variational Monte Carlo techniques, the first step is to sample the “local energy”, $E_{\text{loc}} = (\hat{H}\psi)/\psi$ [150]:

$$E_{\text{kin}} = \frac{\int \psi^* \hat{H} \psi d\mathbf{R}}{\int |\psi|^2 d\mathbf{R}} = \frac{\int |\psi|^2 \frac{\hat{H}\psi}{\psi} d\mathbf{R}}{\int |\psi|^2 d\mathbf{R}}, \quad (\text{E.2})$$

where $\hat{H} = \sum_j \partial_{x_j}^4/4 - \partial_{y_j}^2$, and $d\mathbf{R} = d\mathbf{r}_1 d\mathbf{r}_2 \cdots d\mathbf{r}_N$. We then use a Metropolis algorithm to sample the local energy with probability distribution $P(\mathbf{R}) = |\psi(\mathbf{R})|^2 / \int |\psi(\mathbf{R}')|^2 d\mathbf{R}'$.

In the case of non-analytic wave-functions like $\psi_{B,\text{abs}}$ and $\psi_{B,\text{cf}}$ the expectation value of $\partial_{x_j}^4$ cannot be calculated this way because a finite energy is associated with points which have discontinuous derivatives of ψ . The correct method in that case is to first calculate the momentum distribution of the state, and then compute the expectation value of $\varepsilon_k = k_x^4/4 + k_y^2$. We calculate the momentum distribution $n(\mathbf{k})$ using:

$$n(\mathbf{k}) = N \int d\mathbf{r}_2 \cdots d\mathbf{r}_N |f(\mathbf{k}, \mathbf{r}_2, \dots, \mathbf{r}_N)|^2, \quad (\text{E.3})$$

$$f(\mathbf{k}, \mathbf{r}_2, \dots, \mathbf{r}_N) = \frac{1}{2\pi} \int d\mathbf{r}_1 e^{-i\mathbf{k}\cdot\mathbf{r}_1} \psi(\mathbf{r}_1, \dots, \mathbf{r}_N),$$

where we chose the following normalization: $\int |\psi(\mathbf{R})|^2 d\mathbf{R} = 1$ and $\int n(\mathbf{k}) d\mathbf{k} = N$.

This can be written in the form suitable for Metropolis importance sampling:

$$n(\mathbf{k}) = N \int d\mathbf{R} |\psi(\mathbf{R})|^2 |f_{\mathcal{N}}(\mathbf{k}, \mathbf{r}_2, \dots, \mathbf{r}_N)|^2, \quad (\text{E.4})$$

$$f_N(\mathbf{k}, \mathbf{r}_2, \dots, \mathbf{r}_N) = \frac{1}{2\pi} \int d\mathbf{r}_1 e^{-i\mathbf{k}\cdot\mathbf{r}_1} \psi_N(\mathbf{r}_1, \dots, \mathbf{r}_N),$$

$$\psi_N(\mathbf{r}_1, \dots, \mathbf{r}_N) = \frac{\psi(\mathbf{r}_1, \dots, \mathbf{r}_N)}{\sqrt{\int d\mathbf{r}' |\psi(\mathbf{r}', \mathbf{r}_2, \dots, \mathbf{r}_N)|^2}}.$$

For analytic wave-functions, both methods produce the same result.

The wave-functions we considered all have the property of being strongly anisotropic, i.e. they are given in terms of length-scales a_x, a_y where $a_x \ll a_y$. The best way to do calculations is then to rescale the coordinates so that in the new units $a_x \sim a_y \sim 1$. For example, in the case of $\psi_{B,\text{cf}}^{\text{sq}}$ we first calculate expectation values $\alpha_4 = \langle k_x^4 \rangle$ and $\alpha_2 = \langle k_y^2 \rangle$ for the wave-function with $a_x = a_y = 1$ (rescaled wave-function). The expectation values corresponding to the wave-function in the original units are then simply α_4/a_x^4 and α_2/a_y^2 , respectively. In the end, we minimize $E(a_x, a_y) = \langle k_x^4 \rangle/4 + \langle k_y^2 \rangle = \alpha_4/(4a_x^4) + \alpha_2/a_y^2$, while keeping the density $n = 1/(2\pi a_x a_y)$ constant.

In the case of wave-functions where we can apply periodic boundary condition ($\psi_{B,\text{abs}}, \psi_{B,\text{sq}}$, and ψ_J) we did calculations with $N = 400$ particles. However, in the case of composite-fermion wave-functions ($\psi_{B,\text{cf}}$ and $\psi_{B,\text{cf}}^{\text{sq}}$) we did calculations with $N = 1600$ particles. There the density of a wave-function with finite number of particles has a form of a droplet with radius $R = \sqrt{2(N-1)}$ (when $a_x = a_y = 1$) and the presence of the boundary increases the value of finite-size correction. Larger system sizes were therefore necessary.

E.3 Estimating the interaction energy of a spinless gas at small, but finite densities

In order to estimate the interaction energy at small densities, we can make a simple order-of-magnitude calculation: we choose some coordinates $\boldsymbol{\lambda} = (\mathbf{r}_3, \dots, \mathbf{r}_N)$ and we keep them fixed (see Appendix E for more details). Now we can write the wave-function as $\psi(\mathbf{r}_1, \mathbf{r}_2; \boldsymbol{\lambda})$, and we can define parameter C as a measure of a $\mathbf{r}_1 = \mathbf{r}_2$ wave-function amplitude:

$$C = V \frac{\int d\mathbf{r} |\psi(\mathbf{r}, \mathbf{r})|}{\int d\mathbf{r}_1 d\mathbf{r}_2 |\psi(\mathbf{r}_1, \mathbf{r}_2)|}, \quad (\text{E.5})$$

where V is the volume. We first estimate the kinetic energy: $E_{\text{kin}}(C) \sim n^{4/3}(1 - C)$. The reasoning is that for $C = 0$, $E_{\text{kin}} \sim n^{4/3}$. When $C = 1$, the gas is not correlated and $E_{\text{kin}} \approx 0$. Moreover, E_{kin} should not have an extremum around $C = 0$, and therefore should be linear in C in that region.

The interaction energy is $E_{\text{int}} \sim N^2 g \int d\mathbf{r} |\psi(\mathbf{r}, \mathbf{r})|^2 \sim gnC^2$. We minimize $E_{\text{kin}} + E_{\text{int}}$ with respect to C and the optimal C is $C \sim n^{1/3}/g$, and $E_{\text{int}} \sim n^{5/3}/g$. This means $E_{\text{int}}/E_{\text{kin}} \sim n^{1/3}$, that is the kinetic energy is a dominant part at low densities. The same reasoning gives the correct density scaling of E_{int} in the low-density regime of a 1D Lieb-Liniger gas.

E.4 Kinetic energy of a many-body wave-function

Here we show that spinful wave-function constructed in Eq.(6.11) has the same kinetic energy as the corresponding spinless wave-function.

We consider the following state:

$$|\psi\rangle = \sum_{\mathbf{k}_1 \dots \mathbf{k}_N} f_B(\mathbf{k}_1, \dots, \mathbf{k}_N) |\mathbf{k}_1 \dots \mathbf{k}_N\rangle, \quad (\text{E.6})$$

where f_B is normalized: $\sum_{\mathbf{k}_1, \dots, \mathbf{k}_N} |f_B|^2 = 1$, and $|\mathbf{k}_1 \dots \mathbf{k}_N\rangle = |\mathbf{k}_1\rangle \otimes \dots \otimes |\mathbf{k}_N\rangle$ is an orthonormal momentum-eigenstate basis. Here state $|\mathbf{k}\rangle$ can describe either a spinless or spinful [Eq.(6.4)] single-particle momentum eigenstate. The state $|\mathbf{k}_1 \dots \mathbf{k}_N\rangle$ is an eigenstate of kinetic energy operator with energy $\varepsilon_{\mathbf{k}_1 \dots \mathbf{k}_N} = \varepsilon_{\mathbf{k}_1} + \dots + \varepsilon_{\mathbf{k}_N}$. Therefore

$$\begin{aligned} E_{\text{kin}} &= \sum_{\mathbf{k}_1 \dots \mathbf{k}_N} \varepsilon_{\mathbf{k}_1 \dots \mathbf{k}_N} |f_B(\mathbf{k}_1, \dots, \mathbf{k}_N)|^2 \\ &= \sum_{\mathbf{k}_1 \dots \mathbf{k}_N} (\varepsilon_{\mathbf{k}_1} + \dots + \varepsilon_{\mathbf{k}_N}) |f_B(\mathbf{k}_1, \dots, \mathbf{k}_N)|^2 \\ &= \sum_{\mathbf{k}_1} \varepsilon_{\mathbf{k}_1} \sum_{\mathbf{k}_2 \dots \mathbf{k}_N} |f_B(\mathbf{k}_1, \dots, \mathbf{k}_N)|^2 + \dots \\ &= \sum_{\mathbf{k}} \varepsilon_{\mathbf{k}} n_{\mathbf{k}}, \end{aligned} \quad (\text{E.7})$$

where we assumed f_B is symmetric with respect to particle exchange and $n_{\mathbf{k}}$ is the single-particle momentum distribution:

$$n_{\mathbf{k}} = N \sum_{\mathbf{k}_2 \dots \mathbf{k}_N} |f_B(\mathbf{k}, \mathbf{k}_2, \dots, \mathbf{k}_N)|^2. \quad (\text{E.8})$$

It is clear that kinetic energy does not depend on whether $|\psi\rangle$ [Eq.(E.6)] describes a spinless or spinful state, as long their momentum representation f_B and dispersion $\varepsilon_{\mathbf{k}}$ are the same.

E.5 Estimating spinful state interaction energy

The spinful state is defined as

$$|\psi_{B,s}\rangle = \sum_{\mathbf{k}_1 \dots \mathbf{k}_N} f_B(\mathbf{k}_1, \dots, \mathbf{k}_N) |\mathbf{k}_1 \dots \mathbf{k}_N\rangle_s, \quad (\text{E.9})$$

where $|\mathbf{k}_1 \dots \mathbf{k}_N\rangle_s = |\mathbf{k}_1\rangle_s \otimes \dots \otimes |\mathbf{k}_N\rangle_s$ and $|\mathbf{k}\rangle_s$ is a lower-band single-particle state.

The real-space representation of $|\mathbf{k}_1 \dots \mathbf{k}_N\rangle_s$ is

$$\begin{bmatrix} \langle \mathbf{r}_1 \dots \mathbf{r}_N; \uparrow \uparrow \dots \uparrow | \mathbf{k}_1 \dots \mathbf{k}_N \rangle_s \\ \langle \mathbf{r}_1 \dots \mathbf{r}_N; \uparrow \uparrow \dots \downarrow | \mathbf{k}_1 \dots \mathbf{k}_N \rangle_s \\ \vdots \\ \langle \mathbf{r}_1 \dots \mathbf{r}_N; \downarrow \downarrow \dots \uparrow | \mathbf{k}_1 \dots \mathbf{k}_N \rangle_s \\ \langle \mathbf{r}_1 \dots \mathbf{r}_N; \downarrow \downarrow \dots \downarrow | \mathbf{k}_1 \dots \mathbf{k}_N \rangle_s \end{bmatrix} = \begin{bmatrix} s_\uparrow(\mathbf{k}_1) s_\uparrow(\mathbf{k}_2) \dots s_\uparrow(\mathbf{k}_N) \\ s_\uparrow(\mathbf{k}_1) s_\uparrow(\mathbf{k}_2) \dots s_\downarrow(\mathbf{k}_N) \\ \vdots \\ s_\downarrow(\mathbf{k}_1) s_\downarrow(\mathbf{k}_2) \dots s_\uparrow(\mathbf{k}_N) \\ s_\downarrow(\mathbf{k}_1) s_\downarrow(\mathbf{k}_2) \dots s_\downarrow(\mathbf{k}_N) \end{bmatrix} \times e^{i(\mathbf{k}_1 \cdot \mathbf{r}_1 + \dots + \mathbf{k}_N \cdot \mathbf{r}_N)}, \quad (\text{E.10})$$

where $s_\uparrow(\mathbf{k})$, $s_\downarrow(\mathbf{k})$ are given in eq.(6.4). The real-space representation of the spinful wave-function is then

$$\begin{bmatrix} \psi_{\uparrow \uparrow \dots \uparrow}(\mathbf{r}_1, \dots, \mathbf{r}_N) \\ \psi_{\uparrow \uparrow \dots \downarrow}(\mathbf{r}_1, \dots, \mathbf{r}_N) \\ \vdots \\ \psi_{\downarrow \downarrow \dots \uparrow}(\mathbf{r}_1, \dots, \mathbf{r}_N) \\ \psi_{\downarrow \downarrow \dots \downarrow}(\mathbf{r}_1, \dots, \mathbf{r}_N) \end{bmatrix} = \sum_{\mathbf{k}_1 \dots \mathbf{k}_N} f_B(\mathbf{k}_1, \dots, \mathbf{k}_N) \times \begin{bmatrix} s_\uparrow(\mathbf{k}_1) s_\uparrow(\mathbf{k}_2) \dots s_\uparrow(\mathbf{k}_N) \\ s_\uparrow(\mathbf{k}_1) s_\uparrow(\mathbf{k}_2) \dots s_\downarrow(\mathbf{k}_N) \\ \vdots \\ s_\downarrow(\mathbf{k}_1) s_\downarrow(\mathbf{k}_2) \dots s_\uparrow(\mathbf{k}_N) \\ s_\downarrow(\mathbf{k}_1) s_\downarrow(\mathbf{k}_2) \dots s_\downarrow(\mathbf{k}_N) \end{bmatrix} e^{i(\mathbf{k}_1 \cdot \mathbf{r}_1 + \dots + \mathbf{k}_N \cdot \mathbf{r}_N)}. \quad (\text{E.11})$$

We are interested in the low-density regime and there $|\mathbf{k}| \ll 1$. We can then

expand spin coefficients as:

$$\begin{aligned} s_{\uparrow}(\mathbf{k}) &= -\frac{1}{\sqrt{2}} \left(1 - \frac{k_x}{2} - \frac{k_x^2}{8} + \mathcal{O}(k_x^3) \right), \\ s_{\downarrow}(\mathbf{k}) &= \frac{1}{\sqrt{2}} \left(1 + \frac{k_x}{2} - \frac{k_x^2}{8} + \mathcal{O}(k_x^3) \right) \end{aligned} \quad (\text{E.12})$$

Also, we can replace k_x with $-i\partial_x$. For example, the $\psi_{\downarrow\dots\downarrow}$ component is then:

$$\begin{aligned} \psi_{\downarrow\dots\downarrow} &= \left(\frac{1}{\sqrt{2}} \right)^N \left(1 - \frac{i\partial_{x_1}}{2} + \frac{\partial_{x_1}^2}{8} + \dots \right) \\ &\times \dots \times \left(1 - \frac{i\partial_{x_N}}{2} + \frac{\partial_{x_N}^2}{8} + \dots \right) \psi_B(\mathbf{r}_1, \dots, \mathbf{r}_N), \end{aligned} \quad (\text{E.13})$$

since by definition of f_B (Eq.(6.12)):

$$\psi_B(\mathbf{r}_1, \dots, \mathbf{r}_N) = \sum_{\mathbf{k}_1 \dots \mathbf{k}_N} f_B(\mathbf{k}_1, \dots, \mathbf{k}_N) e^{i(\mathbf{k}_1 \cdot \mathbf{r}_1 + \dots + \mathbf{k}_N \cdot \mathbf{r}_N)}. \quad (\text{E.14})$$

The strategy for calculating the interacting energy is: (a) we concentrate on expectation value of $V_{12} = g\delta(\mathbf{r}_1 - \mathbf{r}_2)$ (the total interaction energy will then be $N(N-1)/2$ times that value). (b) We first calculate the contribution to interaction energy coming from $\psi_{\downarrow\dots\downarrow}$ component. (c) We show that all other spin components give approximately the same contribution.

Estimating $\psi_{\downarrow\dots\downarrow}$ contribution.— The idea is to choose some random values for coordinates $\mathbf{r}_3, \dots, \mathbf{r}_N$ and keep them fixed [we define $\boldsymbol{\lambda} = (\mathbf{r}_3, \dots, \mathbf{r}_N)$]. This way we get a two-body wave-function from which it is easy to calculate $\langle V_{12} \rangle$. Later we show that almost any choice of $\boldsymbol{\lambda}$ gives the same value of $\langle V_{12} \rangle$.

We start by defining

$$\begin{aligned} \Phi(\mathbf{r}_1, \mathbf{r}_2; \boldsymbol{\lambda}) &= \mathcal{N}(\boldsymbol{\lambda}) \left(1 - \frac{i\partial_{x_1}}{2} + \frac{\partial_{x_1}^2}{8} + \dots \right) \\ &\times \left(1 - \frac{i\partial_{x_2}}{2} + \frac{\partial_{x_2}^2}{8} + \dots \right) \chi(\mathbf{r}_1, \mathbf{r}_2; \boldsymbol{\lambda}), \end{aligned} \quad (\text{E.15})$$

where

$$\begin{aligned} \chi(\mathbf{r}_1, \mathbf{r}_2; \boldsymbol{\lambda}) &= \left(1 - \frac{i\partial_{x_3}}{2} + \frac{\partial_{x_3}^2}{8} + \dots\right) \\ &\times \dots \times \left(1 - \frac{i\partial_{x_N}}{2} + \frac{\partial_{x_N}^2}{8} + \dots\right) \psi_B, \end{aligned} \quad (\text{E.16})$$

and $\mathcal{N}(\boldsymbol{\lambda})$ is such that

$$\int d\mathbf{r}_1 d\mathbf{r}_2 |\Phi(\mathbf{r}_1, \mathbf{r}_2; \boldsymbol{\lambda})|^2 = 1. \quad (\text{E.17})$$

We notice that $\Phi(\mathbf{r}_1, \mathbf{r}_2; \boldsymbol{\lambda})$ is simply equal to $\psi_{\downarrow\dots\downarrow}$, but with a different normalization [see Eq.(E.13)].

If ψ_B is analytical, we can Taylor-expand around $\mathbf{r}_1 - \mathbf{r}_2 = 0$:

$$\psi_B = \frac{1}{2}a_{xx}(x_1 - x_2)^2 + \frac{1}{2}a_{yy}(y_1 - y_2)^2 + a_{xy}(x_1 - x_2)(y_1 - y_2) + \dots, \quad (\text{E.18})$$

where we assume $\psi_B = 0$ when $\mathbf{r}_1 - \mathbf{r}_2 = 0$ and $a_{ij} = a_{ij}(\mathbf{r}_{\text{cm}}, \boldsymbol{\lambda})$, where $\mathbf{r}_{\text{cm}} = \mathbf{r}_1 + \mathbf{r}_2$.

χ retains the same structure, but with different coefficients:

$$\chi = \frac{1}{2}b_{xx}(x_1 - x_2)^2 + \frac{1}{2}b_{yy}(y_1 - y_2)^2 + b_{xy}(x_1 - x_2)(y_1 - y_2) + \dots, \quad (\text{E.19})$$

However, once we act on χ with $s_{\downarrow}(-i\partial_{x_1})s_{\downarrow}(-i\partial_{x_2})$, function Φ will have non-zero value for $\mathbf{r}_1 = \mathbf{r}_2$ which will give rise to finite interaction energy.

Let us make the change of variables: $x_r = x_1 - x_2$, $x_{\text{cm}} = x_1 + x_2$. Then:

$$\begin{aligned} \Phi|_{\mathbf{r}_1=\mathbf{r}_2} &\approx \left(1 - \frac{i\partial_{x_1}}{2} + \frac{\partial_{x_1}^2}{8}\right) \left(1 - \frac{i\partial_{x_2}}{2} + \frac{\partial_{x_2}^2}{8}\right) \chi(\mathbf{r}_1, \mathbf{r}_2; \boldsymbol{\lambda})|_{\mathbf{r}_1=\mathbf{r}_2} \\ &= \left[1 - \frac{i}{2}(\partial_{x_r} + \partial_{x_{\text{cm}}}) + \frac{1}{8}(\partial_{x_r} + \partial_{x_{\text{cm}}})^2\right] \\ &\quad \times \left[1 - \frac{i}{2}(-\partial_{x_r} + \partial_{x_{\text{cm}}}) + \frac{1}{8}(-\partial_{x_r} + \partial_{x_{\text{cm}}})^2\right] \chi(\mathbf{r}_1, \mathbf{r}_2; \boldsymbol{\lambda})|_{\mathbf{r}_1=\mathbf{r}_2} \quad (\text{E.20}) \\ &= \left(1 + \frac{1}{2}\partial_{x_r}^2 + \dots\right) \chi(\mathbf{r}_1, \mathbf{r}_2; \boldsymbol{\lambda})|_{\mathbf{r}_1=\mathbf{r}_2} \\ &= \frac{b_{xx}}{2}, \end{aligned}$$

We can estimate $b_{xx} \sim (\Delta k_x)^2 |\bar{\Phi}|$, where Δk_x is the momentum width in x direction and $|\bar{\Phi}|$ is the average magnitude of Φ :

$$|\bar{\Phi}|^2 = \frac{1}{V^2} \int d\mathbf{r}_1 d\mathbf{r}_2 |\Phi|^2 = \frac{1}{V^2}, \quad (\text{E.21})$$

where V is the volume. The interaction energy corresponding to Φ is then

$$\begin{aligned} E_{12}(\Phi) &= \int d\mathbf{r}_1 d\mathbf{r}_2 g \delta(\mathbf{r}_1 - \mathbf{r}_2) |\Phi(\mathbf{r}_1, \mathbf{r}_2)|^2 \\ &\sim V g (\Delta k_x)^4 |\bar{\Phi}|^2 \sim \frac{g}{V} (\Delta k_x)^4 \end{aligned} \quad (\text{E.22})$$

It is clear that a different choice of $\boldsymbol{\lambda}$ would give the same estimate. The same is true for different spin components $\psi_{\sigma_1, \dots, \sigma_N}$. Therefore, when we average over all $\boldsymbol{\lambda}$ and $\{\sigma_1, \dots, \sigma_N\}$:

$$\begin{aligned} \bar{E}_{12} &= \sum_{\sigma_1, \dots, \sigma_N} \int d\boldsymbol{\lambda} p_{\sigma_1, \dots, \sigma_N}(\boldsymbol{\lambda}) E_{12}[\Phi_{\sigma_1, \dots, \sigma_N}(\boldsymbol{\lambda})], \\ p_{\sigma_1, \dots, \sigma_N}(\boldsymbol{\lambda}) &= \int d\mathbf{r}_1 d\mathbf{r}_2 |\psi_{\sigma_1, \dots, \sigma_N}(\mathbf{r}_1, \mathbf{r}_2, \boldsymbol{\lambda})|^2, \end{aligned} \quad (\text{E.23})$$

the energy is again $\bar{E}_{12} \sim \frac{g}{V} (\Delta k_x)^4$. The total energy is then $E_{\text{int}} \sim N(N-1)/2 \times \bar{E}_{12} \sim Ngn(\Delta k_x)^4$ (since there are $N(N-1)/2$ interacting pairs), that is $E_{\text{int}}/N \sim gn(\Delta k_x)^4$. The states that we considered ($\psi_{B,\text{sq}}$, $\psi_{B,\text{cf}}^{\text{sq}}$, and ψ_J) have $\Delta k_x \sim n^{1/3}$ which leads to $E_{\text{int}}/N \sim gn^{7/3}$.

The method described here works only if derivatives of ψ_B are defined at points where $\mathbf{r}_i = \mathbf{r}_j$. This is, for example, not the case with $\psi_{B,\text{abs}}$ or $\psi_{B,\text{cf}}$. However, in those cases it is still possible to estimate the interaction energy: we again concentrate on a two-body wave-function, that is, we fix $\boldsymbol{\lambda} = (\mathbf{r}_3, \dots, \mathbf{r}_N)$ and we look what happens with $\psi_{\downarrow \dots \downarrow}(\mathbf{r}_1, \mathbf{r}_2; \boldsymbol{\lambda})$. Then we can estimate the value of $\psi(\mathbf{r}_1 = \mathbf{r}_2)$ by looking into its Fourier transform.

The general conclusion is that $E_{\text{int}}/N \sim gn(\Delta k_x)^{2m}$, where $m = 1$ if the first derivative of ψ with respect to relative distance $\mathbf{r}_{ij} = \mathbf{r}_i - \mathbf{r}_j$ does not approach zero as $\mathbf{r}_{ij} \rightarrow 0$, $m = 2$ if the first derivative approaches zero, but the second derivative does not as $\mathbf{r}_{ij} \rightarrow 0$, etc. For example, wave-functions $\psi_{B,\text{abs}}$ or $\psi_{B,\text{cf}}$ therefore have $E_{\text{int}}/N \sim gn(\Delta k_x)^2$.

Bibliography

- [1] X.-L. Qi and S.-C. Zhang, Rev. Mod. Phys. **83**, 1057 (2011).
- [2] I. Žutić, J. Fabian and S. Das Sarma, Rev. Mod. Phys. **76**, 323 (2004).
- [3] R.M. Lutchyn, J.D. Sau and S. Das Sarma, Phys. Rev. Lett. **105**, 077001 (2010).
- [4] V. Mourik, K.Zuo, S.M. Frolov, S.R. Plissard, E.P.A.M. Bakkers and L.P. Kouwenhoven, Science **336**, 1003 (2012).
- [5] J. Dalibard, F. Gerbier, G. Juzeliūnas and P. Öhberg, Rev. Mod. Phys. **83**, 1523 (2011).
- [6] V. Galitski and I. B. Spielman, Nature **494**, 49 (2013).
- [7] Y.-J. Lin, K. Jimenez-Garcia and I.B. Spielman, Nature **471**, 83 (2011).
- [8] C.V. Parker, L.-C. Ha and C. Chin, Nat. Phys. **9**, 769 (2013).
- [9] L.L. Foldy and S.A. Wouthuysen, Phys. Rev. **78**, 29 (1950).
- [10] R. Winkler, *Spin-Orbit Coupling Effects in Two-Dimensional Electron and Hole Systems* (Springer, Berlin, 2003).
- [11] G. Dresselhaus, Phys. Rev. **100**, 580 (1955).
- [12] E.I. Rashba, Sov. Phys. Solid State **2**, 1109 (1960).
- [13] I. Bloch, J. Dalibard and W. Zwerger, Rev. Mod. Phys. **80**, 885 (2008).

- [14] Y.-J. Lin, R.L. Compton, K. Jimenez-Garcia, J.V. Porto and I.B. Spielman, *Nature* **462**, 628 (2009).
- [15] H. Miyake, G.A. Siviloglou, C.J. Kennedy, W.C. Burton and W. Ketterle, *Phys. Rev. Lett.* **111**, 185302 (2013).
- [16] M. Aidelsburger, M. Atala, M. Lohse, J.T. Barreiro, B. Paredes and I. Bloch, *Phys. Rev. Lett.* **111**, 185301 (2013).
- [17] J. Ruseckas, G. Jūzeliunas, P. Öhberg and M. Fleischhauer, *Phys. Rev. Lett.* **95**, 010404 (2005).
- [18] T.D. Stanescu, C. Zhang and V. Galitski, *Phys. Rev. Lett.* **99**, 110403 (2007).
- [19] T.D. Stanescu, B. Anderson and V. Galitski, *Phys. Rev. A* **78**, 023616 (2008).
- [20] Y. Li, P. Pitaevskii and S. Stringari, *Phys. Rev. Lett.* **108**, 225301 (2012).
- [21] P. Wang, Z.-Q. Yu, Z. Fu, J. Miao, L. Huang, S. Chai, H. Zhai and J. Zhang, *Phys. Rev. Lett.* **109**, 095301 (2012).
- [22] L.W. Cheuk, A.T. Sommer, Z. Hadzibabic, T. Yefsah, W.S. Bakr and M.W. Zwierlein, *Phys. Rev. Lett.* **109**, 095302 (2012).
- [23] S.-C. Ji, J.-Y. Zhang, L. Zhang, Z.-D. Du, W. Zheng, Y.-J. Deng, H. Zhai, S. Chen and J.-W. Pan, *Nat. Phys.* **10**, 314 (2014).
- [24] S. Sinha, R. Nath and L. Santos, *Phys. Rev. Lett.* **107**, 270401 (2011).
- [25] R. Barnett, S. Powell, T. Grass, M. Lewenstein and S. Das Sarma, *Phys. Rev. A* **85**, 023615 (2012).
- [26] T.A. Sedrakyan, A. Kamenev and L.I. Glazman, *Phys. Rev. A* **86**, 063639 (2012).
- [27] I.B. Spielman, private communication.
- [28] D.L. Campbell, G. Jūzeliunas and I.B. Spielman, *Phys. Rev. A* **84**, 025602 (2011).
- [29] B.M. Anderson, G. Jūzeliunas and I.B. Spielman, *Phys. Rev. Lett.* **111**, 125301 (2013).

- [30] Z.-F. Xu, L. You and M. Ueda, Phys. Rev. A **87**, 063634 (2013).
- [31] C. Wang, C. Gao, C.-M. Jian and H. Zhai, Phys. Rev. Lett. **105**, 160403 (2010).
- [32] T.-L. Ho and S. Zhang, Phys. Rev. Lett. **107**, 150403 (2011).
- [33] C. Wu, I. Mondragon Shem and X.-F. Zhou, Chin. Phys. Lett. **28**, 097102 (2011).
- [34] S.-K. Yip, Phys. Rev. A **83**, 043616 (2011).
- [35] A.J. Leggett, Rev. Mod. Phys. **73**, 307 (2001).
- [36] A.J. Leggett, *Bose-Einstein Condensation: from Atomic Physics to Quantum Fluids*, Proceedings of the 13th Physics Summer School, edited by C.M. Savage and M. Das (World Scientific, Singapore) (2000).
- [37] Y. Castin and R. Dum, Eur. Phys. J. D **7**, 399-412 (1999).
- [38] M. Burrello and A. Trombettoni, Phys. Rev. Lett. **105**, 125304 (2010).
- [39] F. Dalfovo and S. Stringari, Phys. Rev. A **53**, 2477 (1996).
- [40] K. Kasamatsu, M. Tsubota and M. Ueda, Phys. Rev. Lett. **91**, 150406 (2003).
- [41] I.B. Spielman, Phys. Rev. A **79**, 063613 (2009).
- [42] The equation can be derived using expressions given in C.J. Pethick and H. Smith, 2008, *Bose-Einstein Condensation in Dilute Gases* (Cambridge University Press, Cambridge, England).
- [43] X.-Q. Xu and J.H. Han, Phys. Rev. Lett. **107**, 200401 (2011).
- [44] X.-F. Zhou, J. Zhou and C. Wu, Phys. Rev. A **84**, 063624 (2011).
- [45] M. Lewenstein, A. Sanpera, V. Ahufinger, B. Damski, A. Sen De and U. Sen, Adv. Phys. **56**, 243 (2007).
- [46] M. Greiner, O. Mandel, T. Esslinger, T. Hänsch and I. Bloch, Nature **415**, 39 (2002).
- [47] D. Jaksch, C. Bruder, J.I. Cirac, C.W. Gardiner and P. Zoller, Phys. Rev. Lett. **81**, 3108 (1998).

- [48] A.B. Kuklov and B.V. Svistunov, Phys. Rev. Lett. **90**, 100401 (2003).
- [49] L.-M. Duan, E. Demler and M.D. Lukin, Phys. Rev. Lett. **91**, 090402 (2003).
- [50] A.Y. Kitaev, Ann. Phys. **321**, 2 (2006).
- [51] A. Micheli, G.K. Brennen and P. Zoller, Nat. Phys. **2**, 341 (2006).
- [52] J. Simon, W.S. Bakr, R. Ma, M.E. Tai, P.M. Preiss and M. Greiner, Nature **472**, 307 (2011).
- [53] N. Goldman, A. Kubasiak, A. Bermudez, P. Gaspard, M. Lewenstein and M.A. Martin-Delgado, Phys. Rev. Lett. **103**, 035301 (2009).
- [54] T. Graß, K. Saha, K. Sengupta and M. Lewenstein, Phys. Rev. A **84**, 053632 (2011).
- [55] N. Goldman, W. Buegeling and C. Morais Smith, Europhys. Lett. **97**, 23003 (2012).
- [56] J. Larson, J.-P. Martikainen, A. Collin and E. Sjöqvist, Phys. Rev. A **82**, 043620 (2010).
- [57] L. Stekhtman, O. Entin-Wohlman and A. Aharony, Phys. Rev. Lett. **69**, 836 (1992).
- [58] L. Stekhtman, A. Aharony and O. Entin-Wohlman, Phys. Rev. B **47**, 174 (1993).
- [59] A. Zheludev, S. Maslov, G. Shirane, I. Tsukada, T. Masuda, K. Uchinokura, I. Zaliznyak, R. Erwin and L.P. Regnault, Phys. Rev. B **59**, 11432 (1999).
- [60] G. Jackeli and G. Khaliullin, Phys. Rev. Lett. **102**, 017205 (2009).
- [61] N. Marzari and D. Vanderbilt, Phys. Rev. B **56**, 12847 (1997).
- [62] A.H. MacDonald, S.M. Girvin and D. Yoshioka, Phys. Rev. B **37**, 9753 (1988).
- [63] Z. Nussinov, M. Biskup, L. Chayes and J. van den Brink, Rev. Mod. Phys. **87**, 1 (2015).
- [64] E. Altman, E. Demler and M.D. Lukin, Phys. Rev. A **70**, 013603 (2004).

- [65] T.A. Corcovilos, S.K. Baur, J.M. Hitchcock, E.J. Mueller and R.G. Hulet, *Phys. Rev. A* **81**, 013415 (2010).
- [66] K. Inaba and M. Yamashita, *Phys. Rev. Lett.* **105**, 173002 (2010).
- [67] R. Jördens, L. Tarruell, D. Greif, T. Uehlinger, N. Strohmaier, H. Moritz, T. Esslinger, L. De Leo, C. Kollath, A. Georges, V. Scarola, L. Pollet, E. Burovski, E. Kozik and M. Troyer, *Phys. Rev. Lett.* **104**, 180401 (2010).
- [68] D.C. McKay and B. DeMarco, *Rep. Prog. Phys.* **74**, 054401 (2011).
- [69] R.A. Hart, P.M. Duarte, T.-L. Yang, X. Liu, T. Paiva, E. Khatami, R.T. Scalettar, N. Trivedi, D.A. Huse and R.G. Hulet, *Nature* **519**, 211 (2015).
- [70] W.S. Cole, S. Zhang, A. Paramekanti and N. Trivedi, *Phys. Rev. Lett.* **109**, 085302 (2012).
- [71] Z. Cai, X. Zhou and C. Wu, *Phys. Rev. A* **85**, 061605(R) (2012); M. Gong, Y. Qian, V.W. Scarola and C. Zhang, *Sci. Rep.* **5**, 10050 (2015).
- [72] S. Mandal, K. Saha and K. Sengupta, *Phys. Rev. B* **86**, 155101 (2012).
- [73] A. Polkovnikov, K. Sengupta, A. Silva and M. Vengalattore, *Rev. Mod. Phys.* **83**, 863 (2011).
- [74] W.S. Bakr, A. Peng, M.E. Tai, R. Ma, J. Simon, J.I. Gillen, S. Folling, L. Pollet and M. Greiner, *Science* **329**, 547 (2010).
- [75] J. Stenger, S. Inouye, A.P. Chikkatur, D.M. Stamper-Kurn, D.E. Pritchard and W. Ketterle, *Phys. Rev. Lett.* **82**, 4569 (1999).
- [76] M. Cheneau, P. Barmettler, D. Poletti, M. Endres, P. Schauss, T. Fukuhara, C. Gross, I. Bloch, C. Kollath and S. Kuhr, *Nature* **481**, 484 (2012).
- [77] U. Schneider, L. Hackermüller, J.P. Ronzheimer, S. Will, S. Braun, T. Best, I. Bloch, E. Demler, S. Mandt, D. Rasch and A. Rosch, *Nat. Phys.* **8**, 213 (2012).
- [78] C.-L. Hung, V. Gurarie and C. Chin, *Science* **341**, 1213 (2013).
- [79] L. Kadanoff and G. Baym, *Quantum Statistical Mechanics* (W. A. Benjamin Inc, New York, 1962).

- [80] M.I. Dyakonov, V.I. Perel, Zh. Eksp. Teor. Fiz. **60**, 1954 (1971) [Sov. Phys. JETP **33**, 1053 (1971)].
- [81] R.J. Elliott, Phys. Rev. **96**, 266 (1954).
- [82] Y. Yafet, Physics Letters A **98**, 287 (1983).
- [83] T.D. Stanescu and V. Galitski, Phys. Rev. B **75**, 125307 (2007).
- [84] C. Chin, R. Grimm, P. Julienne and E. Tiesinga, Rev. Mod. Phys. **82**, 1225 (2010).
- [85] X. Du, L. Luo, B. Clancy and J.E. Thomas, Phys. Rev. Lett. **101**, 150401 (2008).
- [86] J.D. Sau, R. Sensarma, S. Powell, I.B. Spielman and S. Das Sarma, Phys. Rev. B **83**, 140510(R) (2011).
- [87] S.S. Natu and S. Das Sarma, Phys. Rev. A **88**, 033613 (2013).
- [88] E.G. Mishchenko and B.I. Halperin, Phys. Rev. B **68**, 045317 (2003).
- [89] L.E. Sadler, J.M. Higbie, S.R. Leslie, M. Vengalattore and D.M. Stamper-Kurn, Phys. Rev. Lett. **98**, 110401 (2007).
- [90] T.M. Hoang, C.S. Gerving, B.J. Land, M. Anquez, C.D. Hamley and M.S. Chapman, Phys. Rev. Lett. **111**, 090403 (2013).
- [91] M. Albiez, R. Gati, J. Fölling, S. Hunsmann, M. Christiani and M.K. Oberthaler, Phys. Rev. Lett. **95**, 010402 (2005).
- [92] A. Smerzi, S. Fantoni, S. Giovanazzi and S.R. Shenoy, Phys. Rev. Lett. **79**, 4950 (1997).
- [93] A.L. Gaunt, T.F. Schmidutz, I. Gotlibovych, R.P. Smith and Z. Hadzibabic, Phys. Rev. Lett. **110**, 200406 (2013).
- [94] I.V. Tokatly and E.Y. Sherman, Phys. Rev. A. **87**, 041602(R) (2013).
- [95] T. Yu and M.W. Wu, Phys. Rev. A **88**, 043634 (2013).
- [96] D.S. Hall, M.R. Matthews, C.E. Wieman and E.A. Cornell, Phys. Rev. Lett. **81**, 1543 (1998).

- [97] C.J. Myatt, E.A. Burt, R.W. Ghrist, E.A. Cornell and C. E. Wieman, Phys. Rev. Lett. **78**, 586 (1997).
- [98] V.B. Shenoy and T.-L. Ho, Phys. Rev. Lett. **77**, 2595 (1996).
- [99] D.S. Hall, M.R. Matthews, J.R. Ensher, C.E. Wieman and E.A. Cornell, Phys. Rev. Lett. **81**, 1539 (1998).
- [100] D.M. Weld, P. Medley, H. Miyake, D. Hucul, D.E. Pritchard, W. Ketterle, Phys. Rev. Lett. **103**, 245301 (2009).
- [101] E. Altman, W. Hofstetter, E. Demler and M.D. Lukin, New J. Phys. **5**, 113 (2003).
- [102] R.A. Duine and A.H. MacDonald, Phys. Rev. Lett. **95**, 230403 (2005).
- [103] D. Pekker, M. Babadi, R. Sensarma, N. Zinner, L. Pollet, M.W. Zwierlein and E. Demler, Phys. Rev. Lett. **106**, 050402 (2011).
- [104] C. Sanner, E.J. Su, W. Huang, A. Keshet, J. Gillen and W. Ketterle, Phys. Rev. Lett. **108**, 240404 (2012).
- [105] P. Makotyn, C.E. Klauss, D.L. Goldberger, E.A. Cornell and D.S. Jin, Nat. Phys. **10**, 116 (2014).
- [106] P. Nozières and D. Saint James, J. Phys. (Paris) **43**, 1133 (1982).
- [107] S.S. Natu and E.J. Mueller, Phys. Rev. A **84**, 053625 (2011).
- [108] E.J. Mueller and G. Baym, Phys. Rev. A **62**, 053605 (2000).
- [109] S. Ashhab, J. Low Temp. Phys. **140**, 51 (2005).
- [110] K. Riedl, C. Drukier, P. Zalom and P. Kopietz, Phys. Rev. A **87**, 063626 (2013).
- [111] V.A. Kashurnikov, N.V. Prokof'ev and B.V. Svistunov, Phys. Rev. Lett. **87**, 120402 (2001).
- [112] H. Kleinert, Mod. Phys. Lett. B **17**, 1011 (2003).
- [113] R.P. Smith, R.L.D. Campbell, N. Tammuz and Z. Hadžibabić, Phys. Rev. Lett. **106**, 250403 (2011).

- [114] J.P. Eisenstein and A.H. MacDonald, *Nature* **432**, 691 (2004).
- [115] H. Bruus and K. Flensberg, *Many-Body Quantum Theory in Condensed Matter Physics* (Oxford University Press, New York, 2004).
- [116] C.J. Pethick and H. Smith, *Bose-Einstein Condensation in Dilute Gases* (Cambridge University Press, 2008).
- [117] D.S. Petrov, M. Holzmann and G.V. Shlyapnikov, *Phys. Rev. Lett.* **84**, 2551 (2000).
- [118] D.S. Petrov and G.V. Shlyapnikov, *Phys. Rev. A* **64**, 012706 (2001).
- [119] N.V. Prokof'ev, O. Ruebenacker and B.V. Svistunov, *Phys. Rev. Lett.* **87**, 270402 (2001).
- [120] L. Salasnich, P.A. Marchetti and F. Toigo, *Phys. Rev. A* **88**, 053612 (2013).
- [121] G. Bertaina and S. Giorgini, *Phys. Rev. Lett.* **106**, 110403 (2011).
- [122] J. Guzman, G.-B. Jo, A.N. Wenz, K.W. Murch, C.K. Thomas and D.M. Stamper-Kurn, *Phys. Rev. A* **84**, 063625 (2011).
- [123] I. Bloch, M. Greiner, O. Mandel, T.W. Hänsch and T. Esslinger, *Phys. Rev. A* **64**, 021402(R) (2001).
- [124] C. Hickey and A. Paramekanti, *Phys. Rev. Lett.* **113**, 265302 (2014).
- [125] L. Tarruell, D. Greif, T. Uehlinger, G. Jotzu and T. Esslinger, *Nature* **483**, 302 (2012).
- [126] G.-B. Jo, J. Guzman, C.K. Thomas, P. Hosur, A. Vishwanath, D.M. Stamper-Kurn, *Phys. Rev. Lett.* **108**, 045305 (2012).
- [127] G. Jotzu, M. Messer, R. Desbuquois, M. Lebrat, T. Uehlinger, D. Greif and T. Esslinger, *Nature* **515**, 237 (2014).
- [128] U.K. Rössler, A.N. Bogdanov and C. Pfleiderer, *Nature* **442**, 797 (2006).
- [129] F.D.M. Haldane, *Phys. Rev. Lett.* **61**, 2015 (1988).
- [130] N. Regnault and B. Andrei Bernevig, *Phys. Rev. X* **1**, 021014 (2011).

- [131] E. Berg, M.S. Rudner and S.A. Kivelson, Phys. Rev. B **85**, 035116 (2012).
- [132] X.-G. Wen, *Quantum Field Theory of Many-Body Systems* (Oxford University Press, 2004).
- [133] T.A. Sedrakyan, L.I. Glazman and A. Kamenev, Phys. Rev. B **89**, 201112(R) (2014).
- [134] H.C. Po and Q. Zhou, arXiv:1408.6421.
- [135] J. Miao, B. Liu and W. Zheng, Phys. Rev. A **91**, 033404 (2015).
- [136] R. Jastrow, Phys. Rev. **98**, 1479 (1955).
- [137] Z. Xu, L. Li, G. Xianlong and S. Chen, J. Phys.: Condens. Matter **25** 055601 (2013).
- [138] M.D. Girardeau, J. Math. Phys. **1**, 516 (1960).
- [139] S.M. Girvin and A.H. MacDonald, Phys. Rev. Lett. **58**, 1252 (1987).
- [140] M.V. Feigelman, V.B. Geshkenbein, L.B. Ioffe and A.I. Larkin, Phys. Rev. B **48**, 16641 (1993).
- [141] J. Alicea, O.I. Motrunich, M. Hermele and M.P.A. Fisher, Phys. Rev. B **72**, 064407 (2005).
- [142] M. Rossi, L. Salasnich, F. Ancilotto and F. Toigo, Phys. Rev. A **89**, 041602(R) (2014).
- [143] E.H. Lieb and W. Liniger, Phys. Rev. **130**, 1605 (1963).
- [144] P.M. Preiss, R. Ma, M.E. Tai, A. Lukin, M. Rispoli, P. Zupancic, Y. Lahini, R. Islam and M. Greiner, Science **347**, 1229 (2015).
- [145] T. Esslinger, I. Bloch and T.W. Hänsch, Journal of Modern Optics **47**, 2725 (2000).
- [146] T. Langen, R. Geiger, M. Kuhnert, B. Rauer and J. Schmiedmayer, Nat. Phys. **9**, 640 (2013).
- [147] Y.-J. Lin, R.L. Compton, A.R. Perry, W.D. Phillips, J.V. Porto and I.B. Spielman, Phys. Rev. Lett. **102**, 130401 (2009).

- [148] Z. Hadžibabić, P. Krüger, M. Cheneau, B. Battelier and J. Dalibard, *Nature* **441**, 1118 (2006).
- [149] W. Kohn, *Phys. Rev.* **115**, 809 (1959).
- [150] P.R.C. Kent, *Techniques and Application of Quantum Monte Carlo, PhD Thesis* (University of Cambridge, 1999).